

AFRL-SR-BL-TR-00-

ata sources, gathering
ct of this collection of
Davis Highway, Suite

0034

Standard Form 298 (Rev. 2-89) (EG)
Prescribed by ANSI Std. Z39.18

DTIC QUALITY INSPECTED 1

| | |
|---|----|
| 1. Introduction | 1 |
| 2. Prismatic Liquid Crystal Digital Light Deflector | 3 |
| 2.1 Digital Light Deflecting Devices – History | 3 |
| 2.2 Principles of Operation | 4 |
| 2.3 Passive Deflecting Prism | 5 |
| 2.4 Polarization Rotation Switch | 5 |
| 2.5 Complete Binary Deflecting Switch | 6 |
| 2.6 Cascaded N-Stage Device | 6 |
| 2.7 Angular Dependence of Leakage into Undesired Direction | 6 |
| 2.8 Materials | 7 |
| 2.8.1 Scattering in Low Molecular Mass Nematic Liquid Crystals | 8 |
| 2.8.2 High Birefringence, Low Molecular Mass Nematic Liquid Crystalline Materials | 8 |
| 2.8.3 Low Birefringence, Low Molecular Mass Nematic Liquid Crystalline Materials | 9 |
| 2.8.4 Crosslinked Nematic Liquid Crystalline Materials | 10 |
| 2.8.5 Scattering in Smectic A Liquid Crystalline Materials | 12 |
| 2.8.6 Smectic A Liquid Crystalline Materials | 12 |
| 2.9 Beam Steering Device – Optical Design | 15 |
| 2.9.1 Sequential Doubling of Prism Angles | 15 |
| 2.9.2 Nonlinear Sequence of Prisms | 18 |
| 2.9.3 Integrated Design of the Prism Sequence | 20 |
| 2.9.4 Design Results | 23 |
| 2.10 Beam Steering Device – Fabrication | 23 |
| 2.11 Beam Steering Device – Experimental Results | 25 |
| 2.12 Conclusions – Prismatic Liquid Crystal Beam Steering Device | 27 |
| 3. Computational Simulation of Diffractive Liquid Crystal Gratings | 29 |
| 3.1 Introduction | 29 |
| 3.2 Liquid Crystal Blazed Grating for Beam Steering | 30 |
| 3.3 Liquid Crystal Director Simulation | 31 |
| 3.4 Near Field Simulation (of Liquid Crystal Gratings) | 32 |
| 3.5 Optical Modeling of Liquid Crystals | 32 |
| 3.6 Finite-Difference Time-Domain Method | 33 |
| 3.6.1 Introduction | 33 |
| 3.6.2 How the Finite-Difference Time-Domain (FDTD) Method Works | 34 |
| 3.6.3 Optical Simulation – Anisotropic Media | 38 |
| 3.6.4 Mapping of Liquid Crystal Director onto FDTD Grid | 39 |
| 3.6.5 Optical Simulation – Light Source | 40 |
| Plane Wave | 41 |
| Note on Periodic Boundary Conditions | 44 |
| Gaussian Beam | 45 |
| 3.6.6 Grid Termination | 45 |
| 3.6.7 Numerical Stability and Accuracy | 49 |
| 3.6.8 Computational Expense | 50 |
| 3.6.9 Central Finite Differencing to Fourth Order in Space | 50 |
| 3.7 Near Field Optical Simulation – Verification | 51 |
| 3.8 Far Field Computation | 52 |
| 3.8.1 Introduction | 52 |
| 3.8.2 Diffraction Theory | 53 |
| 3.8.3 Derivation of Two-Dimensional Kirchhoff Surface Integral | 55 |
| 3.9 Initial Calculations | 57 |
| 3.10 Status of Optical Simulation Software and Grating Calculation | 61 |
| 3.11 Conclusion – Optical Simulation of Liquid Crystal Beam Steering Devices | 61 |
| 4. Cholesteric Diffraction Gratings | 63 |
| 4.1 Introduction | 63 |
| 4.2 Experimental | 64 |

| | |
|---|-----|
| 4.3 Homogeneous Modulated Textures | 65 |
| 4.3.1 Planar unidirectional cells | 65 |
| Stripes Parallel to the Rubbing Direction | 65 |
| Stripes Perpendicular to the Rubbing Direction | 69 |
| 4.3.2 Planar twist cells | 70 |
| 4.3.3 Homeotropic cells | 73 |
| 4.4 Optical and Dynamical Properties of CDG | 76 |
| 4.4.1 Electrically-Switchable CDG | 76 |
| Polymer Stabilization of Electrically-Switchable CDG | 80 |
| 4.4.2 Electrically-Controlled CDG | 82 |
| Raman-Nath Diffraction | 82 |
| Dislocation Effect on Optical Properties of CDG | 84 |
| Diffraction Gratings in Ferroelectric SmC* cells | 87 |
| Bragg Diffraction | 90 |
| 4.5 Conclusion - Cholesteric Diffraction Gratings | 91 |
| Appendix A. Mathematical Basis for Computer Simulations | 93 |
| References | 95 |
| Personnel Supported | 99 |
| Publications | 99 |
| Presentations | 100 |
| New Discoveries, Inventions, or Patent Disclosures | 101 |

1. INTRODUCTION

Beam steering technology has to this date found many commercial applications, and more await as higher performance beam steering devices are realized. Among the current uses are industrial metal cutting and laser-based displays. Among the potential future uses are freespace communications, telecommunication switches in optical fiber networks, reprographics, disc-based and volumetric data storage, and a variety of military applications.

No single beam steering technology dominates all areas of performance. Gimbaled front-surface mirrors are well established, and produce relatively uniform intensity over a fairly wide angular range. However, they are also slow, are not random access, and suffer from inertial problems when used in fast stop-start applications. Acousto-optic modulators (AOM's) are fast, and their operating principles and fabrication methods are also well known. However, they lack the wide angular range required by many applications, and can divert energy into undesired diffraction orders.

The potential for new beam steering applications and the inability of existing beam steering technologies to meet many needs have been the driving force behind the recent research into new beam steering technologies.

The ideal beam steering device would steer an incident laser beam over wide angular range with minimal loss of the beam in the device itself. Such a device would also be very fast and free of inertial drawbacks. It should direct all of its transmitted intensity in the desired direction, and uniformly so over the entire angular range. It is possible that no one technology will meet all those requirements. So there is room for the development of new beam steering technologies.

Recent research has been devoted to ceramic-based phase gratings¹, micro-electromechanical relief gratings², and micromirror devices³, among other technologies. Liquid crystalline materials are also under investigation for their potential use in beam steering devices. Liquid crystals produce useful electro-optical effects with much less applied voltage than inorganic materials. Large birefringence (up to ~ 0.3) permits fabrication of devices with a wide range of optical characteristics. Steering direction is controlled via the electro-optic properties of liquid crystals. Accordingly, these devices are free of macroscopic moving parts and performance is relatively free of inertial problems exhibited by large motor-driven mirrors.

There are two basic types of liquid crystal beam steering devices. One type separates the deflection and change-of-direction functions into separate optical elements. In this type of device, a passive birefringent deflector can steer light into two possible directions. The direction is chosen by the state of a polarization deflection switch preceding that deflecting element. Those two optical elements comprise a simple binary deflecting switch. Cascading N properly designed switches can result in a beam steering device capable of steering light into 2^N different directions.

The other type of liquid crystal beam steering device incorporates switching and steering functions in a single layer of material. This type of liquid crystal beam steering technology is found in diffractive gratings^{4,5,6,7}.

Our research was focused on the development of both types of devices. The first type is realized in a prismatic refractive device with a smectic liquid crystal wedge as a passive light deflector and twisted nematic flat cell as an optical switch. The other type is based on electrically controlled cholesteric diffraction gratings. The cholesteric

grating is a phase grating capable of both Bragg and Raman-Nath diffraction and two modes of operation: simple electric switching between non-diffractive and diffractive regimes; continuous beam steering.

The report has the following structure.

Chapter 2 is a discussion of a liquid crystal beam steering device based on the principle of separate deflecting and switching elements. The first part of Chapter 2 contains a brief survey of digital beam steering technology, followed by a layout of what needs to be done to improve this digital liquid crystal beam steering technology. Next, the basic operating principles will be reviewed. Then we will discuss design and material improvements, and finally will detail the fabrication and performance of such a device built in our laboratory.

Chapter 3 covers the development of computational techniques, which can provide analysis of the other liquid crystal beam steering technology, electrically switchable phase gratings. This section includes a short discussion on the potential use of computer designing of diffractive optical elements via an iterative Fourier Transform algorithm. The remainder of the chapter is devoted to near- and far-field simulation of liquid crystal gratings.

The development of beam steering devices based on diffraction properties of the helical structure in cholesteric LC cells is presented in the Chapter 4. The first part of Chapter 4 describes the found textures that possess in-plane periodicity and can serve as diffraction gratings. Next, the optical and dynamical properties of these textures are presented. The possibility to use the new discovered texture in ferroelectric smectic liquid crystals as a diffraction grating and the dislocation effect on optical properties of modulated structures are also discussed.

To study a fine structure of the textures numerical simulations of equilibrium structures based on the Frank-Oseen free energy density minimization has been developed. Mathematical basis of the simulations is presented in Appendix A.

2. PRISMATIC LIQUID CRYSTAL DIGITAL LIGHT DEFLECTOR

2.1 Digital Light Deflecting Devices – History

As was mentioned above, one type of beam steering technology delegates the beam deflecting and deflection change functions to two separate optical elements. This technology is inherently digital, because the deflecting element is birefringent and passive. Hence, a light beam passing through this deflector takes one of two paths, depending on its polarization state. The polarization state is determined by the other type of optical element, a polarization switch. This switch which precedes the deflector in the optical path, and usually take the form of a polarization rotator. A device based on this strategy is often called a Digital Light Deflector, or DLD.

The earliest DLD devices were based on inorganic materials. The first reports of this class of beam steering device began appearing in 1964. These devices can be grouped by the type of passive deflecting element employed. In one class of inorganic DLD's, the passive deflector was a birefringent plate, with its optic axis inclined at some design-specific angle with respect to the surface normal^{8,9,10,11}. These devices translated the incident beam, rather than inducing angular deflection. A second type of inorganic DLD utilized Wollaston prisms as the deflecting elements^{12,13,14}. A third type, closely related to the device considered in this study, made use of Calcite Prisms^{15,16,17,18}. The second and third type of inorganic DLD induced angular deflection. For most of these inorganic DLD devices, polarization switching was accomplished by means of the Pockels or Kerr cells.

These inorganic DLD devices were very fast, capable of switching between deflection positions or angles in less than a microsecond. However, they were also very bulky and consume a large amount of power. In addition, precisely fabricating the desired sequence of prism angles from inorganic birefringent materials can add substantial expense. Those are among the considerations spurring recent research into liquid crystal beam steering.

The first prismatic liquid crystal DLD (LCDLD) was reported in 1990^{19,20,21}. Like the calcite prism DLD's, its deflector is a birefringent wedge, but it is filled with liquid crystalline material. Because the device employed a nematic filler it was prone to scattering losses, which would increase as deflection angle increased. Scattering losses were discussed in those early reports and there was some speculation about potential remedies (including the use of smectic A liquid crystals), but no work was conducted in that area. Instead of Kerr or Pockels cell polarization rotators, this LCDLD employed ferroelectric liquid crystal (FLC) cells with sub-millisecond switching times. Although not as fast as Kerr or Pockels cells, this is fast enough for most applications. The device was fabricated for small angle use only, avoiding the steering errors discussed later in this report. Steering error was not even identified as a potential problem.

Based on all the above literature, the following conclusions pertaining to the current state of the art can be drawn: A compact, accurate, wide-angle, low-loss, low voltage, LCDLD has not yet been reported. Because the liquid crystal switching element (FLC) employed in the early LCDLD work left little potential for further reduction of switching time, our research was devoted to reduction of scattering losses, increasing angular range, and providing a method of designing accurate LCDLD's.

2.2. Principles of Operation

The prismatic version of the digital light deflector consists of cascaded binary light switches (Figures 2.1-2.4). Each switch consists of a passive birefringent deflecting element and a polarization rotation switch (Figure 2.5). Linearly polarized light is directed into the polarization rotation switch. Linearly polarized light transmitted by that switch emerges with its polarization plane unaltered or rotated by 90 degrees. The transmitted beam is then directed into the passive birefringent deflecting prism. The prism consists of a birefringent medium (e.g., a liquid crystal) and a means of supporting such (glass substrates). The optic axis of the birefringent medium is oriented parallel to the vertex of the prism. When light of polarization parallel to the optic axis is received by the prism, its path is deflected.

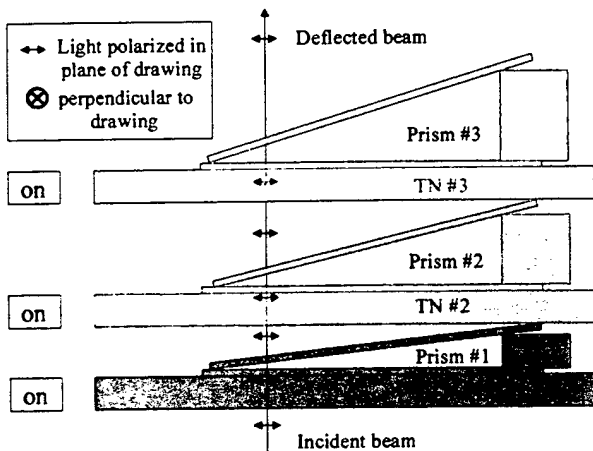


FIGURE 2.11 Three Stage LCDLD. All three polarization rotators are turned on, permitting the incident beam, polarized perpendicular to optic axes of all prisms, to pass through the entire device undeflected.

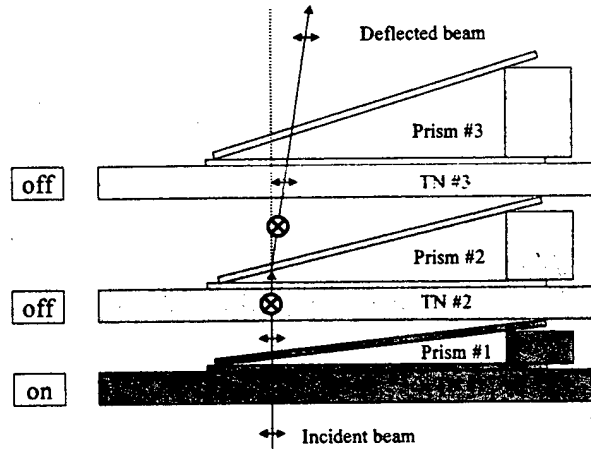


FIGURE 2.3 Three Stage LCDLD. The last two polarization rotators are turned off, permitting the incident beam to pass through the second stage parallel to its optic axis. The beam is deflected by second stage only.

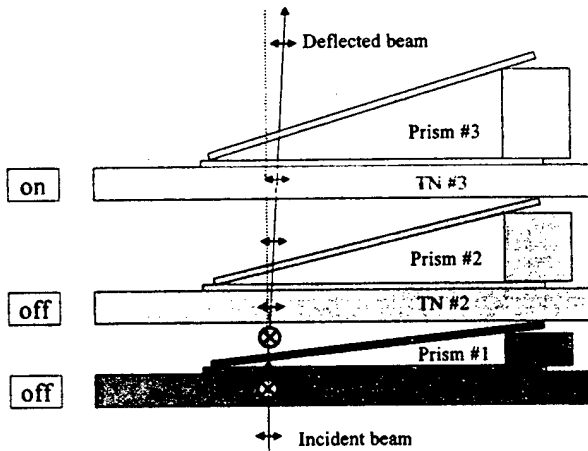


FIGURE 2.2 Three Stage LCDLD. The first two polarization rotators are turned off, permitting the incident beam to pass through the first stage parallel to its optic axis. The beam is thus deflected by first stage only.

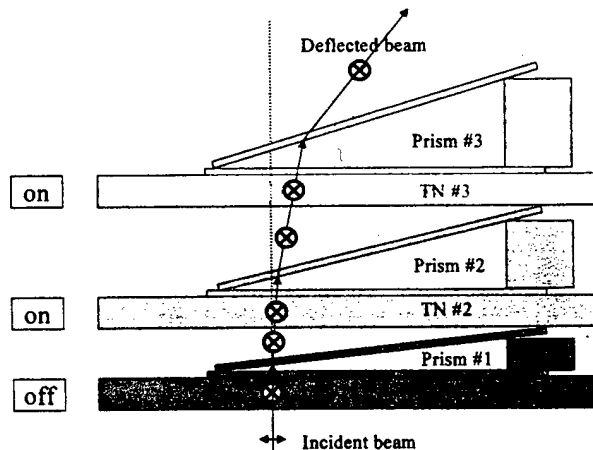


FIGURE 2.4 Three Stage LCDLD. The first polarization rotator is turned off, permitting the incident beam to pass through all stages parallel to their optic axes. The beam is deflected by all three stages.

Light of the orthogonal polarization is deflected by a lesser amount. The angular separation between these two deflections is the characteristic angular deflection of that prism.

The LCDLD is based on these simple two-position beam steering switches. Stacking together N such binary light deflecting switches can create a device capable of deflecting light by any of 2^N angles.

2.3 Passive Deflecting Prism

The passive deflectors could be fabricated from any birefringent material. Constructing a deflector from inorganic crystalline materials would be an option, except for the cost and difficulty in producing the precise sequence of prisms necessary to produce the desired deflection angles. Alternatively, the deflectors can be fabricated from liquid crystals. The deflection angle of a liquid crystal deflector can be easily customized by fabricating a prism with the appropriate angle, or appropriate choice of liquid crystal filler (with the appropriate birefringence), or a combination of both.

The passive deflecting wedge is constructed as shown in Figure 2.6. The three pieces shown are untreated glass plates (without conductive ITO coating). The interior surfaces of pieces A and B are coated with a thin layer of Dupont polyimide 2555, which should provide nearly homogeneous alignment of the liquid crystal at those surfaces. Surface A is rubbed in one direction (parallel to the wedge vertex line), and surface B in an antiparallel direction. Once filled with a liquid crystal, the optic axis of wedge cell will be parallel to the wedge vertex.

2.4. Polarization Rotation Switch

A standard twisted-nematic cell (TN), optimized for the laser wavelength to be used, is placed on the input side of the wedge (Figure 2.5). The TN's output surface liquid crystal orientation is parallel to the optic axis of the wedge.

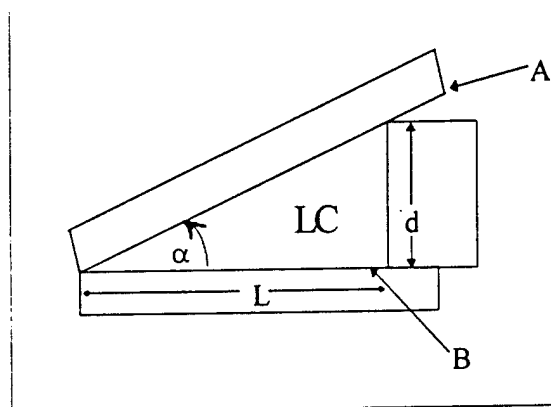


FIGURE 2.5 Binary Light Deflection Switch. Upper wedge is material with refractive index similar to glass substrates.

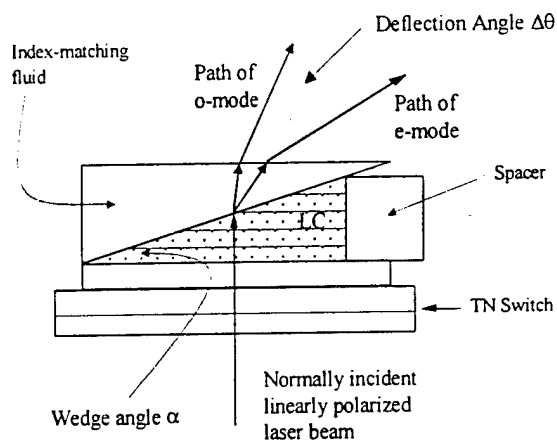


FIGURE 2.6 Passive Birefringent Deflecting Prism.

The TN optical switch may not possess the speed necessary for some applications. Times on the order of ten milliseconds are necessary for the TN cell to switch between the off and on states (i.e. to switch from one deflector output direction to the other). The use of high-birefringence nematic liquid crystals, allowing thinner TN cells, can reduce theoretical switching time only slightly below 10ms. Other nematic modes are capable of switching times as low as 1 ms. Much faster switches can be fabricated with SmC* liquid crystals. However, to demonstrate the material improvement discussed below a TN cell is sufficient.

2.5. Complete Binary Deflecting Switch

The simple switch illustrated in Figure 2.5 includes one feature not yet discussed. This added feature is an isotropic filler placed in all gaps in the device. The filler should possess a refractive index roughly equal to that of the glass being used. That gap-filling significantly reduces Fresnel reflection losses.

With no voltage applied to the TN cell, linearly polarized laser radiation will be rotated by 90 degrees. Application of a moderate voltage (approx. 5 V) to the TN reduces the optical rotation by the TN to practically zero. It is in these two states that light entering the prism will propagate through the switch entirely in one mode or the other. This assumes, of course, that light entering the TN is linearly polarized parallel or perpendicular to the prism's optic axis.

For small prism angles, the characteristic deflection angle of this binary switch is roughly equal to $\alpha\Delta n$, where Δn is the birefringence of the prism filler and α is the prism angle (Figure 2.5).

2.6. Cascaded N-Stage Device

In the composite N-stage device, the prism with the smallest characteristic deflection angle should be placed in the first stage, where the beam to be deflected first enters the device. Subsequent stages should be added in the order of their characteristic deflections. This protocol permits the smallest possible size of the composite device because it minimizes the amount of walk-off from the location of the incident beam.

2.7. Angular Dependence of Leakage into Unselected Direction

It is widely known that TN cells have optical properties which depend on the angle of incidence (in the display field, this is manifested in viewing angle problems). If a TN cell is optimized for rotation of polarization at normal incidence, it may not be so at oblique incidence.

The implication for our simple two-position switch is that, at oblique incidence, light passing from the TN cell into the deflector is no longer linearly polarized. Hence, both modes will propagate through the deflector. For small, near-normal incidence angles, the TN output polarization is only slight elliptic, so "leakage" into the non-selected deflection is not significant. At large oblique angles, the TN output is highly elliptically polarized, resulting in

visibility of both deflections simultaneously. This problem was of some concern in earlier work on inorganic calcite prism DLD's¹⁶.

This is illustrated in the following simple experiment with a single-stage LCDLD. The prism in the test device had dimensions $d=1.6\text{mm}$ and $w=20\text{mm}$ as shown in figure 2.6 (prism angle $\alpha=4.57$ degrees= 0.0798 radians). The wedge was filled with Merck 18349, a nematic liquid crystal blend with $\Delta n=0.27$, and then sealed. This prism was paired with a TN cell as shown in figure 2.5. The TN cell had been fabricated for other purposes; and exhibited 90-degree rotation for normally incident light of approximately 550nm.

A linearly polarized 633nm HeNe laser (polarized parallel to the TN's input surface orientation) was directed at the TN-wedge pair. With no voltage applied to the TN cell, the laser radiation was rotated to match the optic axis of the wedge. In that "off state", the light experienced the prism liquid crystal's extraordinary refractive index and was deflected. Then a moderate voltage (approx. 5 V) was applied to the TN, resulting in a different deflection. The two deflection paths were separated by an angle measured to be roughly equal to $\alpha\Delta n \sim 1.2$ degrees. A detector was placed at both locations. Then the LCDLD was rotated first by 10 degrees to provide a 10-degree incidence angle at the TN's entry surface. The TN cell was turned on and off, with the intensity at both detectors being measured in each state. The ratio of the intensity of the desired deflection path to the nonselected path is the Contrast Ratio. The test was repeated for an incidence angle of 33 degrees. The results appear in Table 2.1.

| Selected Mode | Incidence Angle, degrees | Contrast Ratio |
|---------------|--------------------------|----------------|
| e-mode | 10 | 200:1 |
| | 33 | 100:1 |
| o-mode | 10 | 250:1 |
| | 33 | 50:1 |

TABLE 2.1

At an incidence angle of 10 degrees, both deflections exhibit very little leakage into the nonselected deflection path. For applications not requiring an extremely wide angular range, an optimized TN cell will provide sufficient performance. Fabrication of a TN cell optimized for 633nm or use of 550nm light would improve the above results.

2.8 Materials

The deflecting wedge serves only to refract ordinary and extraordinary modes passing through it by different angles. It should do so without inducing significant losses. There are three types of losses. First are losses resulting from scattering induced by the liquid crystal director fluctuations. The second type of loss results from Fresnel reflections at refractive index mismatches. The third type of loss is leakage into an unselected steering direction, caused by imperfect polarization rotation or misalignment of a deflecting wedge with respect to its predecessor. Losses of the second and third type are important but are engineering issues and thus not of primary importance to this study.

We worked with four types of liquid crystal in an attempt to find low-loss materials for deflecting wedges: low molecular mass nematics of low and high birefringence, a crosslinkable nematic monomer, and smectic A phase materials.

2.8.1 Scattering in Low Molecular Mass Nematic Liquid Crystals. Light scattering in low molecular mass liquid crystals is caused by small-scale variations of director orientations. These fluctuations produce local inhomogeneities of the refractive index. The index variations are dynamic, induced by thermal fluctuations. Such fluctuations are quite noticeable in nematic-type liquid crystals, particularly when viewing a thin layer under a polarizing microscope at temperatures just below the nematic-isotropic transition.

Utilizing continuum theory, the scattering cross-section σ can be expressed in terms of the temporal average of those dynamic director fluctuations²²:

$$\sigma = \left(\omega^2 \Delta \epsilon / 4\pi c^2 \right)^2 \sum_{\alpha=1,2} \langle |n_{\alpha}(q)|^2 \rangle (i_{\alpha} f_z + i_z f_{\alpha})^2 \quad (2.1)$$

where $\Delta \epsilon$ is the dielectric anisotropy at a particular optical frequency and ω is the angular frequency of the illuminating light. The sum is over the two fluctuation modes (both perpendicular to the bulk director), i indicates polarization of light entering the small local region in which the director fluctuates, and f indicates the outgoing polarization. The subscript z indicates polarization along the bulk director and α indicates the two independent directions perpendicular to that director. The expectation value of the director fluctuations is:

$$\langle |n_{\alpha}(q)|^2 \rangle = (\Omega k_b T) / (K_3 q_z^2 + K_{\alpha} q_{\perp}^2 + \Delta \chi H^2) \quad (2.2)$$

where Ω is the volume of the local region, $k_b T$ is the thermal energy, $K_{1,2,3}$ are the splay, twist, and bend elastic constants of the liquid crystal, q is the magnitude of the director fluctuation in a given direction, and $\chi_{\alpha} H^2$ is the anisotropic part of the energy of an applied magnetic field. The reason for including this last term will become evident in the discussion of crosslinkable nematics below.

2.8.2 High birefringence, Low molecular mass nematic liquid crystalline materials. From Figure 2.5 we can derive that, for small prism angles, the e- and o-mode beam separation is approximately $\alpha \Delta n$. So in general, a high birefringence is desirable in order to make an effective passive deflecting element for wider steering angles. The trade-off, seen in Eqn. (2.1) above, is that scattering in a liquid crystal is proportional to the square of the birefringence. So it should not be surprising that nematic liquid crystals with a large birefringence, required for wide-angle steering, exhibits significant scattering losses.

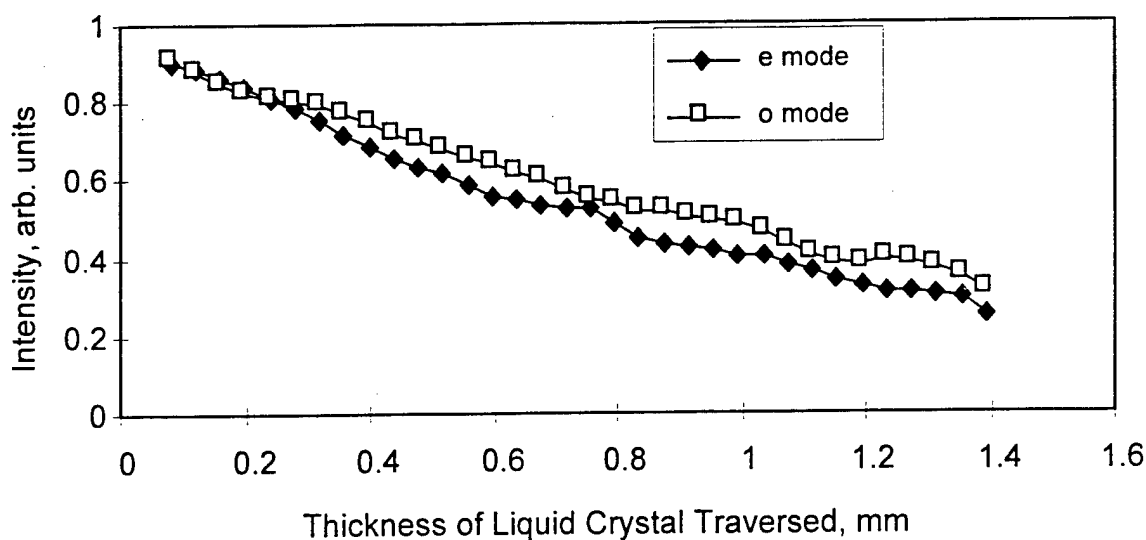


FIGURE 2.7. Intensity of 632.6nm HeNe laser transmitted through nematic liquid crystal Merck 18349.

Figure 2.7 shows the amount of light transmitted through a high birefringence nematic liquid crystal (Merck 18349, $\Delta n=0.27$) as a function of the thickness of material traversed. Transmitted intensity for this material depends strongly on layer thickness. Both e- and o-modes are affected, the e-mode more seriously as expected by theory. By the time a beam has passed through 1.4mm of this substance, 70% of the incident intensity is lost to scattering. Using the small angle approximation $\Delta\theta=\alpha\Delta n$, and assuming a prism "length" $L=20\text{mm}$ (see Figure 2.6), a prism with thickness $d=1.4\text{mm}$ would separate the e- and o-modes by only one degree. A wide-angle LCDLD based on this material would be prone to significant scattering losses.

2.8.3 Low birefringence, Low molecular mass nematic liquid crystalline materials. Even without computing the exact scattering cross-section from Eqns. (2.1) and (2.2), it is obvious that scattering losses are proportional to the square of the optical anisotropy. Additionally, in the one constant approximation $K_1=K_2=K_3=K$, scattering losses are inversely proportional to the magnitude of the elastic constant of the liquid crystal. In general, liquid crystals with small optical anisotropy (i.e. small birefringence Δn) possess smaller elastic constants than high birefringence liquid crystals. The tradeoff suggests favorably low scattering losses for materials with low birefringence.

A prism with $L=20\text{mm}$ and $d=1.6\text{mm}$ was filled with Merck liquid crystal ZLI-2806 ($\Delta n=0.043$). A Helium-Neon laser beam was directed toward the prism at normal incidence to one of the prism faces. The intensity of the transmitted beam was measured at the point where the prism was 1.4mm thick. The wedge transmitted 6% less intensity at this point than near the vertex, compared to 70% loss for the high-birefringence nematic.

This low-birefringence prism produced a characteristic beam separation of 0.19° . A prism filled with Merck liquid crystal with the same characteristic angular separation would, for $L=20\text{mm}$, possess $d\sim 0.25\text{mm}$. Light passing through the thick end of such a prism would experience scattering losses of $\sim 20\%$. So it would appear that use of a

low-birefringence material provides significant reduction of scattering losses, when compared to high-birefringence nematic prisms with the same beam separation.

Nevertheless, the low-birefringence nematic still exhibits measurable loss. But of greater concern is that the above low-birefringence prism produced a separation of only 0.19° between the e- and o-modes. Larger beam deflections will require passive deflecting prisms with steeper angles. A low-birefringence nematic-filled prism with characteristic beam separation of 1° would, for $L=20\text{mm}$, require $d=8\text{mm}$ (prism angle $\alpha \sim 21.8^\circ$). Using the simple prismatic LCDLD architecture, maximum angular range will be severely limited because of the low birefringence.

2.8.4 Crosslinked nematic liquid crystalline materials. Neither low- nor high-birefringence low molecular mass nematic liquid crystals provide a suitable medium for constructing wide-angle low-loss prismatic LCDLD's. The high-birefringence nematic would be the best choice if not for its inherent scattering losses. If a nematic liquid crystal is to be used, a way must be found to reduce light scattering. That is, the thermally-induced director fluctuations causing light scattering must be suppressed.

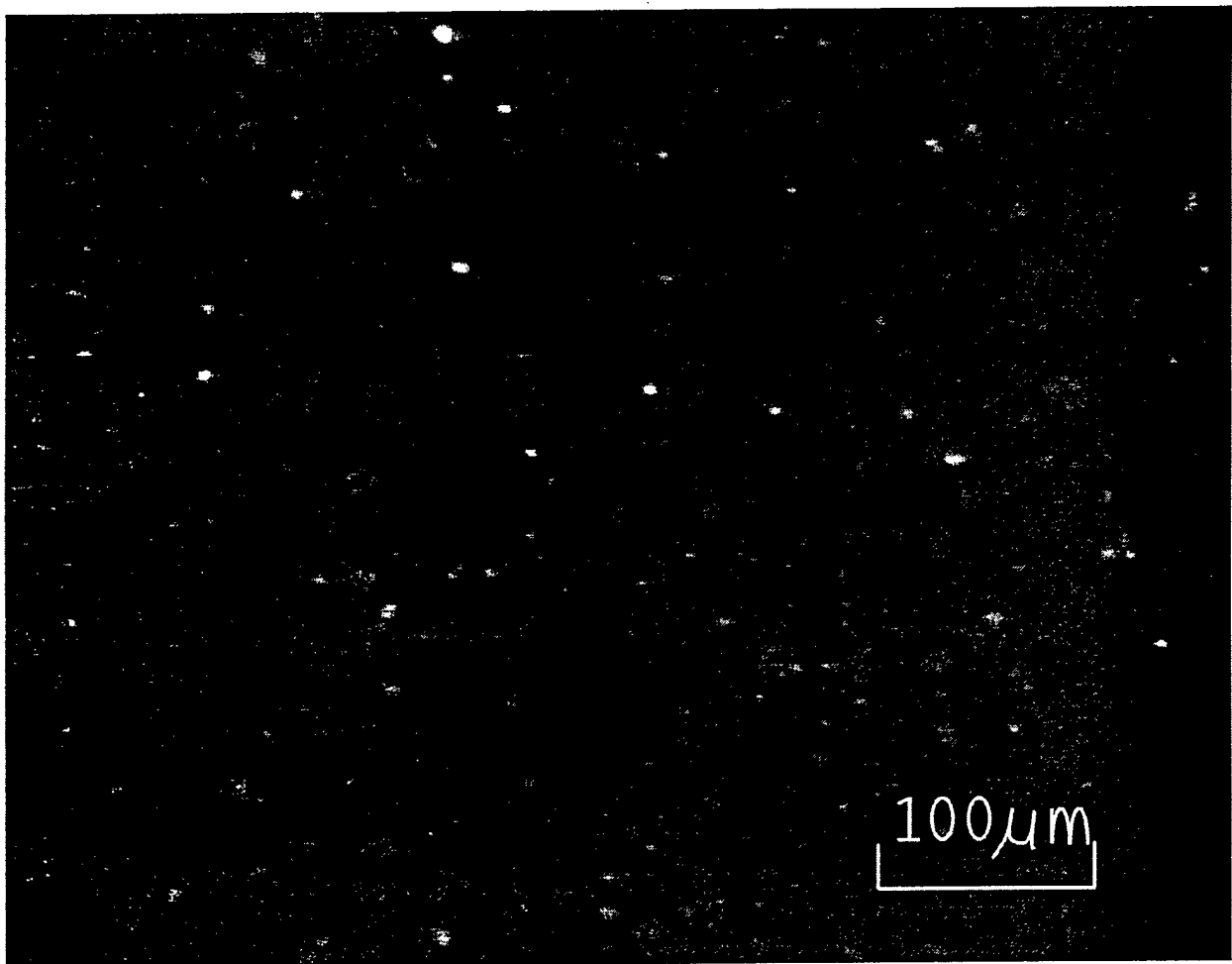


FIGURE 2.8 Photograph of $100\mu\text{m}$ thick layer of crosslinked nematic monomer, homogeneous alignment, placed between crossed polarizers.

One means of restricting the dynamic fluctuations is to frustrate one or more degrees of freedom of those fluctuations. A plausible means of accomplishing that task is to incorporate the nematic unit in a monomer, impose the desired bulk orientation, and polymerize or crosslink to lock in that orientation. The resulting three-dimensionally interconnected network should serve to restrict the motion of individual nematic mesogens.

Our work in this area centered on a liquid crystalline diacrylate monomer, which has been reported to form crosslinked layers with macroscopic orientation²³. The reported work was conducted on thin (5 μ m) layers. Surface rubbing was sufficient to produce macroscopic planar orientation of the liquid crystal monomer, parallel to the rub direction. We attempted to reproduce those results for a wedge cell with maximum thickness of 1.6mm.

Before we could accomplish the $d=1.6$ mm wedge, another problem was uncovered. Observation of a crosslinked layer with a uniform thickness of 100 μ m, the bulk orientation was observed (parallel to the rub direction).

However, the crosslinked nematic layer would not, in any orientation between parallel polarizers under a microscope, produce a "completely" dark state. Instead, the texture looked somewhat mottled, similar to that observed when viewing uncrosslinked nematic layers. Closer inspection did not indicate any *dynamic* fluctuations, but the texture was still speckled (Figure 2.8). We believe that the crosslinking process did effectively eliminate dynamic scattering, leaving behind a *static* scattering problem. This could be caused by the nematic existing in a dynamically fluctuating state prior to and during the crosslinking process. The crosslinking effectively fixes in place the spatial director variations existing at the time of crosslinking. In effect, the crosslinked layers provided a snapshot of dynamic fluctuations (figure 2.9). In order for this material to be of use, dynamic director fluctuations must be temporarily quenched prior to and during crosslinking.

Theoretical dependence of director fluctuation magnitude on applied external field has long been known²². Several investigators have explored this dependence^{24,25}.

We applied a 1T field (the limit of our laboratory electromagnet) to a 100 μ m thick layer of common nematic material with optical properties similar to the crosslinkable nematic monomer. Unfortunately, there was no observable reduction in turbidity, and the intensity of a transmitted laser beam was not measurably altered.

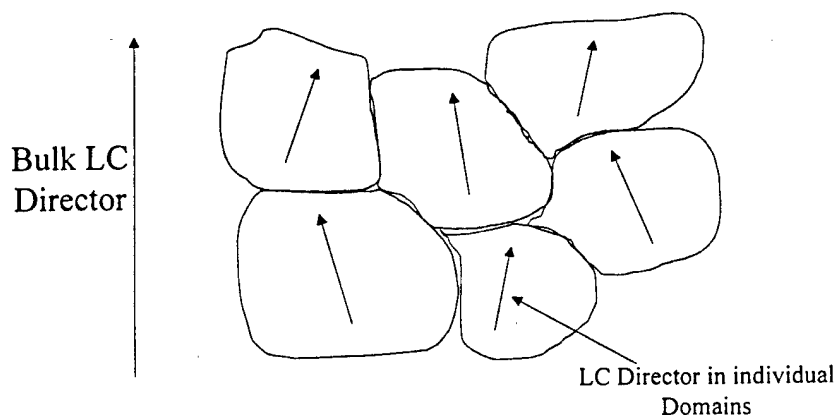


FIGURE. 2.9 Drawing of director fluctuations "frozen" by crosslinking of a nematic monomer.

In order to see why no significant improvement was obtained, it is sufficient to examine the denominator from Eqn. (2.2) for the magnitude of director fluctuations:

$$\langle |n_\alpha(q)|^2 \rangle \propto 1/(K_3 q_z^2 + K_\alpha q_\perp^2 + \Delta\chi H^2) \quad (2.3)$$

In the one-constant approximation, this becomes, for the purpose of dimensional analysis:

$$\langle |n_\alpha(q)|^2 \rangle \propto 1/(K q^2 + \Delta\chi H^2) \quad (2.4)$$

In order to suppress director fluctuations and have a significant impact on light scattering, the energy density of the applied magnetic field must be comparable to the distortion energy of the director fluctuation. K is on the order of 10^{-11} N and the dimensionless bulk value of $\Delta\chi \sim 10^{-6}$ in the SI system of units. If we assume, for wide-angle scattering, $q \sim 2\pi/\lambda$ where $\lambda \sim 500$ nm, then the two energies are comparable when $H \sim 4$ T, much higher than can be obtained with our wire-wound laboratory electromagnets. Moreover, to suppress the fluctuations to the point where scattering becomes insignificant, the applied field should be much higher still.

2.8.5 Scattering in Smectic A Liquid Crystalline Materials. Scattering is caused by fluctuations in the orientations of liquid crystal molecules. Such fluctuations are quite noticeable in nematic-type liquid crystals, which possess only orientational order. Additional order, such as the one-dimensional positional order produced by smectic A phase liquid crystal layer structures, restrains some fluctuation modes and reduces scattering. In essence, the twist and bend deformations common to nematics are suppressed in a smectic liquid crystal, and a new deformation, that of layer compression, is introduced. Light scattering is, as with nematic liquid crystals, dependent on director fluctuations. For a smectic A liquid crystal, the mean square fluctuation of the director takes the form²⁶:

$$\langle |n_\alpha(q)|^2 \rangle \propto 1/(B q_z^2 q_\perp^{-2} + K_1 q_\perp^2 + \Delta\chi H^2) \quad (2.5)$$

where B is the elastic modulus of smectic layer compressibility. The second term in the denominator is familiar from the similar expression for nematics; it represents splay energy of director fluctuations. In general, the elastic constant for layer compressibility is quite high, and for most scattering geometries the first term in the denominator is much larger than the second. As a result, smectic A liquid crystals do not scatter light as well as nematics, for most scattering geometries.

The reduced light scattering in smectic A liquid crystals can be quite useful in passive (i.e. non-switched) birefringent optical components.

2.8.6 Smectic A Liquid Crystalline Materials. Fabrication of smectic liquid crystal deflectors posed a unique challenge. The fabrication process is as follows. Optical elements, constructed from mechanically rubbed

polyimide-coated surfaces, are filled with the smectic A liquid crystal material. The desired orientation of molecules is obtained by heating liquid crystal into its nematic phase. The element is then cooled to its smectic A phase. It is during the cooling process that defects (which scatter light) are likely to occur. Most of the available room-temperature smectic A liquid crystals (e.g. 8CB, shown in figure 2.10) are polar molecules. These materials produce a partially interdigitated bilayer structure, the smectic- A_d phase. The degree of interdigitation, and thus the layer thickness, varies with temperature, as shown in figure 2.10. Because the layers are not very compressible²⁶, layer shrinkage results in a tilting of the layers so as to occupy the same fixed volume. This tilting of layers may promote the formation of focal-conic defects in the smectic- A_d phase^{27,28}, shown in the photo in figure 2.13.

The search for a useful smectic A material centered on those materials which possess a room temperature monolayer smectic- A_1 or non-interdigitated bilayer smectic- A_2 phase. One such material is a blend of the $n=6,7$ homologues of dialkylazoxybenzene (DnAOB), shown in figure 2.11. These molecules possess only a small lateral dipole moment and should produce a monolayer structure.

A weight-ratio blend of 46% D6AOB to 54% D7AOB exhibits an ordinary refractive index of 1.52 and an extraordinary refractive index of 1.72. This blend possesses a smectic A phase at room temperature. Prisms filled with this blend do appear to form significantly fewer defects. This blend does have a small drawback. Because of the azoxy bridge group, it absorbs the shorter visible wavelengths. This blend can be used as long as the absorption does not present a problem. Comparison of the transmissive properties of this blend with that of the nematic discussed earlier is shown in the figure 2.12.

The use of the above-mentioned material eliminates scattering losses as an optical design problem. The only remaining important design consideration is steering accuracy.

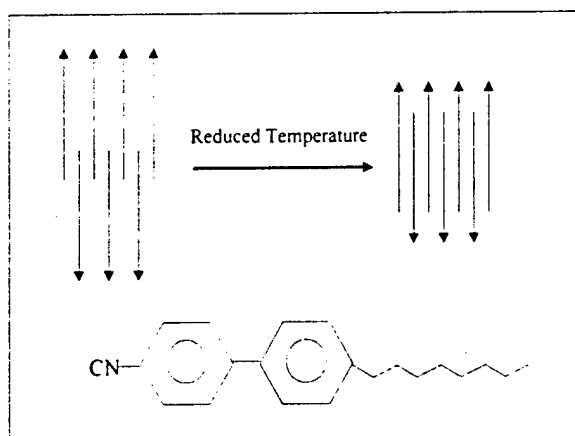


FIGURE 2.10 Interdigitated smectic A_d layer structure of 8CB. Layer thickness decreases with decreasing temperature

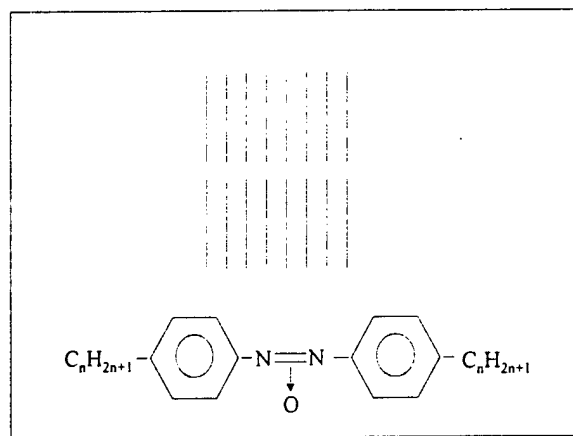


FIGURE 2.11 Monolayer smectic A structure exhibited by blend of D6AOB and D7AOB. Layer thickness does not vary with temperature.

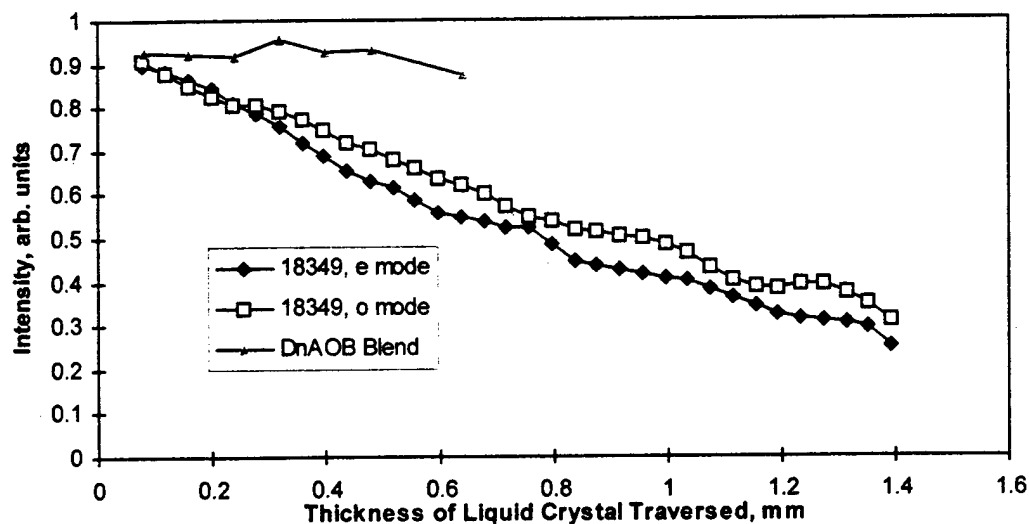


FIGURE 2.12 Non-scattered Transmissivity vs. Liquid Crystal Layer Thickness. Comparison of a nematic material (18349) to a nonpolar smectic A blend (DnAOB).

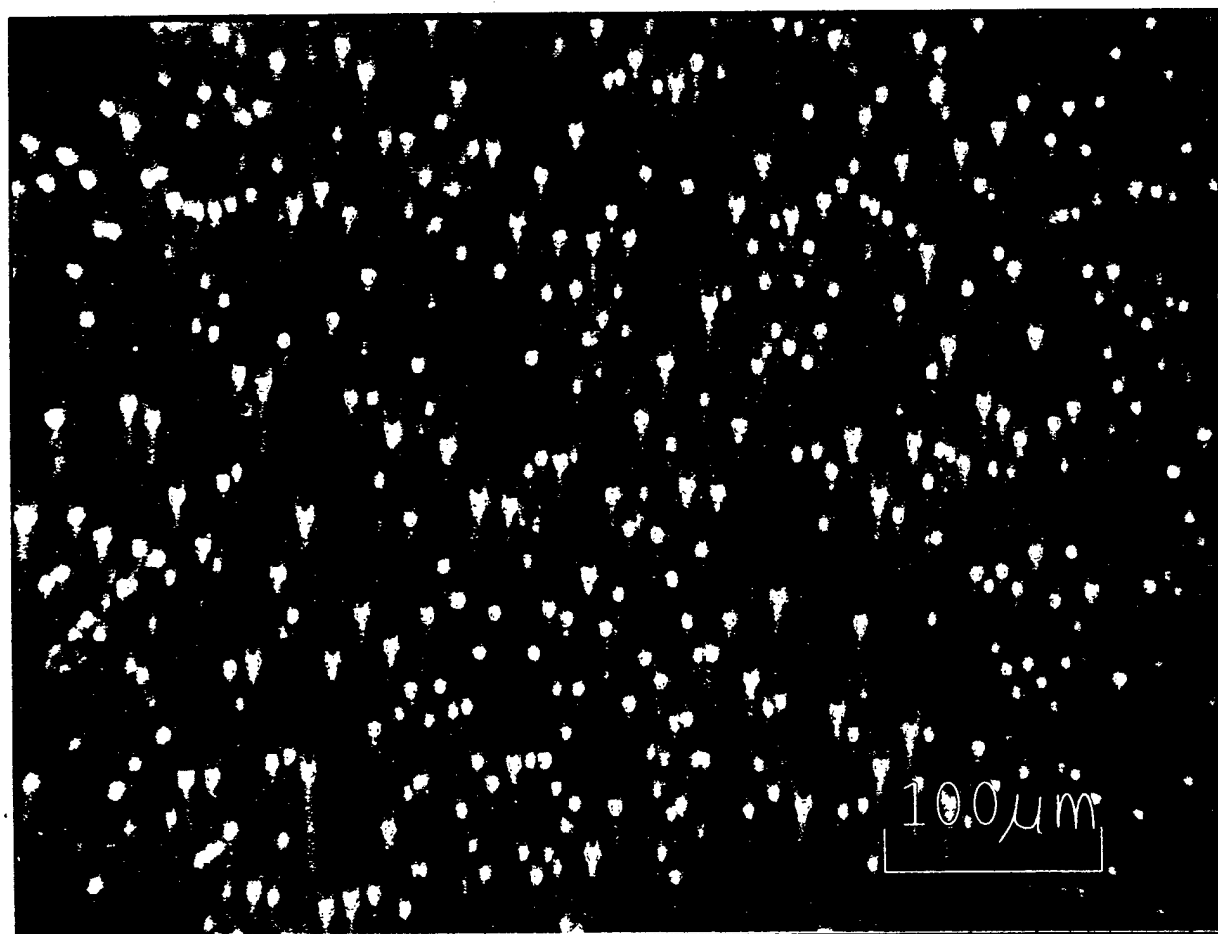


FIGURE 2.13 Photograph of 100μm thick layer of 8CB, homogeneous alignment, placed between crossed polarizers on a microscope stage.

2.9. Beam Steering Device – Optical Design

The stacked prismatic architecture is not free of limitations. One of those limitations is that, as more and more stages with increasingly large characteristic deflections are stacked together, it becomes more difficult to obtain a constant angular separation of adjacent steering positions throughout the device's entire angular range. This problem becomes more pronounced at the outer reaches of the angular range.

For prismatic LCDLD devices with small angular range, 2 degrees or less, this problem is not significant.

One measure of DLD device accuracy is the external angular separation of adjacent deflection paths. Ideally, all such angular separations should be the same, equal to the desired resolution of the device. All of the following design calculations arbitrarily assume an angular separation equal to the far-field divergence angle of a common laboratory helium-neon laser operating at 632.8nm. The device should be placed somewhere in the near field (i.e. within the Rayleigh range) of the laser. Steering accuracy and resolution specifications will be met in the far field.

A device with constant angular separation over its entire range would be easy to design if all the liquid crystals to be used as prism fillers possessed ordinary and extraordinary refractive indices symmetric about that of the substrate and the index-matched filler. However, it is difficult to find such suitable liquid crystals, particularly those with high birefringence and a monolayer room temperature smectic A phase. Hence, accuracy may be a problem unless the cascaded device is designed and fabricated for non-ideal refractive indices.

The key to an accurate LC-DLD lies in the design and placement of the deflecting wedges. As has already been mentioned and will be shown below, accurate devices with a small angular range (a few degrees) are easy to design. One can choose the angle of the first wedge to produce the desired angular resolution. Deflecting prisms in each subsequent stage, making use of the same birefringent filler, are fabricated with twice the wedge angle of the previous stage. The prisms and stages are then assembled exactly as shown in figure 2.2. This simplistic approach can be called a Doubled Sequence of prisms.

It is not until a wide-angle device is desired that the inherent flaw of that approach becomes apparent. As the external steering angle increases, so do internal beam path incidence angles at refractive index mismatches. As these angles increase, the linear small-angle approximation to Snell's law is no longer valid. So the task is to find a means of incorporating this "problem" into the design.

Below, we describe three approaches to design: treating each prism in the sequence as an independent deflector (both small and large angle calculations), and treating all prisms in the composite device as part of one integrated structure. These approaches produce Doubled, Nonlinear, and Integrated sequences of prisms, respectively. The first of these is the faulty Doubled Sequence approach described above, and is included primarily as a reference for the other two approaches.

2.9.1. Sequential Doubling of Prism Angles. This design approach is based on the approximation that, for a given birefringent medium, doubling the prism angle will double the angular separation between the two propagation paths of a linearly polarized beam. This works up to a point, as shown below.

In order to derive the relations necessary to calculate prism angles, we employ simple raytracing analysis. The two possible beam paths, upon exiting into the air from the single stage in figure 2.5, are derived from Snell's Law:

$$\theta_{exit,e-mode} = \sin^{-1} \left\{ n_G \cdot \sin \left[\sin^{-1} \left(\frac{n_e}{n_G} \sin(\alpha) \right) - \alpha \right] \right\} \quad (2.6)$$

$$\theta_{exit,o-mode} = \sin^{-1} \left\{ n_G \cdot \sin \left[\sin^{-1} \left(\frac{n_o}{n_G} \sin(\alpha) \right) - \alpha \right] \right\} \quad (2.7)$$

Here, n_G is the refractive index of the glass and isotropic filler, n_e and n_o are the extraordinary and ordinary refractive indices of the liquid crystal inside the prism, and α is the prism's internal angle. For small prism angles, the angular separation between these two paths becomes:

$$\Delta\theta_{exit,j} = \theta_{exit,e-mode} - \theta_{exit,o-mode} \approx \alpha_j \cdot \Delta n_j \quad (2.8)$$

where Δn is the liquid crystal's birefringence and the subscript j denotes the j^{th} stage in the N-stage device.

The design begins with a choice of device resolution. If we wish to distinctly resolve, without overlap, the $1/e^2$ diameter of a common laboratory Helium Neon laser possessing a far field divergence angle of 0.001007 radians, then the first stage in the device should produce an angular separation of e- and o-modes equal to that amount. This will be denoted $\Delta\theta_{exit,1}$. The second stage should produce an angular separation of twice that, and so forth. Then, using Eqn. (2.8), the sequence of prisms can be determined from the following prescription:

$$\alpha_1 = \Delta\theta_{exit,1} / \Delta n_1 \quad (2.9)$$

$$\alpha_j = (\Delta\theta_{exit,j}) / \Delta n_j = (2 \cdot \Delta\theta_{exit,j-1}) / \Delta n_j = (2^{j-1} \cdot \Delta\theta_{exit,1}) / \Delta n_j \quad (2.10)$$

In other words, each prism angle in an N-stage device can be calculated directly from the minimum desired angular separation $\Delta\theta_{exit,1}$. Utilizing this scheme, the set of prisms in Table 2.2 was obtained. Note that the smectic A blend

| Stage # j | $\Delta\theta_j$ radians | Liquid Crystal | $n_{e,j}$ | $n_{o,j}$ | α_j radians |
|--------------|-----------------------------|-------------------|-----------|-----------|-----------------------|
| 1 | 0.001007 | ZLI-2806 | 1.5183 | 1.4746 | 0.02304 |
| 2 | 0.002014 | ZLI-2806 | 1.5183 | 1.4746 | 0.04609 |
| 3 | 0.004028 | DnAOB Blend | 1.72 | 1.52 | 0.02014 |
| 4 | 0.008056 | DnAOB Blend | 1.72 | 1.52 | 0.04028 |
| 5 | 0.016112 | DnAOB Blend | 1.72 | 1.52 | 0.08056 |
| 6 | 0.032224 | DnAOB Blend | 1.72 | 1.52 | 0.16112 |
| 7 | 0.064448 | DnAOB Blend | 1.72 | 1.52 | 0.32224 |

TABLE 2.2. Prism Angles designed with the Doubled Sequence design method.

was not “used” for the first two stages. The reason for this will be given in the later section discussing device fabrication.

In order to show that this design approach is faulty, each deflection path through the N stage device was traced. As with the above design approach, this requires nothing more than Snell’s Law and a little trigonometry. However, now each possible deflection path must be traced along its entire transit through the assembled N -stage device. What is needed is a more general function for mapping input beam paths of arbitrary incidence through a particular stage. Because the prisms are birefringent, each input results in two possible outputs. The general mapping function is then used to compute all the possible output paths of a given stage, which serve as the inputs for the next stage. The process is repeated until exiting the device. In general, a linearly polarized laser beam entering the j^{th} stage at a particular incidence angle follows a path such as shown in figure 2.14. Assuming the glass and isotropic filler have a refractive index equal to the liquid crystal’s ordinary index, the relation between entry and exit angles is:

$$\theta_{out,j,i}(n_{o,i}, \theta_{out,j-1,i}, \alpha_j) = \sin^{-1} \left\{ \frac{n_{o,j}}{n_G} \sin \left[\sin^{-1} \left(\frac{n_G}{n_{o,j}} \cdot \sin(\theta_{out,j-1,i}) \right) + \alpha_j \right] \right\} - \alpha_j \quad (2.11)$$

$$\theta_{out,j,2^{j-1}+i}(n_{e,i}, \theta_{out,j-1,i}, \alpha_j) = \sin^{-1} \left\{ \frac{n_{e,j}}{n_G} \sin \left[\sin^{-1} \left(\frac{n_G}{n_{e,j}} \cdot \sin(\theta_{out,j-1,i}) \right) + \alpha_j \right] \right\} - \alpha_j \quad (2.12)$$

Here, the subscript $i=1$ to 2^{j-1} denotes the possible input paths to the j^{th} stage. Note that the same input path i can be mapped into two possible output paths, i and $i+2^{j-1}$, depending on whether the beam experiences the e- or o-mode of the liquid crystal inside the j^{th} stage’s prism. The values of α_j are those calculated from Eqns. (2.11) and (2.12).

Starting with a normally incident laser beam, i.e. $\theta_{out,0,1}=0$, and drawing from the prism angles calculated earlier, two output paths from the first stage are calculated, one from Eqn. (2.11) and the other from Eqn. (2.12). Both of those paths serve as input directions into the second stage. Eqns. (2.11) and (2.12) are each applied to both input directions, producing the four output paths of the second stage. The process is repeated through all N stages.

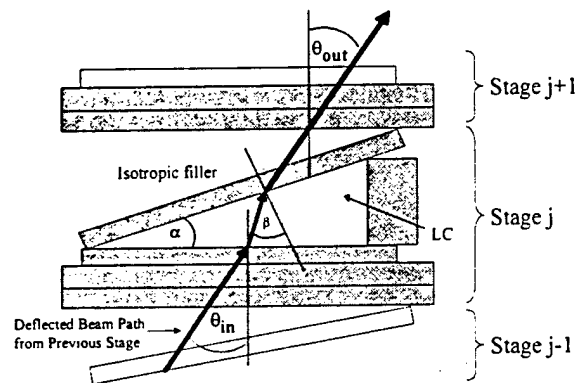


FIGURE 2.14 Interior Stage in an LCDLD. The general path of a beam through this device is shown.

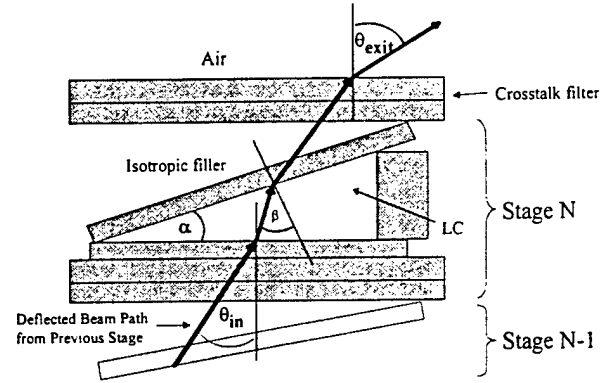


FIGURE 2.15 Final Stage in an LCDLD, showing a deflected beam exiting the device.

After computing all the propagation paths inside the N -stage device, the $2N$ output paths from the N^{th} stage are refracted out of the device, as shown in figure 2.15. The final calculation of the exit paths is simply:

$$\theta_{\text{exit},N,i} = \sin^{-1}\{n_G \sin(\theta_{\text{out},N,i})\}, \dots, \quad (2.13)$$

where $\theta_{\text{exit},N,i}$ are the 2^N deflection paths produced by the N -stage LCDLD.

This analysis was applied to the hypothetical 7-stage LCDLD listed in Table 2.2. It was assumed that the glass substrates and isotropic filler possessed the same refractive index, $n_G=1.5$. Steering angles were calculated with respect to the normally incident laser source. The results of this analysis are shown in figures 2.16, 2.17, and 2.18.

Figure 2.16 compares steering angles produced by the hypothetical LCDLD with the Doubled Sequence of prisms to an ideal LCDLD. The ideal LCDLD is one with a constant angular separation, equal to the far field divergence angle of a common HeNe laser (0.001007 radians, or 0.0577 degrees). For both the ideal and Doubled Sequence LCDLD's, steering angles are referenced to least deflected path. Steering angles are plotted against the numbered index of steering paths, ranging from least to most deflected path. Figure 2.16 shows that the Doubled Sequence device does not perform as desired, and the difference between it and an ideal device increases with deflection angle.

The difference between the ideal and Doubled Sequence steering angles is shown in figure 2.17. That difference increases discontinuously at regularly spaced locations within the deflection pattern. Each of these discontinuities occurs when a prism begins mapping input beam paths with its extraordinary refractive index. The Doubled Sequence of prisms produces steering "error" of approximately five beam diameters at its largest deflection. For some applications, this error may not be acceptable.

As mentioned earlier, another perspective on digital beam steering accuracy requires that each exiting deflection path be separated by the same amount from its neighboring paths. Figure 2.18 is a plot of angular separation across the entire deflection range of the Doubled Sequence device. The computed angular separations closely match the desired value of 0.0577 degrees over most of the deflection range. However, there are some locations within the field of view of this device at which angular separation significantly differs from the desired amount.

All of the above problems occur because the Doubled Sequence of prisms is not the optimal design for this device. The problems are not easily noticed if the angular range of such a device is limited to 2 degrees or so (see figure 2.16). The fact that each additional prism, with a larger angle than its predecessor, increases the steering error is caused by the design method, which assumes the small angle approximation of design formulae.

2.9.2. Nonlinear Sequence of Prisms. For more precise calculation of prism angles, one can forego the linear approximations employed above, and calculate exact prism angles by substituting Eqns. (2.6) and (2.7) into the exact form of Eqn. (2.8). This produces a nonlinear relation, which cannot be solved analytically for the prism angles. In order to solve for prism angles α , one may apply an iterative numerical technique such as the Newton method²⁹ (also called fixed-point iteration). Each prism angle in the sequence is calculated separately using such an approach, independent of the other wedges. This can be called a Nonlinear Sequence.

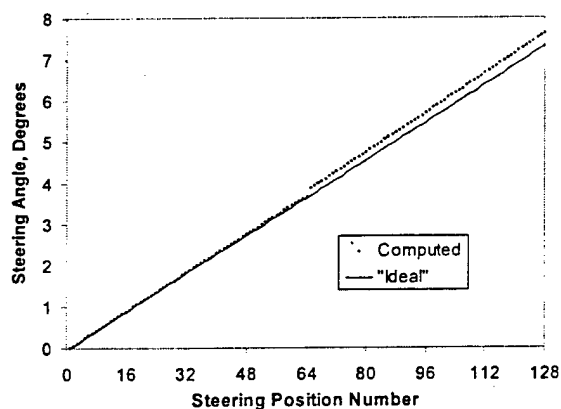


FIGURE 2.16 Computed Steering Angle at each Steering Position of a 7 stage LC-DLD with Sequence Doubled prism angles.

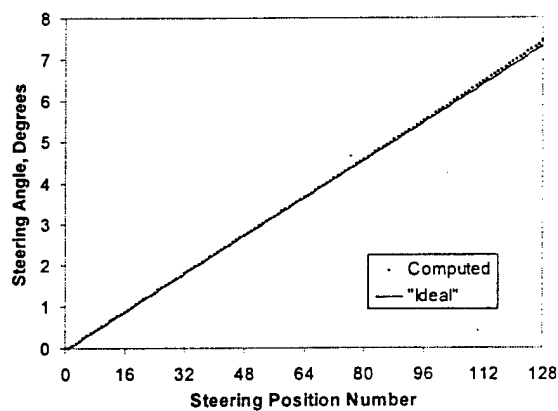


FIGURE 2.19 Computed Steering Angle at each Steering Position of a 7 stage LC-DLD with a Nonlinear Sequence of prism angles.

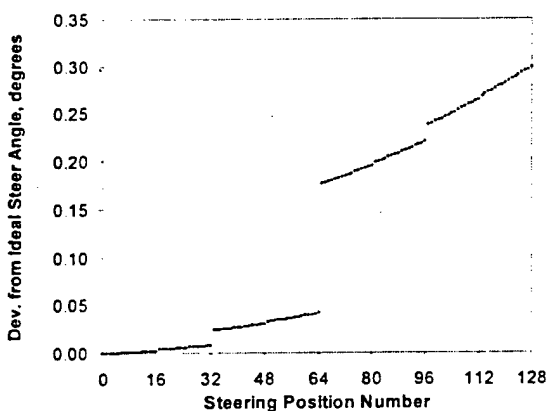


FIGURE 2.17 Computed Steering Angle at each Steering Position of a 7 stage LC-DLD with Sequence Doubled prism angles.

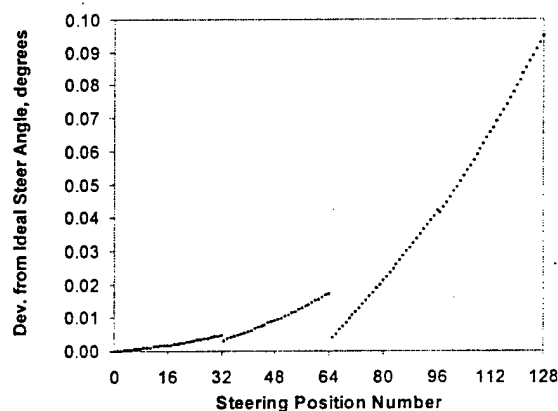


FIGURE 2.20 Computed Angular Separations over the angular range of a 7 stage LC-DLD with a Nonlinear Sequence of prism angles.

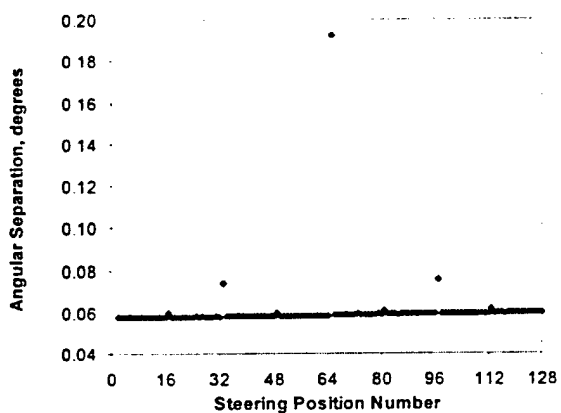


FIGURE 2.18. Computed Angular Separations over the angular range of a 7 stage LC-DLD with Sequence Doubled prism angles.

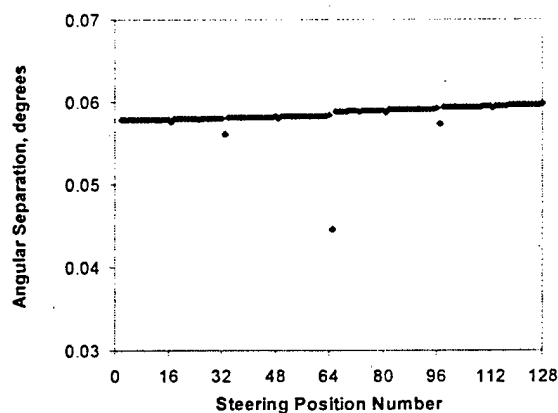


FIGURE 2.21. Computed Angular Separations over the angular range of a 7 stage LC-DLD with a Nonlinear Sequence of prism angles.

This approach was applied to the same set of liquid crystals and desired angular separation as in the Doubled Sequence approach. The result was another hypothetical set of prisms, which are listed further on in Table 2.3.

This Nonlinear Sequence LCDLD was then subjected to the same raytrace analysis as described above for the Doubled Sequence device. The results shown in figures 2.19, 2.20, and 2.21 indicate a much more accurate device.

2.9.3. Integrated Design of the Prism Sequence. There is still some error in this Nonlinear Sequence LCDLD, and it appears the problem will increase with increasing angular range. In order to effect further improvements, some aspects of the preceeding device architecture must be abandoned.

Up to this point, the device architecture was assumed to take a rather simple form shown in figures 2.1 through 2.4. Prisms were oriented with one face lying flat on the polarization rotation switch for that stage. The cascaded device was built from those binary switch building blocks requiring that the entry face of all prisms be parallel, and the prism vertices all on the same "side" of the device's longitudinal axis.

Three changes were made in this basic device architecture. Each change is a tactic aimed at reducing incidence angles of deflection paths at dielectric discontinuities. The effect of each tactic is to move the optics back toward the small angle approximation, where deflection is linearly related to prism angle. All three changes can be incorporated into a new quantifiable design computation.

The first change is to alternate prism vertices about the DLD longitudinal axis. Another tactic is to tilt each prism within its stage. A third tactic is to reduce prism angles slightly below their Doubled Sequence values. This tactic made the Nonlinear Sequence design more accurate than the Doubled Sequence of prisms. A DLD constructed with this new architecture would look something like the drawing in figure 2.22.

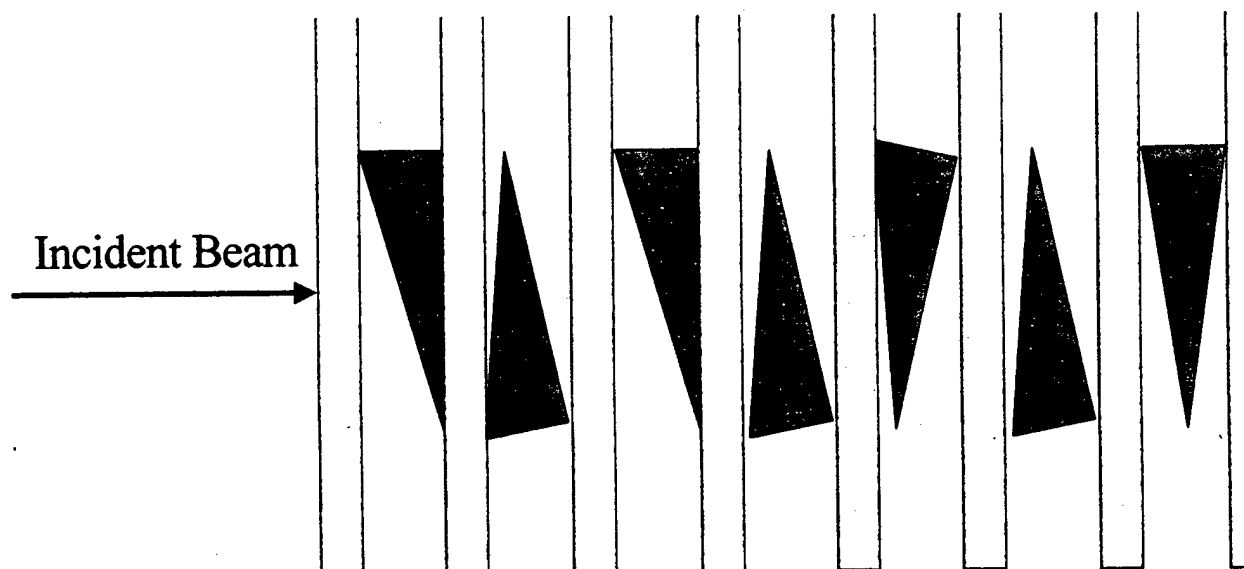


FIGURE 2.22 Drawing of seven stage LCDLD constructed with Integrated Design architecture.

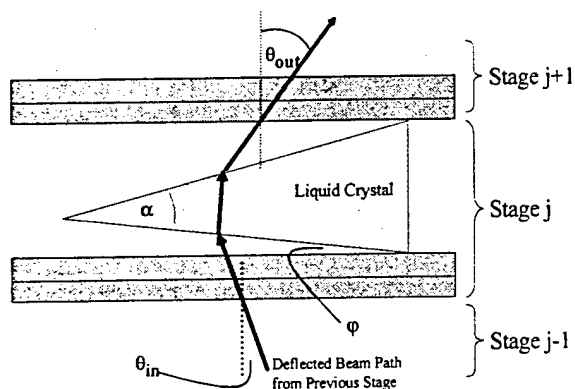


FIGURE 23. Single Stage LC-DLD. The two possible deflection paths through this device are shown.

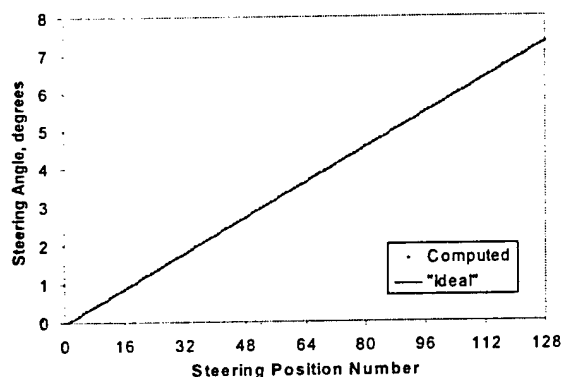


FIGURE 24. Computed Steering Angle at each Steering Position of a 7 stage LC-DLD with Optimized prism angles and prism tilts.

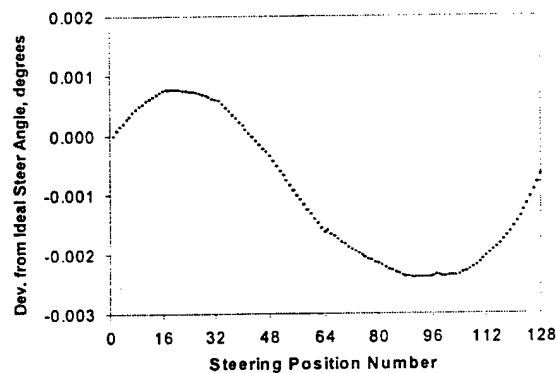


FIGURE 25. Computed Steering Angle at each Steering Position of a 7 stage LC-DLD with Optimized prism angles and prism tilts.

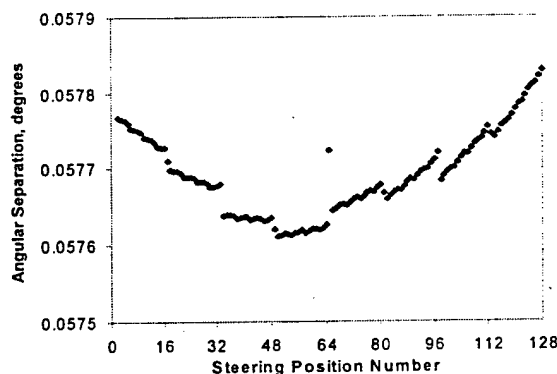


FIGURE 26. Computed Steering Angle at each Steering Position of a 7 stage LC-DLD with Optimized prism angles and prism tilts.

The first step in this new design process is to obtain a new mapping function to describe how each stage processes all of the possible deflection paths resulting from the previous stage. From the drawing in figure 2.23, the following mapping function can be derived:

$$\theta_{out,j,i} = \sin^{-1} \left\{ \frac{n_{lc,j}}{n_G} \sin \left[\sin^{-1} \left(\frac{n_G}{n_{lc,j}} \sin [\theta_{out,j-1,i} - \varphi_j] \right) + \alpha_j \right] \right\} - \alpha_j + \varphi_j \quad (2.14)$$

where the subscript j indicates the sequential stage number, i denotes the index for input and output path, α is the prism angle, φ is the tilt of that prism within its stage, and the $n_{lc} = n_o$ when an ordinary mode transit is being considered, or n_e for an extraordinary mode transit.

Employing Eqn. (2.14) for each stage in the sequence, all of the possible output steering angles can be obtained. Then, as before, application of Eqn. (2.13) yields the exit paths. Next, the angular separation between any two adjacent steering directions can be calculated:

$$\Delta\theta_{exit,N,i} = \theta_{exit,N,i+1} - \theta_{exit,N,i} \quad (2.15)$$

Here, the subscript i indicates the relative position of a deflection path within the composite DLD's exit-side deflection pattern. For an N -stage device, there will be 2^N-1 values of $\Delta\theta_{exit,N,i}$. From these, the RMS value of the deviation of all $\Delta\theta_{exit,N,i}$ from the intended value (e.g. the laser beam divergence angle) is calculated for a given set of prism angles and tilts. This is the device's RMS steering error $\Delta\theta_{RMS}$.

The goal of this process is to find the set of prism angles and tilts which minimize the device's net RMS steering error. In other words, the characteristic RMS steering error function of an N -stage DLD is minimized with respect to its $2N$ variables (the prism angles and tilts). This cannot be done analytically, so a numerical technique was employed. Of the available methods for minimizing a function with respect to multiple variables, we chose a simple successive line minimization technique³⁰. This method is less robust than methods such as the conjugate gradient method, but was chosen because it was easier to encode. One should be wary when employing this method, however, because it can prove nonconvergent. Problems can generally be avoided if the convergence tolerance is not too small.

The approach to device design treats all internal prisms as contributing factors to any one external deflection path. This is particularly important if the liquid crystal in a particular prism has both its ordinary and extraordinary refractive indices unequal to that of the substrates and index-matched filler. When that is so, any prism will deflect *all* of the paths processed through it. As a result, all of the external steering directions will depend on all of the prism angles and orientations. Because the optimum angles and orientations of all prisms are interrelated, this approach is called the Integrated design method.

| Stage Number | n_o | n_e | Sequence Doubled Prism angle α , radians | Nonlinear Sequence Prism angle α , radians | Integrated Design Prism angle α , radians | Integrated Design Prism tilt ϕ , radians |
|--------------|--------|--------|---|---|--|---|
| 1 | 1.4746 | 1.5183 | 0.02304 | 0.02304 | 0.02302 | 0.02299 |
| 2 | 1.4746 | 1.5183 | 0.04609 | 0.04605 | 0.04603 | 0.03889 |
| 3 | 1.52 | 1.72 | 0.02014 | 0.02014 | 0.02012 | 0.02012 |
| 4 | 1.52 | 1.72 | 0.04028 | 0.04025 | 0.04024 | 0.01237 |
| 5 | 1.52 | 1.72 | 0.08056 | 0.08034 | 0.08039 | 0.06634 |
| 6 | 1.52 | 1.72 | 0.16112 | 0.15939 | 0.16046 | 0.05410 |
| 7 | 1.52 | 1.72 | 0.32224 | 0.22482 | 0.22860 | 0.13648 |

TABLE 3. Computed Design Specifications for Prism Angles and Prism Tilt Angles for Three Design Methods

This Integrated approach was applied to the same set of liquid crystals and desired angular separation as in the both prior design methods. That hypothetical set of prisms and their orientations is listed in Table 2.3.

This Integrated LCDLD was then subjected to the same raytrace analysis as described above for the Doubled Sequence device. The results shown in figures 2.24, 2.25, and 2.26 indicate an extremely accurate device.

2.9.4. Design Results. The three design methods described above were each applied to the same desired angular separation and liquid crystals. The resulting design specifications are listed side-by-side in Table 2.3.

As it turns out, the DnAOB blend is not capable of forming defect-free prisms with internal angles larger than approximately 0.14 radians. So the full extent of the advantages of the Nonlinear and Integrated design approach discussed above cannot yet be demonstrated. Nevertheless, the approach to design discussed in previous sections can serve as a prescription for design should improved materials be developed.

2.10. Beam Steering Device - Fabrication

In order to demonstrate the utility of a prismatic digital light deflector utilizing smectic A materials, a working prototype was assembled.

The angular separation between adjacent deflection positions was arbitrarily chosen to be twice the far field divergence angle of a common laboratory helium-neon laser (i.e. 2×0.001007 radians).

As was mentioned above, the stacked prismatic architecture can be a source of steering error at large deflection angles. For LCDLD devices with small angular range, 2 degrees or less, this problem is not significant. Nevertheless, the design method described above was utilized to calculate optimal prism angles and orientations for a four-bit (16-position) beam steering device with an angular range of 1.72 degrees. The resulting design specifications appear in Table 2.4:

| Stage Number | Material | n_o | n_e | Wedge angle α , radians | Wedge tilt ϕ , radians |
|--------------|-------------|--------|--------|--------------------------------|-----------------------------|
| 1 | ZLI-2806 | 1.4746 | 1.5183 | 0.04603 | 0.03889 |
| 2 | DnAOB Blend | 1.52 | 1.72 | 0.02012 | 0.02012 |
| 3 | DnAOB Blend | 1.52 | 1.72 | 0.04024 | 0.01237 |
| 4 | DnAOB Blend | 1.52 | 1.72 | 0.08039 | 0.06634 |

TABLE 2.4. Computed Design Specifications for Prism and Tilt Angles for a four-stage Prismatic LCDLD.

The first stage need only possess a characteristic deflection of approximately 0.002 radians. If the prism in this stage is filled with the DnAOB blend ($\Delta n=0.2$), the prism angle will be very small and difficult to produce with much precision. Consequently, the prism in the first stage was designed for and filled with the nematic blend Merck

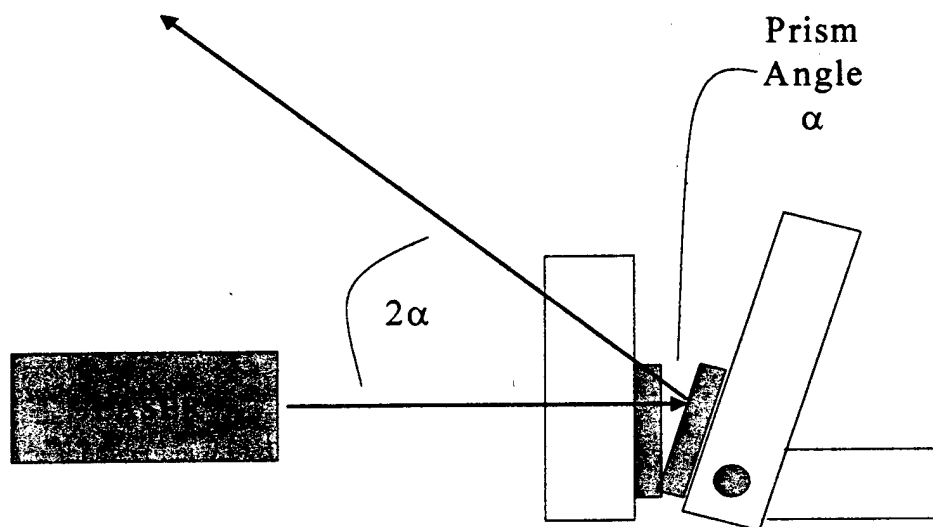


FIGURE 2.27 Apparatus for fabrication of prisms. Prism substrates form an angle α .

ZLI-2806. Even when filled with the much lower birefringence nematic, the prism angle is still small, and the liquid crystal layer in the prism is only 1mm thick at a distance of 10mm from the wedge vertex. For this low-birefringence nematic, scattering is not a problem for such an optical pathlength.

The remaining three prisms were filled with a 50:50 (by weight) mixture of the $n=6$ and $n=7$ homologues of DnAOB.

An apparatus (shown in figure 2.27) was constructed to control the prism angles during fabrication. This eliminated the need to machine custom spacers for each prism and locate those spacers at the precisely required distance from the wedge vertices (not an easy task when assembling manually).

Fabrication of the four-stage demonstration device was as follows:

1. The angular separation between adjacent deflection positions was chosen to be twice the far field divergence angle of a common laboratory helium-neon laser (2×0.001007 radians).
2. Choice of materials. The prism of the first stage was to be filled with a low birefringence nematic liquid crystal, Merck ZLI-2806 which possesses a birefringence of $\Delta n=0.04$. The remaining three prisms were filled with a 50:50 (by weight) mixture of the $n=6$ and $n=7$ homologues of DnAOB (Di-n-alkyl-azoxybenzene) which possesses a birefringence of $\Delta n=0.2$.
3. The Integrated Design principles described above were utilized to design a four stage (four binary deflection switches) cascaded device.
4. The prisms were fabricated with the design-specified angles. Each consisted of two glass substrates, coated with DuPont polyimide PI-2555. The polyimide surfaces were rubbed mechanically to induce orientation of the liquid crystal filler. The two substrates were adhered together in a wedge-configuration (utilizing apparatus

shown in figure 2.27), with the rub directions of the two substrates antiparallel to each other but parallel to the wedge vertex. These wedge cells were then filled with the prescribed liquid crystal filler.

5. The prism containing the low-birefringence nematic liquid crystal (Merck ZLI-2806) was filled and sealed without additional processing.
6. Prisms containing the smectic A liquid crystal were filled and heated into the nematic phase in order to produce the desired orientation of liquid crystal. The prisms were then cooled slowly into the smectic A phase. This procedure worked well for prism angles up to approximately 0.14 radians. Smectic prisms with steeper angles contain too many defects to be useful (that is why we limited the angular range of our prototype to 1.72 degree; the practical limit for this DnAOB-based device is approximately 2 degrees).
7. Twisted-nematic (TN) cells were fabricated for use as the polarization rotators.
8. Each prism was affixed to a TN cell, not abutting the TN cell as shown in figures 2.1 through 2.4, but at the design-specified angle listed in Table 2.4 (and depicted crudely in figures 2.22 and 2.23).
9. These four stages were then affixed to each other at complementary angles, the result being that all TN cell substrates were parallel to each other. In addition, the optic axes of the four birefringent prisms were aligned parallel to each other. The stages were affixed in increasing order of their characteristic deflection angles.
10. All gaps were filled with Norland 65, used for index matching to reduce Fresnel reflections at glass surfaces.
11. As with some of the prior art^{15,16,19}, an additional filtering stage was added, consisting here of a fifth TN cell and a dichroic linear polarizing film. Crosstalk is defined as leakage of the beam into undesired steering deflections. This problem stems from imperfect fabrication. The most intense crosstalk is polarized in a plane perpendicular to that of the selected deflection. The filter blocks that part of the crosstalk noise.

2.11. Beam Steering Device - Experimental Results

A randomly polarized Helium-Neon laser (632.8nm) was directed at the prismatic light deflector's entry surface (at normal incidence). A dichroic linear polarization film was interposed between the laser and the entry surface, oriented with its "transmission axis" parallel to the optic axes of the prisms. With each possible permutation of the four stages' TN cells being turned on or off (i.e. rotating or not rotating the light incident upon them), the transmitted beam was deflected in one dimension. Angular separation of each deflection position was roughly constant throughout the angular range of the device, although this has not yet been measured.

The transmitted intensity at each of the 16 possible deflection positions was measured and normalized to the intensity of the beam after passing through the initial dichroic linear polarizing film. These results are shown in figure 2.28. Photographs of the device and its operation are shown in figures 2.29 through 2.34.

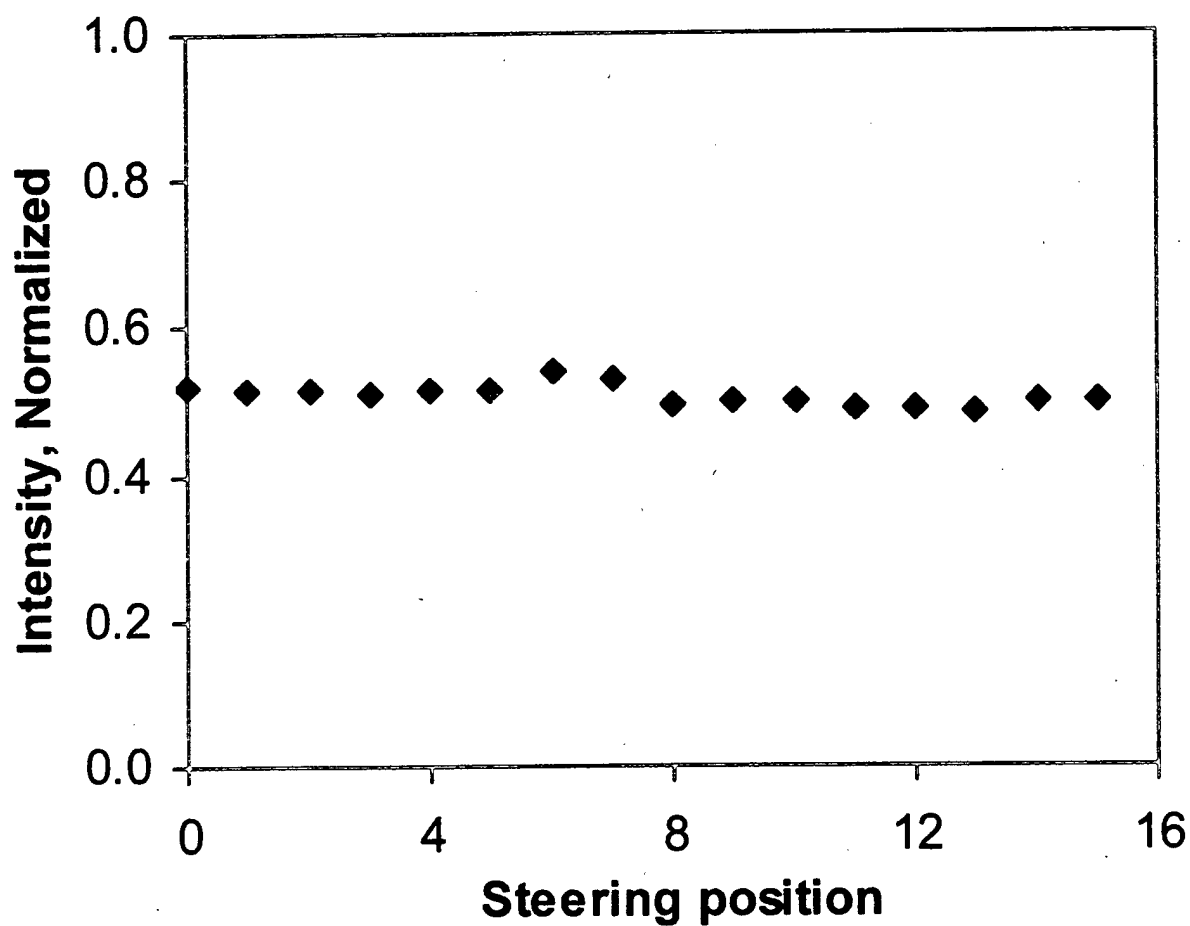


FIGURE 28. Transmitted intensity, as a function of deflection position, four-stage LCDLD. Intensity is normalized to that of the linearly polarized source. Position 0 is the least deflected, position 15 the most deflected (1.72 degrees from position 0).



FIGURE 2.29 View of four stage LCDLD, from above.



FIGURE 2.30 Side view of four stage LCDLD.

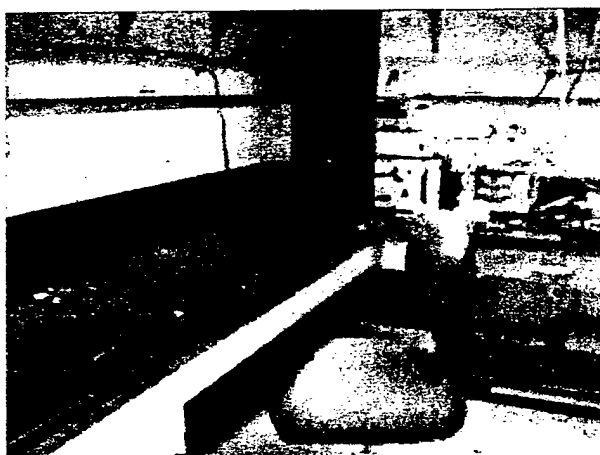


FIGURE 2.31 Least deflected output of four stage LCDLD, at distance of 2 meters.



FIGURE 2.32 Most deflected output of four stage LCDLD, at distance of 2 meters.

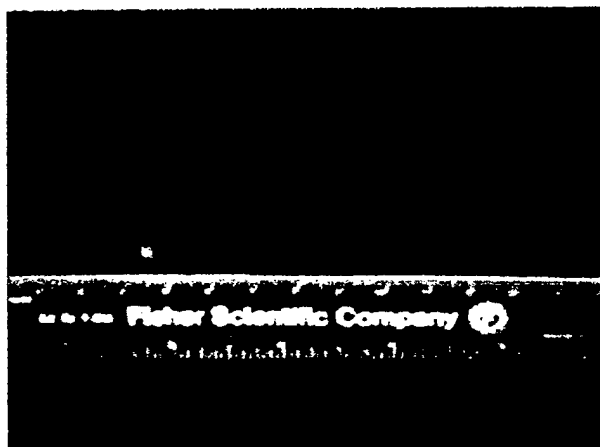


FIGURE 2.33. Close-up of least deflected output of four stage LCDLD, at distance of 2 meters.

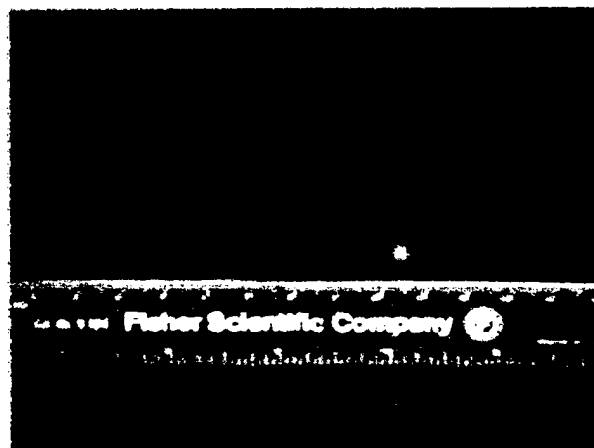


FIGURE 2.34. Close-up of most deflected output of four stage LCDLD, at distance of 2 meters.

2.12. Conclusions – Prismatic Liquid Crystal Beam Steering Device

- We have assembled a working prototype of a prismatic liquid crystal beam steering device, also known as the liquid crystal digital light deflector (LCDLD). It deflects an incident laser beam through an angular range of 1.72 degrees with almost uniform intensity.
- Our research has uncovered a class of liquid crystalline material which, when used as the filler for passive birefringent deflecting prisms, can overcome the scattering problem related to nematic materials.
- We have used one of these nonpolar smectic A materials (actually, a blend) in our prototype.
- But even this material has its limits. Increasing the device's angular range beyond approximately 2 degrees requires increasing prism angles beyond this particular material's defect-free limits. As the prism angle increases, increasing separation of substrates opposite the wedge vertex permits focal conic defects to form.

- We have developed a design method that can provide for accurate wider angle steering if the focal conic defects can be circumvented.
- Additional research may uncover other room temperature nonpolar smectic A materials with increased birefringence (tolanes, for example) so that smaller prism angles can be used, thereby extending angular range.
- Refined fabrication techniques (smoother and cleaner surfaces, smectic A materials with fewer impurities) which can reduce the nucleation of focal conic defects, thereby extending angular range.
- Alternate deflecting elements (stacked prisms within a particular stage, static liquid crystal-filled surface relief gratings, stacked smectic A liquid crystal polymer films possessing a gradient in effective extraordinary refractive index) may also extend the angular range.
- It is possible to increase angular range by making liquid crystal Wollaston-type prisms (figure 2.35), but it is not easy to fabricate defect-free SmA cells with optic axis perpendicular to prism vertex. This difficulty increases with the prism angle (i.e. larger L/A ratio).

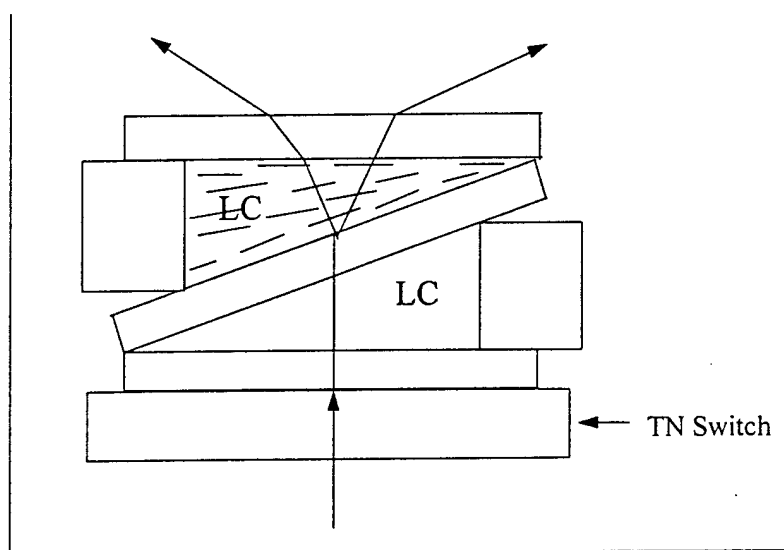


FIGURE 2.35 "Two Position" Switch. Upper wedge is liquid crystal aligned perpendicular to wedge vertex. In lower wedge, liquid crystal alignment is parallel to wedge vertex.

3. COMPUTATIONAL SIMULATION OF DIFFRACTIVE LIQUID CRYSTAL GRATINGS

3.1 Introduction

The previous chapter dealt with a prismatic digital light deflector employed for steering beams. A variety of other liquid crystal structures are under investigation for their potential use in beam steering devices. These include cholesteric diffraction gratings^{6,7}, and optical phased arrays^{4,5}. While experimental research provides some insight into the behavior of such beam steering technologies, additional information can be obtained from computer simulation. In addition, reliable computer simulations can reduce the experimentation necessary to optimize device performance.

This chapter covers the development of software capable of simulating the performance of diffractive liquid crystal beam steering devices.

Computer simulation of diffractive liquid crystal devices can be separated into three distinct steps. First, the spatial variation of the liquid crystal director (i.e. of the dielectric tensor) inside the device must be obtained. That data serves as input for a second computation, which obtains the near field transmitted through or reflected from the liquid crystal structure. The near field is defined as the electromagnetic field existing on or just outside the exit surface of the liquid crystal layer being analyzed. The near field data is then transformed into the far field by a third computational step.

For diffractive liquid crystal beam steering devices, the goal of this three-step process is to compute the diffraction pattern resulting from illumination of the liquid crystal structure. In the case of beam steering devices, the objective is to simulate yields theoretical steering performance of a hypothetical device.

In the past, simulations of diffractive liquid crystal beam steering devices have been based on simplified models of director orientation in, light propagation through, and diffraction from liquid crystal devices^{5,31}. Those studies have not included accurate modeling of liquid crystal director variations near electrode edges caused by fringing fields. In addition, the wave nature of light was ignored when obtaining the electromagnetic fields transmitted through the inhomogeneous anisotropic structure. Finally, those studies employed the Fraunhofer approximation of near to far field transformation, thereby restricting accuracy to the paraxial region and for diffracting features much larger than a wavelength.

Here we discuss computational tools capable of more accurate analysis of diffractive liquid crystal structures with two-dimensionally varying director distributions.

There is an added benefit to the development of the near and far field optical simulation tools discussed in this chapter. The near field method is generally applicable to most two-dimensionally inhomogeneous anisotropic dielectric structures. The far field method is of use with any accurately determined aperture surface fields. Hence, these two computational tools can be used to analyze optical performance of other liquid crystal devices, such as individual or multiple pixels within a liquid crystal display or spatial light modulator.

The text of this chapter proceeds as follows. First is a description of the phased-array liquid crystal gratings which are employed in beam steering applications. Next is a discussion of computation of the liquid crystal director distribution in such a device. Then a near field calculation technique is described. This is followed by a discussion

of the transformation of the near fields into a far field diffraction pattern. After some conclusions, the current version of the source code is listed in an appendix.

3.2 Liquid Crystal Blazed Grating for Beam Steering

A simple hypothetical device for steering optical beams by means of phase retardation is a prism with adjustable height (Figure 3.1). Because of the linearly increasing thickness of the prism, the phase of an incident plane wave is retarded in a linearly increasing fashion across the wave front. Upon emerging from the prism, the propagation direction of the incident plane wave has been deflected. If the prism's angle can be altered upon demand, the deflection angle can be "tuned".

Making use of the ability of liquid crystals to reorient under the influence of an applied electric field, such a device can be fabricated from a uniformly thick liquid crystal layer⁴. The device consists of electrodes deposited on a pair of parallel glass plates, into which a liquid crystalline material is filled. A continuous transparent electrode is deposited on one of the plates and a series of closely spaced electrodes on the other. The adjustable linear phase profile is then encoded by means of properly chosen voltages at each of the closely spaced electrodes. However, in order for such a device to deflect an incident laser beam over a wide angular range, the liquid crystal device must be quite thick. In the process, several problems would be encountered. First, owing to the thickness, some portion of the incident light beam would be lost to scattering. The second problem is that such a device would change deflections very slowly due to the thickness of the liquid crystal layer.

The latter problem has been noted and solved by other investigators^{4,5}. Switching time was shortened by reduction of the layer thickness. In this liquid crystal layer electrodes are employed to encode a blazed phase profile instead of the unbroken linear phase ramp of a prism. The width of a blaze dictates the angular deflection an incident beam. A section of such a device is depicted in Figure 3.2. The continuous linearly varying differential phase retardation profile is ideally broken into the familiar sawtooth pattern (Figure 3.3), "reset" from an integer multiple of wavelengths to zero periodically in one direction across the liquid crystal layer. Unfortunately, the elastic nature of nematic liquid crystalline materials prevents such a sharp transition. Instead, as is crudely depicted in Figure 3.4,

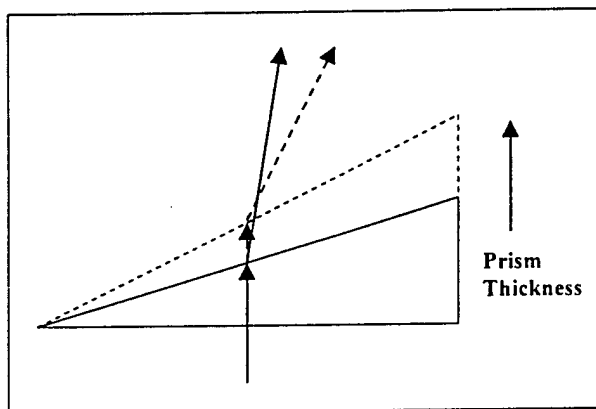


FIGURE 3.1 Hypothetical prism with adjustable height. Shows two heights and the resulting deflected paths of normally incident beam.

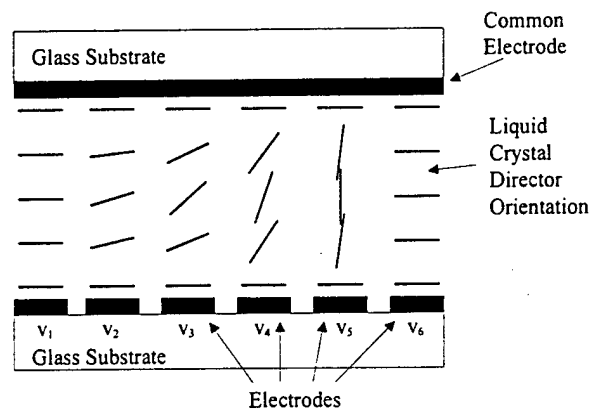


FIGURE 3.2 Encoding a single blaze onto a layer of liquid crystal. Phase reset located between V_5 and V_6 is an integer multiple of wavelength.

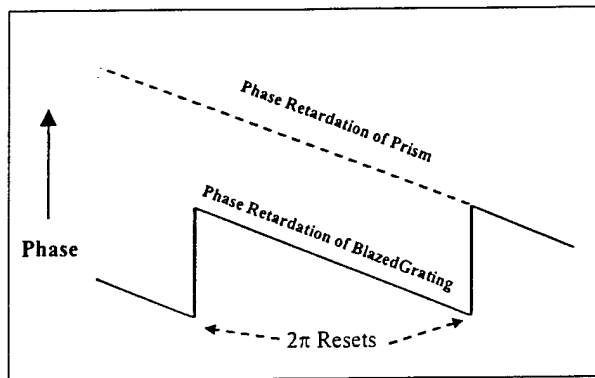


FIGURE 3.3 Reduction of linear phase ramp at each integer multiple of 2π elevation.

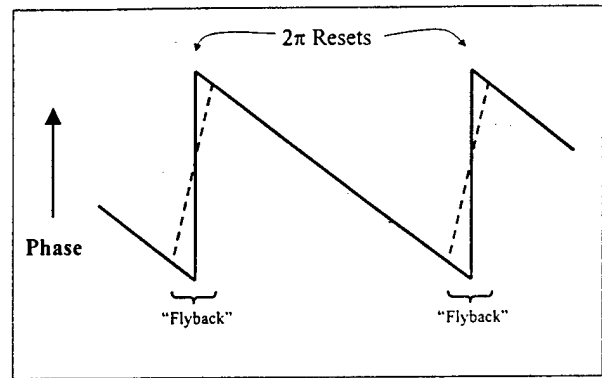


FIGURE 3.4 Rough depiction of "blurred" reset in a liquid crystal region (dashed lines).

this transition between two very different liquid crystal director orientations occurs over some finite distance in order to minimize the energy of the distortion. This non-ideal reset region has been referred to as "flyback"⁴. These flyback regions deflect some of the incident light away from the desired direction.

3.3 Liquid Crystal Director Simulation

A number of studies have examined the performance of these devices experimentally^{4,5,32} and via computer simulation^{4,5,31}. These earlier simulations employed simple models of the liquid crystal inside the blazed grating. The simple models were used as the basis for near and far field optical simulations of the gratings.

One such model assumes the liquid crystal orientation varies linearly and smoothly within each blaze, which would produce transmitted plane waves with a smooth linear phase ramp. Phase stair stepping, which might result from the influence of discretely patterned electrodes on the spatial mapping of liquid crystal director, is ignored. Between each blaze is the reset region. The director orientation in the reset region is not clearly defined.

The other model is based on the concept of independently quantized phase shifters⁴. In this model, a one-dimensionally varying liquid crystal director is associated with each electrode. The variations are in a direction perpendicular to the glass substrates enclosing the liquid crystal. Each such region is held to be independent of the state of other electrodes. In this model phase stair stepping is exaggerated. No clear definition of the reset region is given in this model either.

Neither model provides an accurate description of the physics of liquid crystals under the influence of external fields. Nevertheless, accurate optical simulations have been rendered for at least small deflection angles⁴. In such a case, the individual blazes are defined by many electrodes and are much wider than the reset regions. The discrete of discrete electrodes would not then be obvious. Inaccurate assumptions about the nature and impact of the reset regions (i.e. flyback) would not figure prominently in simulations of optical performance.

If, on the other hand, one wishes to simulate the performance of such a device in a state which produces a large angular deflection of incident light, the validity of those two simple models is questionable. In this state, each blaze may be produced by as few as three electrodes⁴. The influence of electrodes and reset regions would then be more

noticeable. Accurate simulation of the grating in this state may require more precise specification of the liquid crystal director distribution.

Methodology for modeling of two- and three-dimensional liquid crystal director configurations has been developed elsewhere³³. Given the applied external fields and a specific geometry, computations utilizing this method numerically converge to the director distribution which minimizes the free energy. The results in this chapter make use of that technique. Further details of liquid crystal director modeling will not be discussed here. The remainder of this chapter assumes such data can be obtained. Instead, here we concentrate on calculating the near and far fields resulting from illumination of properly modeled liquid crystal structures.

3.4 Near Field Simulation (of Liquid Crystal Gratings)

Assuming one has obtained an accurate mapping of the liquid crystal director everywhere inside the grating device, the next step in the simulation is to compute the electromagnetic fields transmitted through the layer.

Prior simulations of blazed liquid crystal phase gratings have assumed a rather simple geometrical optics model of light transmission through the liquid crystal layer. Normally incident light entering the layer at a given point is propagated through the entire layer in the same direction and retarded by an amount depending on the liquid crystal orientation along that "ray" path. The model ignores distortion of waves propagating through the layer caused by variations of dielectric properties parallel to the layer. Such a model can be reasonably accurate for a device in a state producing a small deflection angle, in which variations of the dielectric tensor parallel to the layer surface occur gradually throughout most of the grating.

However, large steering angles require significant variations of the dielectric tensor parallel to the layer surface. The influence of the reset regions and finite-sized electrodes is then prominent. In and near these areas the dielectric tensor undergoes significant spatial variations parallel to the grating surface. Plane waves entering the layer will be distorted.

The simple geometric optics near field model ignores the true wave nature of light propagation through a two-dimensionally inhomogeneous anisotropic medium. What is needed is a means of computing electromagnetic fields transmitted through such structures.

3.5 Optical Modeling of Liquid Crystals

In the past, optical simulations of liquid crystal structures have been dominated by "one-dimensional" methods, such as the extended Jones method³⁴ and the Berreman 4 X 4 matrix method³⁵. These methods are restricted to or designed specifically for simulations of inhomogeneous liquid crystal (anisotropic) structures with variations of the liquid crystal director in only one direction, perpendicular to the glass substrates enclosing the liquid crystal.

Liquid crystal devices may also include some regions in which the liquid crystal director (i.e. the dielectric tensor) also varies in a direction parallel to the glass substrates. Those variations are caused by effects such as disclinations (e.g. reverse tilt in a TN) and fringe field areas near the edges of electrodes.

In a low-resolution liquid crystal device, the individually tuned electrodes are large compared to areas covered by disclinations and fringing fields. The contribution of those regions of distorted dielectric properties to the total optical performance of the device can be ignored. As a result, the above-mentioned one-dimensional optical simulation methods can be satisfactorily employed for optical analysis of relatively simple low-resolution liquid crystal devices.

In general, the current trend is toward liquid crystal devices with smaller gaps separating smaller electrodes. In a blazed-phase grating, this permits reduction of the blaze width and increase in allowable steering angle. In a display, this permits higher image resolution. In addition, some recently developed liquid crystal structures, such as some of the In Plane Switching modes (IPS), purposefully make use of fringing fields.

These developments have a cost. Disclinations and fringing field regions contribute more significantly to net optical performance. Furthermore, the smaller size and closer spacing of electrodes may also increase the significance of some heretofore-ignored diffractive effects.

Therefore, methodology for computer simulation of the optical performance of these newer high-performance liquid crystal structures must also evolve.

There have been some attempts to extend the use of the one-dimensional methods to two and three dimensions. One such technique involves dividing the structure into layers and columns. Each column is regarded as an independent one-dimensional structure. One of the one-dimensional methods is then applied to each column. However, such adaptation of one-dimensional techniques to two-dimensional problems cannot properly take into account lateral scattering of light propagating within the liquid crystal structure. Nor can those methods accurately calculate oblique propagation light through a liquid crystal structure with director variations in more than one dimension.

For these and other reasons, near field optical modeling of such structures requires a more robust computational method. Among the two-dimensional computational methods, our work is concentrated on the Finite-Difference Time-Domain (FDTD). FDTD makes use of direct discretization of Maxwell's equations³⁶, without any of the simplifications which permitted development of the one-dimensional methods. Because of this, the FDTD method can accommodate multidimensional inhomogeneity of the dielectric tensor.

3.6 Finite-Difference Time-Domain Method

3.6.1 Introduction. The FDTD method provides an avenue toward optical simulation of liquid crystal devices with multi-dimensional inhomogeneities of director orientation. These conditions occur in liquid crystal microdisplays, some diffractive liquid crystal devices, and in existing liquid crystal displays such as those employing in-plane switching. In future comparisons with far-field results of one-dimensional optical techniques applied to these problems, the one-dimensional methods may well prove equal to the task. However, without very precise experimental methods or a tool such as FDTD, that cannot be known.

The FDTD method is capable of directing plane waves or gaussian beams at arbitrary incidence onto a liquid crystal structure. After a series of numerical calculations, transmitted and reflected responses can be collected. Those

responses can be utilized to compute transmitted and reflected intensities along the surface of a liquid crystal pixel or can be transformed into the far field (i.e. diffraction).

As an illustration of the ability of FDTD to simulate a variety of optical problems, Figure 3.5 shows the interference pattern resulting from two oscillating dipoles placed on an FDTD grid.

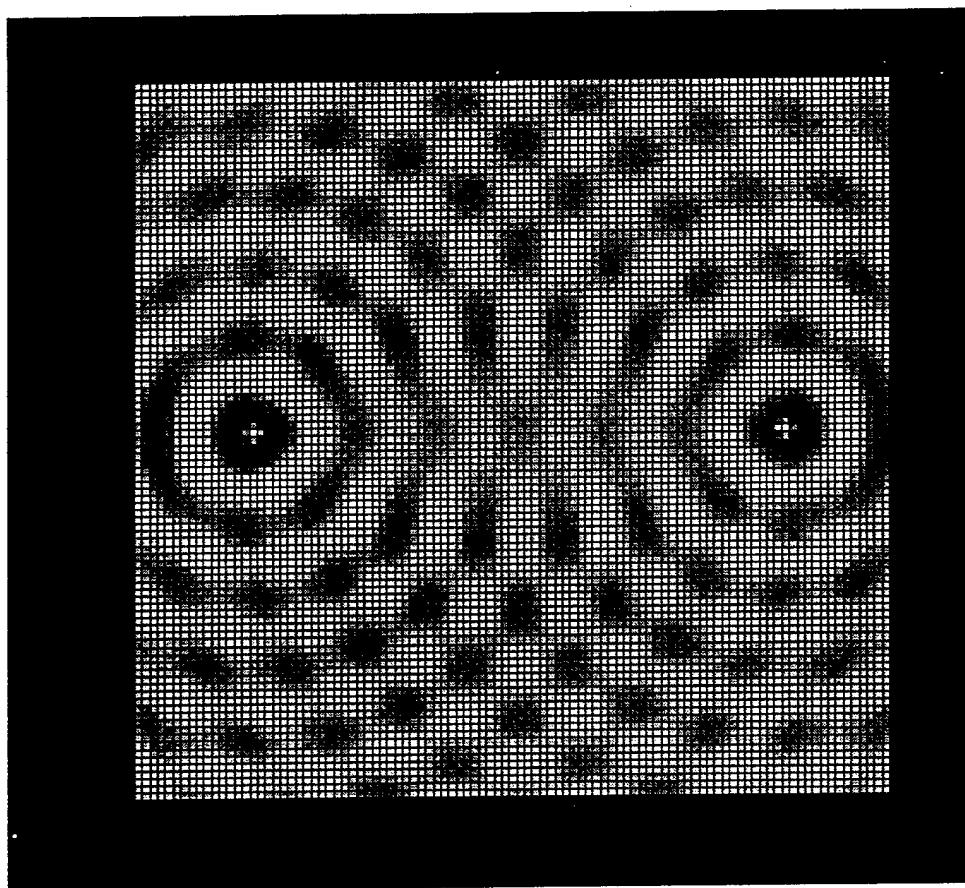


FIGURE 3.5 FDTD Simulation of Two Interfering Dipoles. Grey-scale plot of instantaneous electric field magnitude at one point in time. Dark and light regions indicate positive and negative field magnitudes.

3.6.2 How the Finite-Difference Time-Domain (FDTD) Method Works. The FDTD method has been in use in the electrical engineering community for years, but has only recently been applied to liquid crystal structures³⁷. At the heart of the FDTD method is the spatial discretization of the structure to be analyzed, and the use of central finite differences to approximate the derivatives in the differential form of Maxwell's equations. An oscillating wave source is introduced into the grid and "directed" at the structure to be analyzed. The entire grid is then time-stepped until steady state response oscillations are obtained at all points on the grid.

The following sections outline the implementation of this method. Some of the descriptions herein borrow from Taflove's book³⁸ and other sources which will be referenced. For a more thorough treatment, the reader should refer to Taflove's book.

The mechanism by which the FDTD method works can be illustrated by reducing the three dimensional differential form of Maxwell's equations to a simple one-dimensional isotropic case. We begin with Maxwell's equations, which can be written, for sourceless homogeneous linear isotropic media:

$$\frac{\partial \mathbf{E}(\mathbf{r})}{\partial t} = \varepsilon^{-1} \cdot [\nabla \times \mathbf{H}(\mathbf{r})] \quad (3.1)$$

$$-\frac{\partial \mathbf{H}(\mathbf{r})}{\partial t} = \mu_0^{-1} \cdot [\nabla \times \mathbf{E}(\mathbf{r})] \quad (3.2)$$

where ε is the dielectric constant. The use of the magnetic permeability μ_0 implies a nonmagnetic medium. $\mathbf{E}(\mathbf{r})$ and $\mathbf{H}(\mathbf{r})$ are the spatially varying electric and magnetic vector fields inside the medium. These two vector equations at a given location can be written as the following six scalar partial differential equations:

$$\frac{\partial E_x}{\partial t} = \varepsilon^{-1} \cdot \left[\frac{\partial H_z}{\partial y} - \frac{\partial H_y}{\partial z} \right] \quad (3.3)$$

$$\frac{\partial E_y}{\partial t} = \varepsilon^{-1} \cdot \left[\frac{\partial H_x}{\partial z} - \frac{\partial H_z}{\partial x} \right] \quad (3.4)$$

$$\frac{\partial E_z}{\partial t} = \varepsilon^{-1} \cdot \left[\frac{\partial H_y}{\partial x} - \frac{\partial H_x}{\partial y} \right] \quad (3.5)$$

$$\frac{\partial H_x}{\partial t} = -\mu_0^{-1} \cdot \left[\frac{\partial E_z}{\partial y} - \frac{\partial E_y}{\partial z} \right] \quad (3.6)$$

$$\frac{\partial H_y}{\partial t} = -\mu_0^{-1} \cdot \left[\frac{\partial E_x}{\partial z} - \frac{\partial E_z}{\partial x} \right] \quad (3.7)$$

$$\frac{\partial H_z}{\partial t} = -\mu_0^{-1} \cdot \left[\frac{\partial E_y}{\partial x} - \frac{\partial E_x}{\partial y} \right] \quad (3.8)$$

For a two dimensional medium invariant in the z direction, these equations simplify to:

$$\frac{\partial E_x}{\partial t} = \varepsilon^{-1} \cdot \left[\frac{\partial H_z}{\partial y} \right] \quad (3.9)$$

$$\frac{\partial E_y}{\partial t} = \varepsilon^{-1} \cdot \left[-\frac{\partial H_z}{\partial x} \right] \quad (3.10)$$

$$\frac{\partial E_z}{\partial t} = \varepsilon^{-1} \cdot \left[\frac{\partial H_y}{\partial x} - \frac{\partial H_x}{\partial y} \right] \quad (3.11)$$

$$\frac{\partial H_x}{\partial t} = -\mu_0^{-1} \cdot \left[\frac{\partial E_z}{\partial y} \right] \quad (3.15)$$

$$\frac{\partial H_y}{\partial t} = -\mu_0^{-1} \cdot \left[-\frac{\partial E_z}{\partial x} \right] \quad (3.15)$$

$$\frac{\partial H_z}{\partial t} = -\mu_0^{-1} \cdot \left[\frac{\partial E_y}{\partial x} - \frac{\partial E_x}{\partial y} \right] \quad (3.15)$$

These equations describe fields propagating in the xy plane. From this general two-dimensional field distribution, we can select one of the two propagating modes. Here we select the transverse magnetic (TM) mode, in which the electric field oscillates perpendicular to the plane and the magnetic field in the plane. For this mode $E_x=E_y=H_z=0$, which reduces the number of differential equations to three:

$$\frac{\partial E_z}{\partial t} = \epsilon^{-1} \cdot \left[\frac{\partial H_y}{\partial x} - \frac{\partial H_x}{\partial y} \right] \quad (3.15)$$

$$\frac{\partial H_x}{\partial t} = -\mu_0^{-1} \cdot \left[\frac{\partial E_z}{\partial y} \right] \quad (3.16)$$

$$\frac{\partial H_y}{\partial t} = -\mu_0^{-1} \cdot \left[-\frac{\partial E_z}{\partial x} \right] \quad (3.17)$$

Now if fields in the two dimensional TM case are also invariant in y , the field equations can be further reduced to the following simple one dimensional case:

$$\frac{\partial E_z}{\partial t} = \epsilon^{-1} \cdot \left[\frac{\partial H_y}{\partial x} \right] \quad (3.18)$$

$$\frac{\partial H_y}{\partial t} = -\mu_0^{-1} \cdot \left[-\frac{\partial E_z}{\partial x} \right] \quad (3.19)$$

These last two equations describe a TM plane wave propagating through a homogeneous isotropic medium, along the x direction.

In order to evaluate these equations numerically, the fields are specified at discrete points on the one-dimensional space and the derivatives are replaced by discrete finite difference formulae. The implementation of these two steps is crucial to understanding the FDTD method. The electric and magnetic fields are specified at alternating discrete points in space (here, along the x -axis). This spatial interleaving of E_z and H_y is shown graphically in Figure 3.6. In addition, E_z and H_y are specified at alternating discrete points in time (Figure 3.7). In essence, this one-dimensional space is actually two dimensional, in space and time. With the grid defined in such a manner, all derivatives in the field equations can be approximated with central finite difference formulae. Initially, we employed standard central

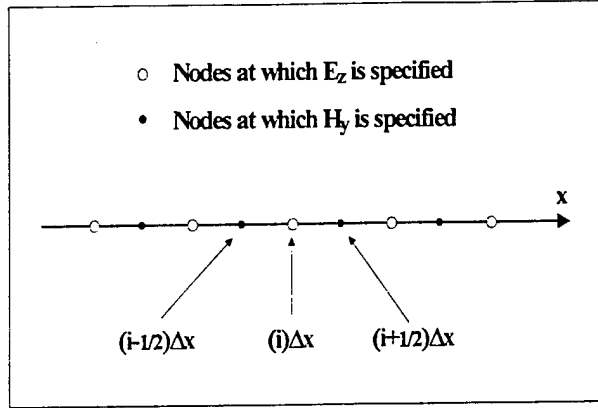


FIGURE 3.6 One-dimensional FDTD grid for TM mode.

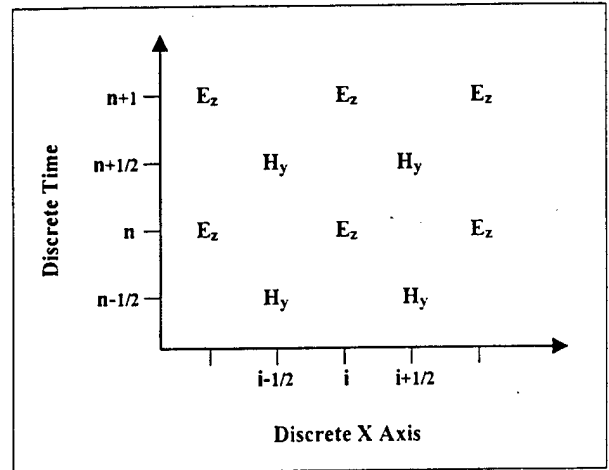


FIGURE 3.7 Staggered one-dimensional FDTD space-time grid.

finite differences with second order accuracy for all space and time derivatives. For our one-dimensional TM wave, using Eqns. (3.18) and (3.19) and drawing from Figure 3.7, the field equations become:

$$\frac{E_{z,i}^n - E_{z,i}^{n-1}}{\Delta t} = \epsilon^{-1} \cdot \left[\frac{H_{y,i+1/2}^{n-1/2} - H_{y,i-1/2}^{n-1/2}}{\Delta x} \right] \quad (3.20)$$

$$\frac{H_{y,i+1/2}^{n+1/2} - H_{y,i+1/2}^{n-1/2}}{\Delta t} = -\mu_0^{-1} \cdot \left[-\frac{E_{z,i+1}^n - E_{z,i}^n}{\Delta x} \right] \quad (3.21)$$

Here, the subscript i denotes discrete location along the x -axis, superscript n denotes discrete time step, Δt is the time between successive evaluations the electric field nodes (or successive evaluations of the magnetic field nodes), and Δx is the spatial separation between adjacent nodes of one of the fields. If the spatial distribution of fields is known before any specific time step n , the only unknown in Eqn. (3.20) above is E_z at time step n . This equation can then be reformulated to isolate that unknown quantity:

$$E_{z,i}^n = E_{z,i}^{n-1} + \frac{\epsilon^{-1} \cdot \Delta t}{\Delta x} \cdot \left[H_{y,i+1/2}^{n-1/2} - H_{y,i-1/2}^{n-1/2} \right] \quad (3.22)$$

This "update equation" can be applied to calculate the new value of E_z from field quantities obtained at earlier times. At a given time step n , this formula is applied at all of the grid's spatial locations at which E_z was specified. Once this updating is completed, E_z and H_y are known at all grid points at times up to and including step n .

From Eqn. (3.21), we obtain a similar update equation for H_y at time step $n+1/2$ in terms of E_z and H_y fields at times through step n :

$$H_{y,i+1/2}^{n+1/2} = H_{y,i+1/2}^{n-1/2} - \frac{\mu_0^{-1} \cdot \Delta t}{\Delta x} \cdot \left[-E_{z,i+1}^n + E_{z,i}^n \right] \quad (3.23)$$

At a given time step $n+1/2$, this formula is applied at all of the grid's spatial locations at which H_y was specified. Once this updating is completed, E_z and H_y are known at all grid points at times up to and including step $n+1/2$.

This technique for solving hyperbolic differential equations is known as a *staggered-leapfrog* scheme. Starting at time step zero, all of the field quantities are given initial values. This may or may not include specification of the initial values of a time-varying source at the appropriate grid nodes. At time step one-half, Eqn. (3.22) is applied at all of the E_z nodes. Afterward, if there is a time varying source located at any of the E_z nodes, those values are updated. Then, at time step one, Eqn. (3.23) is applied at all of the H_y nodes. Afterward, if there is a time varying source located at any of the H_y nodes, those values are updated.

In the case where there is a steadily oscillating time varying source, such as an incident plane wave, this process is repeated until steady state field oscillations are obtained at all points on the grid. That steady state is a numerical approximation to the solution of Maxwell's equations for the defined structure and source.

For a two dimensional spatial domain in the xy plane ($z=0$), the description above is simply extended to include spatial derivatives with respect to y , producing another update equation for H_x . For arbitrarily polarized electromagnetic fields, the field equations for the transverse electric (TE) mode are included, yielding additional update equations for E_x , E_y , and H_z . Then the two dimensional update equation for E_z is derived from the discretization of Eqn. (3.5) (instead of Eqn. (3.18), as was done in the one-dimensional case above):

$$E_{z,i,j}^n = E_{z,i,j}^{n-1} + \frac{\epsilon^{-1} \cdot \Delta t}{\Delta h} \cdot \left[H_{y,i+\frac{1}{2},j}^{n-\frac{1}{2}} - H_{y,i-\frac{1}{2},j}^{n-\frac{1}{2}} - H_{x,i,j+\frac{1}{2}}^{n-\frac{1}{2}} + H_{x,i,j-\frac{1}{2}}^{n-\frac{1}{2}} \right] \quad (3.24)$$

The subscript j has been added to denote discrete location in the y direction. In the above equation, a uniform grid is assumed, for which $\Delta x = \Delta y = \Delta h$. For this general two-dimensional isotropic medium, there are six such update equations; each obtained similarly from Eqns. (3.9) through (3.14).

3.6.3 Optical Simulation – Anisotropic Media. In addition to the isotropic medium discussed above, the FDTD method has been employed for analysis of anisotropic media³⁹. If the structure to be analyzed includes regions of inhomogeneous anisotropic material, the appropriate Maxwell's equations are:

$$\frac{\partial \mathbf{E}(\mathbf{r})}{\partial t} = \epsilon(\mathbf{r})^{-1} \cdot [\nabla \times \mathbf{H}(\mathbf{r})] \quad (3.25)$$

$$-\frac{\partial \mathbf{H}(\mathbf{r})}{\partial t} = \mu_0^{-1} \cdot [\nabla \times \mathbf{E}(\mathbf{r})] \quad (3.26)$$

where $\epsilon^{-1}(\mathbf{r})$ is the inverse of the spatially varying dielectric tensor. As before, space and time derivatives are approximated with central finite difference formulae. The structure to be analyzed is discretized spatially and material properties are defined at the appropriate locations on the computational grid. The previous FDTD simulation of liquid crystals employed this technique³⁷.

After discretization in time employing the central finite difference, Eqns. (3.25) and (3.26) can be used as follows to update the three vector components of both fields:

$$E_{I,i,j}^n = E_{I,i,j}^{n-1} + \Delta t \cdot \epsilon_{IJ,i,j}^{-1} \cdot \epsilon_{JKL} \cdot D_{K,i,j} \{H_L^{n-1/2}\} \quad (3.27)$$

$$H_{I,i,j}^{n+1/2} = H_{I,i,j}^{n-1/2} - \frac{\Delta t}{\mu_0} \cdot D_{J,i,j} \{E_K^n\} \quad (3.28)$$

where subscripts I,J,K,L can be any of the rectilinear coordinate directions x,y,z . Summation convention is used. The symbol ϵ_{IJK} represents the Levi-Civita permutation symbol. The IJ component of the inverted dielectric tensor at any grid location (i,j) is denoted $\epsilon_{IJ,i,j}^{-1}$. The superscript n denotes the discrete time coordinate, and Δt is the time step resulting from finite difference approximation of the time derivative. $D\{\}$ denotes central finite difference approximations to the spatial derivatives, with respect to the rectilinear coordinate uppercase subscript, evaluated at the discrete grid location indicated by the lowercase subscripts.

3.6.4 Mapping Liquid Crystal Director onto FDTD Grid. For an inhomogeneous liquid crystal structure, the inverted tensor in Eqn. (3.27) is determined from the liquid crystal director orientation. Liquid crystalline materials generally possess uniaxial optical anisotropy, so the relation between the tensor elements and the director's vector components is:

$$\epsilon_{I,J} = \epsilon_{\perp} \cdot \delta_{I,J} - \Delta\epsilon \cdot n_I \cdot n_J \quad (3.29)$$

Here I and J can be any of the three rectilinear directions (x,y,z) , and n_I is the component of the vector director orientation \mathbf{n} in the I direction. The bulk dielectric anisotropy of the liquid crystal is $\Delta\epsilon$, ϵ_{\perp} is the material's relative dielectric permittivity in the direction perpendicular to the vector \mathbf{n} , and $\delta_{I,J}$ is the Kronecker delta. The director orientation at a given location is thus used to calculate the dielectric tensor of the medium at that point, which is then inverted and used in Eqn. (3.27).

The available two-dimensional liquid crystal director modeling software produces data files specifying the director at discrete locations on a two-dimensional grid. If the spacing of that director data matched the spacing of the FDTD grid, each director-location specification could be assigned directly onto the FDTD grid. However, such fortuitous coincidence cannot be assumed. In fact, it is common practice to generate director data at nodes spaced approximately $0.25\mu\text{m}$ or more apart. FDTD grids are more refined, with node spacing generally one order of magnitude smaller. Because of this mismatch, liquid crystal director data must be interpolated onto the FDTD grid.

We accomplished this by means of a simple two-dimensional linear interpolation. Given the discrete director map of a liquid crystal structure and its size, each location at which the director is specified is given an absolute continuous-space location, as it would appear in the FDTD space. Then, for each FDTD grid point within that region, the four nearest neighboring points at which the director is defined are determined. See, for example, Figure

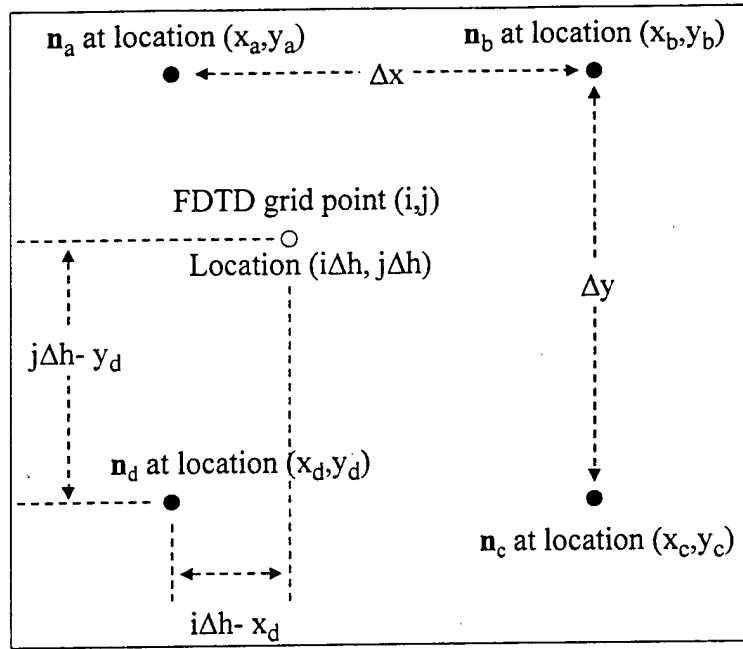


FIGURE 3.8 Interpolation of externally generated director orientation map onto FDTD grid.

3.8. The director orientation at the FDTD grid point is then approximated by a linear interpolation of the defined director orientations at those four neighboring points. The interpolation is as follows:

$$n_{i,j,l} = \frac{(\Delta x - \Delta x_d)(\Delta y_d)n_{a,l} + (\Delta x_d)(\Delta y_d)n_{b,l} + (\Delta x - \Delta x_d)(\Delta y - \Delta y_d)n_{d,l} + (\Delta x_d)(\Delta y - \Delta y_d)n_{c,l}}{\Delta x \Delta y} \quad (3.30)$$

On the left side of the above equation is the $I=(x,y,z)$ component of the director at FDTD grid point (i,j) . On the right side, the same component of the defined director orientations at points a, b, c , and d are used. The quantities Δx_d and Δy_d are defined as distances from the FDTD grid point to the “lower-left” nearest neighbor:

$$\Delta x_d = i\Delta h - x_d \quad (3.31)$$

$$\Delta y_d = j\Delta h - y_d \quad (3.32)$$

In the above equations, Δh is the uniform spacing between nodes on the FDTD grid. Once this process has been completed, the components of the dielectric tensor at that FDTD grid point are determined using Eqn. (3.29), and the tensor is inverted for use in Eqn. (3.27). This process is repeated for each FDTD grid point inside the liquid crystal structure. Once done, the liquid crystal structure has been mapped as an inhomogeneous anisotropic dielectric structure on the FDTD grid.

3.6.5 Optical Simulation – Light Source. The objective in this analysis is to calculate the response of the dielectric structure to some external light source. Hence, in addition to the dielectric structure (e.g. liquid crystal device or portion thereof) placed on the computational grid, a source of illumination must also be created elsewhere

on the grid. At time zero, the source has not yet been "turned on", and the fields at all grid points can be appropriately initialized to zero. After time zero, the source is "turned on" and, if time varying, is updated at each time step along with the remainder of the grid. The source propagates toward the dielectric object, which then superimposes its scattering response onto the incident light.

The simulated source should be designed to mimic the physical properties of the real source. If, in the simulation, the scattering object is to be illuminated by a plane wave, that simulated plane wave must propagate as a perfect non-diffracting plane wave in the absence of the scatterer. In other words, it must act as if of infinite extent. If the simulated source is to be a TEM₀₀ laser beam, it must, in the absence of a scattering object, propagate as demanded by gaussian beam theory. In other words, a gaussian profile beam must retain its gaussian profile and diverge as predicted by theory.

Quite frequently, optical simulations are conducted with plane wave sources. This provides reasonable accuracy if the extent of the source being represented is much larger than the scattering object, and if the incident wave fronts exhibit negligible curvature in the neighborhood of the scatterer. One such case is the analysis of an individual pixel in a liquid crystal display illuminated by a backlight (which is roughly the size of the entire display).

Prior analysis of beam steering liquid crystal phase gratings made use of an incident plane wave, cut off abruptly at the edges of the grating³¹. Fraunhofer diffraction of the periodic gratings was calculated assuming an incident plane wave. Each repeat unit (i.e. each blaze) was illuminated by light of the same intensity and phase. The transmission function of one such blaze was obtained and Fourier transformed, then convolved with the Fourier transform of a periodic delta function representing the locations of all such blazes in the grating. The finite nature of the grating was obtained by convolution with a rectangular window function in the spatial domain. However, the sharp finite boundaries of such a window may introduce diffraction into the analysis and does not accurately simulate illumination of a grating by a smaller diameter beam. In addition, this treatment does not accurately simulate the propagating laser beam.

For those reasons, we chose a gaussian profile laser beam as the incident light source for analysis of liquid crystal phase gratings.

Nevertheless, a simulated plane wave source did prove to be a useful tool in the development of this software. Both types of simulated sources on an FDTD grid are described below.

3.6.5.1 Plane Wave Illumination of Objects on the FDTD Grid. Plane wave illumination of liquid crystal structures is provided by means of the separate-field formulation³⁸. In this technique, the inner computational domain is divided into two regions (see Figure 3.9). In the inner region the total field, the superposition of the source and the scattered fields is calculated. In the outer region, only the scattered field is calculated. An oscillating wave source is introduced at the interface between these two regions, added into Maxwell's equations on the inner side of the interface and subtracted on the outer side. This technique can produce diffraction-free plane waves in simulations for which periodic boundary conditions are not appropriate. The separate-field formulation also permits easy extension to off-axis incident light.

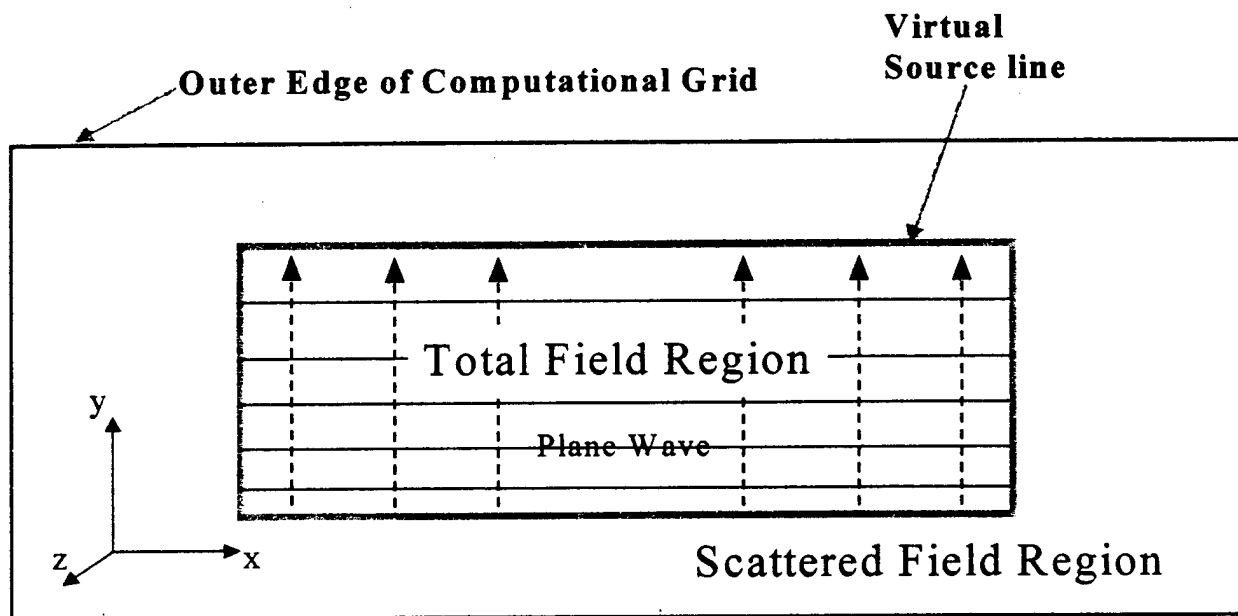


FIGURE 3.9 Layout of two-dimensional FDTD computational space with separate field formulation of plane wave.

Inside the total field region, the electric and magnetic fields at a given point in space and time are the sum of the incident (source) and scattered fields at that point. The electric field can be expressed:

$$\mathbf{E}_{i,j}^n = \mathbf{E}_{i,j}^{total,n} = \mathbf{E}_{i,j}^{incident,n} + \mathbf{E}_{i,j}^{scattered,n} \quad (3.33)$$

Outside the total field region, the electric and magnetic fields at a given point in space and time are solely due to scattered fields reaching that point. Then the electric field can be expressed:

$$\mathbf{E}_{i,j}^n = \mathbf{E}_{i,j}^{scattered,n} \quad (3.34)$$

When updating the electric field, an update formula such as Eqn. (3.24) is employed. Outside the virtual source line (Figure 3.8), the scattered electric field is updated and must be calculated from scattered magnetic field quantities. Inside the source line, updating is to be calculated from total field quantities. However, at nodes just outside and just inside the virtual source line, the updating of electric field such as occurs in Eqn. (3.24) involves a mixture of total and scattered magnetic field quantities. This requires a correction.

The difference between the total and scattered field at a particular point in space and time is simply the magnitude of the source at that place and time. So the correction involves adding or subtracting that source quantity which improperly appeared or did not appear in the field quantities used by the update equation. This correction takes place after applying the update formulae over the entire grid irrespective of whether all of the inputs were correct. The correction process can be illustrated by looking at how an inappropriate application of Eqn. (3.24), for updating E_z , is subsequently adjusted. The example here is for the case of a grid node just to the left of the virtual source line, depicted in Figure 3.10.

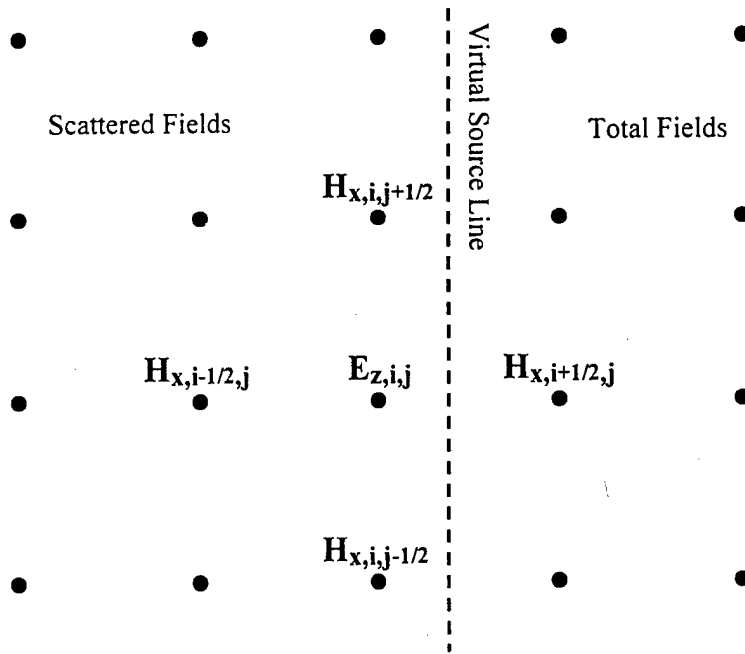


FIGURE 3.10 Updating and Correcting the z component of the electric field at (i,j) just to the left of the virtual source line. Updating of this scattered field quantity involved one total magnetic field quantity at $(i+1/2,j)$. Source at that node must be removed from the updated electric field to provide the correct scattered electric field at (i,j) .

Assume a current time step n . The electric field node (i,j) is updated using Eqn. (3.24), restated below indicating which of the field quantities involved in the equation are total or scattered fields:

$$E_{z,i,j}^{Updated,S,n} = E_{z,i,j}^{Corrected,S,n-1} + \frac{\epsilon^{-1} \cdot \Delta t}{\Delta x} \cdot \left[H_{y,i+1/2,j}^{T,n-1/2} - H_{y,i-1/2,j}^{S,n-1/2} - H_{x,i,j+1/2}^{S,n-1/2} + H_{x,i,j-1/2}^{S,n-1/2} \right] \quad (3.35)$$

Here, the added superscript S indicated a scattered field quantity and T denotes a total field quantity. Note that the "old" value of E_z was a previously corrected value; the "new" incorrectly updated result is also indicated. Analogous to Eqn. (3.33), the total magnetic field at node $(i+1/2,j)$ is the sum of incident and scattered fields there:

$$H_{y,i+1/2,j}^{T,n-1/2} = H_{y,i+1/2,j}^{S,n-1/2} + H_{y,i+1/2,j}^{I,n-1/2} \quad (3.36)$$

where the superscript I denotes the incident field at that point in space and time. So after incorrectly updating E_z at the node (i,j) , the post-updated correction becomes:

$$E_{z,i,j}^{Corrected,S,n} = E_{z,i,j}^{Updated,S,n} - \frac{\epsilon^{-1} \cdot \Delta t}{\Delta x} \cdot \left[H_{y,i+1/2,j}^{I,n-1/2} \right] \quad (3.37)$$

If the type of source and the time it was "turned on" is known, the incident magnetic field can be calculated at node $(i+1/2,j)$ for time step $(n-1/2)$. That value is used to correct the updated electric field at node (i,j) and time step n as shown in the above equation.

If the source is a plane wave traveling in a vacuum, the real part of the electric and magnetic fields take the form:

$$\mathbf{E}'(\mathbf{r}, t) = \cos(\mathbf{k} \cdot \mathbf{r} - \omega t) \quad (3.38)$$

$$\mathbf{H}'(\mathbf{r}, t) = Z_0^{-1} \cdot \mathbf{E}'(\mathbf{r}, t) \quad (3.39)$$

where k is the wave vector and Z_0 the impedance of free space. On this discrete grid, the vector \mathbf{r} is the distance from the origin of the propagating waves to grid location at which the value of the incident field is required. The time t is simply the elapsed time since the source was "turned on".

In our FDTD implementation, the source is a two dimensional cross-section of a plane wave traveling in the positive y direction of the total field region as shown in Figure 3.9. If the source is a TM field, it takes the form:

$$E_{z,i,j}^{l,n-1} = \cos\left(\frac{2\pi\sqrt{\epsilon}}{\lambda_0} \cdot [j - j_{origin}] \Delta h - \omega \cdot (n-1) \Delta t\right) \quad (3.40)$$

$$H_{x,i,j}^{l,n-1/2} = Z_0^{-1} \cdot \cos\left(\frac{2\pi\sqrt{\epsilon}}{\lambda_0} \cdot [j - j_{origin}] \Delta h - \omega \cdot \left(n - \frac{1}{2}\right) \Delta t\right) \quad (3.41)$$

Where j_{origin} is the discrete y coordinate of the bottom virtual source box in Figure 3.9, λ_0 is the wavelength in a vacuum, and all other quantities are as previously defined.

After carrying out corrections at all nodes just inside and outside the virtual source line, all of the field magnitudes on the grid are as they should be for that point in time. It should be noted that if no scattering object exists inside the total field region, there should be no scattering of the incident field into the scattered field region of the grid. This fact can be utilized as a test for proper implementation.

This source implementation results in a simulated source of finite size. Diffraction is not a concern, though, because the technique "fools" the grid into thinking it is an extract from a source of infinite extent.

3.6.5.2 Note on Periodic Boundary Conditions. Without this separate-field formalism, diffraction-free plane waves can still be produced if periodic boundaries are employed.

For this grid with two spatial dimensions, one can imagine setting up a single line source instead of the enclosed "box" shown in Figure 3.9. However, the line source would have a finite size and waves propagating from it would thus diffract as they propagated through the grid. This can be remedied through the use of periodic boundary conditions. One previous FDTD simulation of liquid crystals³⁷ employed periodic boundaries, in effect assuming an infinite lateral juxtaposition of identical liquid crystal structures, all illuminated identically. As was discussed earlier, this may not always be desirable, and may not allow accurate determination of transmitted fields if the liquid crystal structure is asymmetric. In addition, off-axis illumination with periodic boundaries is not easy to realize.

3.6.5.3 Gaussian Beam Illumination of Objects on the FDTD Grid. Illumination of objects on an FDTD grid by a simulated laser beam is not common practice. We are currently working on an implementation of such a source, drawing from the simple optics of a gaussian (TEM₀₀) beam⁴⁰. In three dimensions, the electric field in a time-varying gaussian beam propagating in the y direction takes the form:

$$\mathbf{E}(x, y, z, t) = \mathbf{E}(t) \cdot \exp \left\{ -\frac{(x^2 + z^2)}{[w(y)]^2} \right\} \quad (3.42)$$

where $w(y)$ is the e^{-2} radius of the beam's intensity, which is expanding with distance from the minimum beam waist. We can arbitrarily position the minimum beam waist at $y=0$, where the beam radius is denoted w_0 . At that location, the transverse nature of wave propagation dictates that $\mathbf{E}(t)$ has only x and z components, the combination of which defines the state of polarization of the beam. Since the liquid crystal light propagation computations are planar, the radially symmetric beam is assigned cylindrical symmetry. Then the electric field profile, invariant in z , at the beam waist is:

$$\mathbf{E}(x, 0, t) = \mathbf{E}(t) \cdot \exp \left\{ -\frac{x^2}{w_0^2} \right\} \quad (3.43)$$

Assuming this beam waist is located in a vacuum, then the time-varying magnetic field intensity is:

$$\mathbf{H}(x, 0, t) = \frac{1}{Z_0} \mathbf{E}(t) \cdot \exp \left\{ -\frac{x^2}{w_0^2} \right\} \quad (3.44)$$

where Z_0 is the impedance of free space. This source is desirable for full simulations of diffractive liquid crystal beam steering gratings.

3.6.6 Grid Termination. In order to produce an accurate solution to Maxwell's equations, the results must be a solution over an infinite space. However, practical limitations of computer power and memory require the termination of the computational grid. Any such termination method must not affect the computations inside the finite computational grid. In other words, the grid termination must not result in reflection of propagating waves back into the grid.

There are a variety of grid termination techniques³⁸, but only two are mentioned here. The initial FDTD liquid crystal study³⁷ employed the second-order Mur treatment⁴¹ for terminating the grid. The Mur grid termination technique applies a numerical solution to the wave equation along the grid boundary. It is computationally inexpensive and relatively easy to implement.

Our testing of the Mur absorbing boundary revealed that it did not result in efficient termination except for waves normally incident (or nearly so) upon the grid boundary. Reflections of waves incident upon the Mur boundary were, over many time steps, of sufficient magnitude to influence FDTD results. For this reason, the more effective "Perfectly matched layer" (PML) absorbing layer⁴² was used for the simulations in this study.

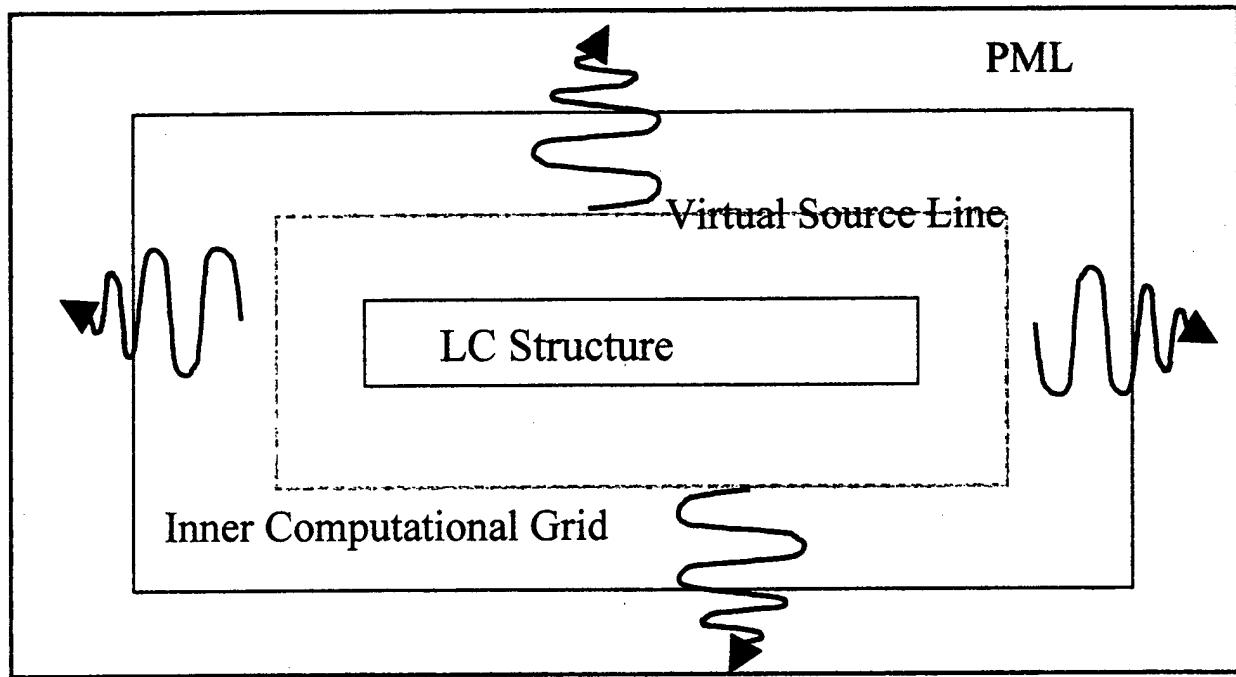


FIGURE 3.11 PML absorbing boundary layer surrounding the inner FDTD grid. All waves traveling outward from inner grid pass through the interface with the PML. Inside the PPML, all propagating waves are absorbed.

The PML is implemented as an absorbing layer which surrounds the inner computational domain (see Figure 3.11). It consists of a fictitious lossy medium incorporating magnetic as well as electric conductivity:

$$\epsilon_0 \frac{\partial \mathbf{E}}{\partial t} + \sigma \mathbf{E} = \nabla \times \mathbf{H} \quad (3.45)$$

$$-\mu_0 \frac{\partial \mathbf{H}}{\partial t} - \sigma^* \mathbf{H} = \nabla \times \mathbf{E} \quad (3.46)$$

Impedance matching of the PML with the adjacent inner computational domain makes that interface very transmissive to waves radiating from the inner grid. For instance, if the inner computational grid adjacent to the PML in Figure 3.11 is a vacuum, impedance matching of the two media requires:

$$\frac{\sigma}{\epsilon_0} = \frac{\sigma^*}{\mu_0} \quad (3.47)$$

As a result, radiation reaching the boundary passes into the PML without reflection. The electric and magnetic conductivities of the PML then result in rapid decay of waves passing into it.

As with the other regions of the grid, implementation of the PML takes the form of a set of update equations which calculate new values of a field quantity at a given point on the grid in terms of nearby field quantities obtained after prior time steps. The following description is drawn from the original paper by Berenger⁴².

In a rectilinear coordinate system, one will normally obtain three partial differential equations from each of Eqns. (3.42) and (3.43). These six equations would represent the x,y,z components of the PML Maxwell equations. However, in order to implement a reflectionless (i.e. impedance matched) interface with the inner computational grid, the out-of-plane field components of this two-dimensional space are split into two components. The resulting eight differential equations can then be written:

$$\epsilon_0 \frac{\partial E_x}{\partial t} + \sigma_y E_x = \frac{\partial(H_{zx} + H_{zy})}{\partial y} \quad (3.48)$$

$$\epsilon_0 \frac{\partial E_y}{\partial t} + \sigma_x E_y = -\frac{\partial(H_{zx} + H_{zy})}{\partial x} \quad (3.49)$$

$$\epsilon_0 \frac{\partial E_{zx}}{\partial t} + \sigma_x E_{zx} = \frac{\partial H_y}{\partial x} \quad (3.50)$$

$$\epsilon_0 \frac{\partial E_{zy}}{\partial t} + \sigma_y E_{zy} = -\frac{\partial H_x}{\partial y} \quad (3.51)$$

$$\mu_0 \frac{\partial H_x}{\partial t} + \sigma_y^* H_x = -\frac{\partial(E_{zx} + E_{zy})}{\partial y} \quad (3.52)$$

$$\mu_0 \frac{\partial H_y}{\partial t} + \sigma_x^* H_y = \frac{\partial(E_{zx} + E_{zy})}{\partial x} \quad (3.53)$$

$$\mu_0 \frac{\partial H_{zx}}{\partial t} + \sigma_x^* H_{zx} = -\frac{\partial E_y}{\partial x} \quad (3.54)$$

$$\mu_0 \frac{\partial H_{zy}}{\partial t} + \sigma_y^* H_{zy} = \frac{\partial E_x}{\partial y} \quad (3.55)$$

where there are now four "components" of each field. In addition, the conductivities σ and σ^* are each ascribed directional properties, corresponding to light propagation in the indicated directions.

The above eight differential equations *could* be discretized as was shown earlier for an isotropic medium, but the fast decay of waves propagating in the PML would render such treatment numerically unstable. Instead, the differential equations are discretized by a method known as exponential time stepping³⁸. This involves analytical solution to each differential equation and *then* a discretization. The results for Eqns. (3.49) and (3.54) are:

$$E_{y,i,j}^n = \exp\left(-\frac{\sigma_x \Delta t}{\epsilon_0}\right) \cdot E_{y,i,j}^{n-1} - \frac{1 - \exp\left(-\frac{\sigma_x \Delta t}{\epsilon_0}\right)}{\sigma_x \Delta h} \cdot \left[H_{zx,i+1/2,j}^{n-1/2} - H_{zx,i-1/2,j}^{n-1/2} - H_{zy,i,j+1/2}^{n-1/2} + H_{zy,i,j-1/2}^{n-1/2} \right] \quad (3.56)$$

$$H_{zx,i,j}^{n+1/2} = \exp\left(-\frac{\sigma_x^* \Delta t}{\mu_0}\right) \cdot H_{zx,i,j}^{n-1} - \frac{1 - \exp\left(-\frac{\sigma_x^* \Delta t}{\mu_0}\right)}{\sigma_x^* \Delta h} \cdot [E_{y,i+1/2,j}^n - E_{y,i-1/2,j}^n] \quad (3.57)$$

The subscripts and superscripts are all as denoted earlier for discretized differential equations. The remaining six Eqns. (3.48), (3.50), (3.51), (3.52), (3.53), and (3.55) can be discretized by comparison.

When updating PML components involving split-fields at nodes on the inner edges of the PML, the split fields from interior nodes are not available. In such cases, one should utilize the single unsplit interior field component in place of the split field component. If an interior node adjacent to the PML interface requires a split field quantity from a PML node, one should sum the split field components from the appropriate PML node and use that sum as the unsplit field quantity in the interior update formula.

The discretized PML equations are deployed differently in the three types of regions shown in Figure 3.12. In region I, all field components (x, y, zx , and zy for both E and H) are updated using exponential discretizations of PML Eqns. (3.48) through (3.55). In region II, exponentially discretized PML equations are utilized to update all x and zy field components. In this region, σ_x and σ_x^* are both set equal to zero. Then the y field components are updated utilizing update formulae for an isotropic medium, i.e. the standard central finite differencing of Eqns. (3.4) and (3.7). The zx components are updated using standard central finite differencing of PML Eqns. (3.50) and (3.54), with σ_x and σ_x^* both set equal to zero. In region exponentially discretized III, PML equations are utilized to update all y and zx field components. In this region, σ_y and σ_y^* are both set equal to zero. Then the x field components are updated utilizing update formulae for an isotropic medium, i.e. the standard central finite differencing of Eqns. (3.3) and (3.6). The zy components are updated using standard central finite differencing of PML Eqns. (3.51) and (3.55), with σ_y and σ_y^* both set equal to zero.

The conductivity values require some careful treatment. One might want to arbitrarily set those values equal to some large value uniformly throughout the PML in order to increase damping. After all, as long as impedance

| | | |
|-----------------|---------------|------------|
| PML I | II | I |
| III | Interior Grid | III |
| I | II | I |

FIGURE 3.12 PML is implemented differently in the three regions shown.

matching is observed, all incident waves should enter the PML, and large conductivity values will damp out those waves in a very short distance. That would permit use of a very thin PML layer, reducing its computational load. However, such an implementation would result in undesired numerical reflections back into the interior grid. In order to prevent those reflections, conductivity values should be small just inside the PML and increased gradually with increasing distance into the PML layer. We set those conductivity values equal to zero at the interior-PML interface, and increased them according to:

$$\sigma(r) = \sigma_{\max} \left(\frac{r}{d} \right)^s \quad (3.58)$$

where r is the distance into and d is the thickness of the PML layer. The values of σ_{\max} and s are chosen, after testing, to minimize reflection back into the interior grid. Optimum values of each depend on the thickness of the PML. For a PML which is $6\Delta h$ thick, we found optimum values of $\sigma_{\max} = 5 \times 10^7 \Omega^{-1} \text{m}^{-1}$ (same *magnitude* for the magnetic conductivity) and $s=5$.

3.6.7 Numerical Stability and Accuracy. Two other matters are of importance in FDTD simulations. First, limiting the size of the time step is necessary to prevent growth of numerically induced oscillations. Second, inaccuracies can result from the temporal and spatial discretization of the problem.

Limiting the size of the time step is necessary in order to prevent growth of numerically induced oscillations. The limit for a two-dimensional uniformly spaced FDTD grid employing second-order accurate spatial and temporal finite differences is expressed in the following relation³⁸:

$$\Delta t \leq \frac{\Delta h}{v_{\max} \sqrt{2}} \quad (3.59)$$

where Δt is the size of the time step and v_{\max} is the maximum phase velocity of waves traveling on the grid. The spatial step Δh is the size of the standard Yee cell³⁵ (two node separations across), normally defined as λ/N . For the sake of accuracy, N is usually 10 or larger. Increasing N will produce more accurate results.

FDTD inaccuracies result from the temporal and spatial discretization of the problem. For instance, the second-order accurate central finite difference approximations used in this study are somewhat less than exact. Such discretization can manifest itself in numerical dispersion³⁸, which is the departure of numerical phase velocity from that which would occur in continuous space. In particular, the phase velocity of waves in an FDTD simulation employing second-order accurate spatial and temporal finite differences is always less than the continuous-space value. In other words, the numerical wavelength is always less than the continuous-space value, and spectral data generated by FDTD simulations will be shifted to longer wavelengths⁴³.

The magnitude of this shift depends on spacing between nodes on the grid, time step size, dielectric properties, and the frequency of the propagating wave. Because time stepping to a steady-state FDTD result may require

accounting for multiple reflections, the impact of numerical dispersion also depends on the size of the structure to be analyzed and the number of time steps required to reach steady state.

Of these factors, only the time step size and node spacing are not predetermined by a particular problem. One might expect that as time step and node spacing approach zero, errors are reduced and the FDTD result approaches the exact solution. This behavior for node spacing has been confirmed⁴³. However, as has been found in previous studies^{44,45}, FDTD results are more accurate when the time step is equal to, not less than, its maximum stable value. This may be due in part to the fact that as the time step is decreased, more steps are necessary to reach steady state, increasing the impact of roundoff error.

Thus, for a given discretization scheme, the only simple control over accuracy and dispersion is the choice of node spacing. As node spacing is reduced, numerical dispersion decreases and accuracy increases.

3.6.8 Computational Expense. Unfortunately, grid refinement can overpower the computer hardware. For example, consider a liquid crystal structure $50\mu\text{m} \times 10\mu\text{m}$, being simulated for $\lambda=500\text{nm}$, on a grid with nodal spacing of $\Delta h = \lambda/60$ (required for accurate results when employing second-order-accurate finite differencing⁴³). Discretization of the structure will produce $2.9 \cdot 10^7$ nodes, each with three vector components, each double precision. In addition, at each node there is a 3×3 dielectric tensor. The resulting computation would cover $3.5 \cdot 10^8$ double precision numbers, requiring approximately 2.8GB of RAM. Even without considering computation time, this is clearly not a practical numerical computation.

The solution to this problem is substitution of fourth-order accurate finite difference approximation for the spatial derivatives. Fourth-order accurate central finite difference approximations do not require as much grid refinement as second order finite differences in order to produce accurate results.

3.6.9 Central Finite Differencing Accurate to Fourth Order in Space. The standard central finite difference approximation of a first derivative, accurate to within an amount proportional to the square of the spacing between nodes, is often called a second order accurate finite difference. On the interior grid, second order accurate approximations have been utilized up to now in this chapter. For instance, Eqn. (3.18) and an approximation to it utilizing second order accurate approximations to both space and time derivatives were:

$$\frac{\partial E_z}{\partial t} = \epsilon^{-1} \cdot \left[\frac{\partial H_y}{\partial x} \right] \quad (3.60)$$

$$\frac{E_{z,i}^n - E_{z,i}^{n-1}}{\Delta t} = \epsilon^{-1} \cdot \left[\frac{H_{y,i+1/2}^{n-1/2} - H_{y,i-1/2}^{n-1/2}}{\Delta x} \right] \quad (3.61)$$

If the second order accurate spatial difference approximation is replaced with a standard fourth order accurate central finite difference approximation, Eqn. (3.61) becomes:

$$\frac{E_{z,i}^n - E_{z,i}^{n-1}}{\Delta t} = \varepsilon^{-1} \cdot \left[\frac{-H_{y,i+3/2}^{n-1/2} + 27 \cdot H_{y,i+1/2}^{n-1/2} - 27 \cdot H_{y,i-1/2}^{n-1/2} + H_{y,i-3/2}^{n-1/2}}{24 \cdot \Delta x} \right] \quad (3.62)$$

Eqn. (3.62) is more accurate, for a given spacing of grid nodes, than Eqn. (3.61). However, it can be improved further by slightly adjusting the finite difference coefficients as described by Taflov^{38,46}. The adjusted equation becomes:

$$\frac{E_{z,i}^n - E_{z,i}^{n-1}}{\Delta t} = \varepsilon^{-1} \cdot \left[\frac{-B \cdot H_{y,i+3/2}^{n-1/2} + A \cdot H_{y,i+1/2}^{n-1/2} - A \cdot H_{y,i-1/2}^{n-1/2} + B \cdot H_{y,i-3/2}^{n-1/2}}{\Delta x} \right] \quad (3.63)$$

We found that A=1.22634 and B=0.04234 provided greatest accuracy for most of our simulations.

3.7 Near Field Optical Simulation – Verification.

In order to confirm validity of this computational method, it was applied to several well-known liquid crystal problems with analytical solutions. The first is optical rotation in a twisted-nematic cell. The second problem is that of Bragg reflection at normal incidence from a planar cholesteric layer with helical axis normal to the surrounding substrates.

Optical rotation in twisted nematic cells is a well-known phenomenon⁴⁷. If the quantity $\Delta n \cdot d / \lambda$ is properly adjusted, an incident linearly polarized source will emerge from the other side of the TN cell still linearly polarized, with its plane of polarization rotated by 90°. The lowest such value of $\Delta n \cdot d / \lambda$ is approximately 0.866. A twisted nematic cell with those characteristics was placed in the FDTD computational grid. It was illuminated with a linearly polarized source, normally incident upon the glass-liquid crystal interface. As can be seen in Figures 3.13 and 3.14,

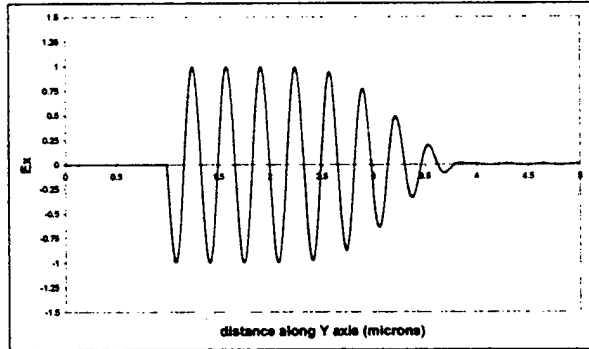


FIGURE 3.13 Lab frame x component of wave propagating along y-axis, normal to first minimum TN cell. Source linearly polarized in xy plane, emitted at $y=2\mu\text{m}$. TN layer located between $2\mu\text{m}$ and $4\mu\text{m}$. Filled with nematic liquid crystal ($n_e=1.7165$, $n_o=1.5$), embedded in glass ($n=1.5$), $\lambda = 0.5\mu\text{m}$. Rub direction of first surface is parallel to z-axis.

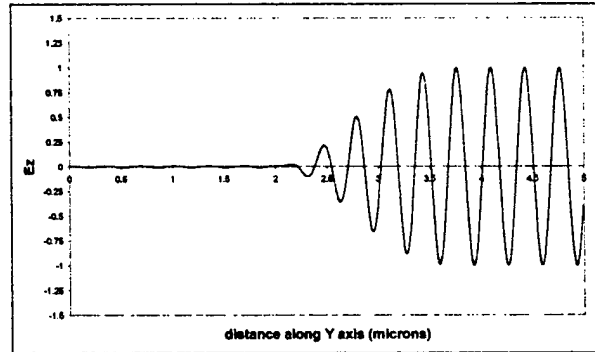


FIGURE 3.14 Lab frame z component of wave propagating along y-axis, normal to first minimum TN cell. Source linearly polarized in xy plane, emitted at $y=2\mu\text{m}$. TN layer located between $2\mu\text{m}$ and $4\mu\text{m}$. Note that incident x-polarized field has been rotated to z-polarization after traversing y-thickness of TN cell.

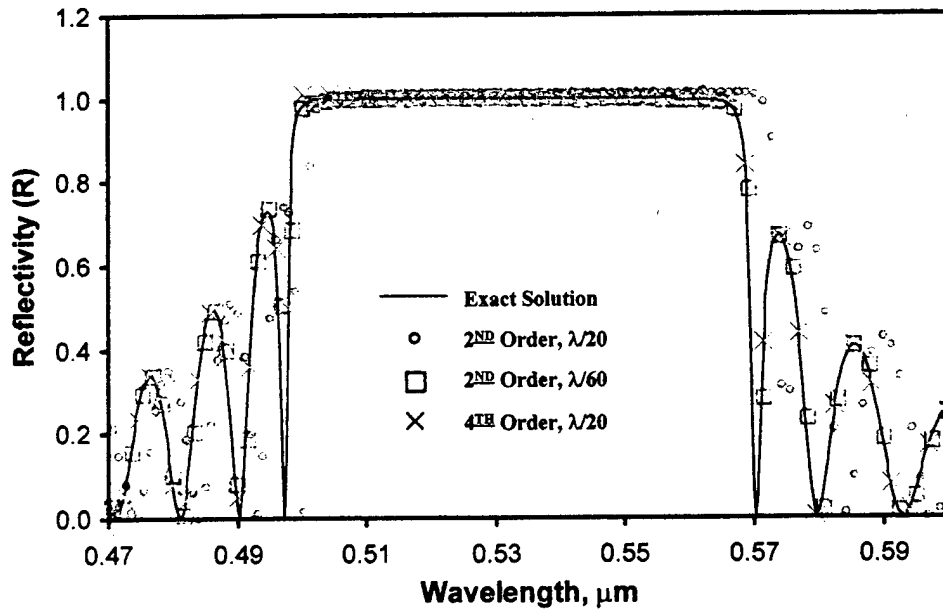


FIGURE 3.15 Bragg reflection from a planar cholesteric layer. Comparison of analytical solution to FDTD data generated with second and fourth order accurate finite differences at different FDTD grid resolutions.

the source is indeed rotated and emerges from the nematic layer still linearly polarized.

Bragg reflection from cholesteric liquid crystal cells is another well-known phenomenon²⁴. This is a more rigorous test for the FDTD method, as the liquid crystal director changes significantly over much shorter distances than the TN cell. Analytical solutions to this problem have been developed⁴⁸.

A cholesteric layer was placed in the FDTD grid. The fictitious cholesteric layer was illuminated with a circularly polarized source normally incident upon the glass-liquid crystal interface. The magnitude of the reflected field was computed at discrete wavelengths over a range encompassing the reflection band. These FDTD-generated data points were superimposed on the curve of the analytic solution. The results of this comparison appear in Figure 3.15. FDTD computation utilizing fourth order spatial difference approximations produced results for $\Delta h = \lambda/20$ as accurate as second order differencing with $\Delta h = \lambda/60$.

3.8 Far Field Computation

3.8.1 Introduction. The FDTD method described above is used to direct a light source at a liquid crystal structure and then compute the electromagnetic fields exiting that structure. Those exit fields are in the near field region, which is defined as being within one wavelength or so beyond the exit surface. The next step in the simulation is to utilize those results to obtain the distribution of light far from the liquid crystal structure. That far zone distribution of light is what we often call the diffraction pattern. In the case of a beam steering liquid crystal grating, the diffraction pattern includes the portion of incident light which is steered into the desired direction, plus that portion which propagates in other directions. Complete knowledge of this distribution of diffracted light may be of use in improving the design of these liquid crystal beam steering devices.

After employing the FDTD method to obtain the near fields, the same technique could be applied outward through space to some distance from the diffracting liquid crystal structure. Assuming careful attention is paid to numerical issues, one could thusly obtain the far field pattern. However, as has already been discussed, the FDTD method incurs substantial computational costs even for relatively small structures. Because of limits to computer memory and speed, direct computation of far field behavior is not feasible at this time. An alternate technique is required. For this we turn to diffraction theory.

3.8.2 Diffraction Theory. There are a number of different diffraction models. These models can be divided into two classes, vector and scalar. Scalar treatments include Huygens' Principle^{49,50,51}, Rayleigh-Sommerfeld theory^{49,50,51,52}, the Kirchhoff formulation^{49,50,51,52}, and a model referred to as the angular spectrum of plane waves^{51,53}. The well-known Fraunhofer and Fresnel approximations, as they appear in most introductory optics texts, are derived from the Kirchhoff model. Vector models include a treatment by Stratton and Chu⁵⁴, another based on the surface equivalence principle⁵⁵, and a rigorous electromagnetic boundary value model which appears in Jackson's text⁵⁶ (among other places). Each of these theoretical models has strengths and weaknesses, and each can be satisfactorily employed for some range of problems. The choice of an appropriate model is based on what is known about a specific problem.

Application of any diffraction model can be divided into two separate tasks⁵⁷. First, one must obtain the fields exiting a diffracting object (i.e. the near fields, or the boundary field values), or a reasonable approximation thereof. The second step involves propagating those fields to the desired observation point. These are distinct and separate parts of the diffraction models listed above. Most texts do not make this separation clear. Instead, the boundary value assumptions and subsequent propagation into the far field are lumped together into one theoretical treatment. If the resulting diffraction pattern is at all inaccurate, it is difficult to determine how much of that error is due to incorrect boundary fields and how much is the result of the propagation calculation. Because of this, it is often difficult to know which model is appropriate for a particular problem.

We are not searching for an accurate complete diffraction model. What is sought is only that portion of one of the diffraction theories which can accurately calculate far zone diffraction patterns given accurate near fields. Our purpose here is not to provide rigorous proof of accuracy. Instead, what follows is an attempt at sorting through the various theories in order to provide rationale for the choice of one such method.

It is often said that scalar diffraction models are not applicable for diffracting apertures possessing features with sizes on the order of a wavelength. In addition, some models, notably the Fraunhofer and Fresnel approximations, are of questionable value for calculating nonparaxial diffracted fields.

In general, scalar theories assume the exact boundary field distribution (i.e. the near field) is not known, and make an intelligent guess about its values. For instance, Rayleigh and Kirchhoff treatments of diffraction by a slit in an opaque screen often assume the fields inside the opening are the same as the undisturbed (i.e. incident) values, and are zero elsewhere on the screen. That assumption produces boundary fields which are discontinuous at the edges of the slit. Approximate boundary fields obtained in such a manner are not an exact representation of the true boundary fields. The approximation neglects to apply Maxwell's equations to obtain exact boundary conditions at

the edges of the aperture. As a result, subsequent calculation of the diffracted fields will contain some error. The magnitude of error increases as the width of the slit is reduced to and below the wavelength of incident light.

In any case, scalar theory calculations based on simple assumptions about boundary fields generally depart somewhat from experimental data. This is particularly true for cases when the diffracting aperture or features therein are not large compared to a wavelength^{58,59}. Approximation of the boundary field distribution is at least partly to blame.

There have been attempts to obtain more accurate representations of boundary fields for some simple problems such as an infinite slit⁶⁰, an infinite half-plane⁶¹, or a circular aperture⁵⁰. However, those boundary field computations are difficult and not generally applicable to arbitrary diffracting apertures.

Vector models are also capable of obtaining more accurate near fields. Such treatments apply electromagnetic boundary conditions, derived from Maxwell's equations, to the diffracting aperture. The accuracy of boundary fields obtained in such a manner depends on the ability to solve the boundary condition equations. Again, for complicated diffracting objects, the calculation is often extremely difficult if not impossible.

So it is imperative that one obtain the most accurate possible representation of the near fields. The FDTD method is capable of computing accurate near fields. But if one can obtain accurate boundary fields by some method such as FDTD, which propagation method should be employed? Are there restrictions which accompany any of these propagation methods?

First, we should make note of one feature of the FDTD computation method. The core algorithm employed by the FDTD method is derived directly from the differential forms of Ampere's and Faraday's laws, also known as the two Maxwell curl equations. The two divergence laws are not explicitly enforced in the FDTD method, but it has been shown to possess a divergence-free nature³⁷. Consequentially, it can be said that fields computed by the FDTD method are solutions to Maxwell's equations, to within any error incurred by the numerical nature of the computation. This is an increase in accuracy over simple near field approximations such as described above.

Given that the near fields produced by the FDTD computational method can be close approximations of Maxwell fields, all that should be required of a propagation model is that it retain the Maxwellian nature of those fields as they propagate away from the near zone. Any such propagation model should produce an accurate diffraction pattern from accurate fields on the surface of a diffracting aperture.

With the exception of the original Huygens' Principle, all of the diffraction theories listed above contain propagation models derived from Maxwell's equations. Propagation models in the scalar Rayleigh and Kirchhoff theories are based on the Helmholtz wave equation, which is obtained directly from Maxwell's curl equations. After application of Green's Theorem, the propagation models are derived. The scalar propagation models are then applied to each vector component of the boundary field. If the vector near fields adhere to Maxwell's equations, the component-by-component propagation of those fields employing a method derived from the wave equation should, in theory, produce Maxwell far fields.

It should be noted that the differences between these scalar theories result from different aspects of the boundary fields employed in their respective propagation models. As a result, incorrectly specified boundary fields can lead to

different diffraction patterns from these scalar theories. Conversely, given the same accurate boundary values, these propagation models should produce the same diffraction pattern⁵⁷.

The preceding discussion provides reasonable expectation that we can safely use the propagation models contained in Rayleigh and Kirchhoff theories. The major problem with those theories is the possibility of incorrectly specified boundary fields. Use of FDTD-computed near fields significantly reduces that concern.

We have not discussed the angular spectrum representation or any of the vector theories. Each of these methods has its proponents. We can say that there are doubts about the validity of the Stratton-Chu theory because its propagation model is not divergence-free. The Surface Equivalence Principle is popular in the electrical engineering community, but is more difficult to implement in its non-paraxial form. In theory, it should produce Maxwell far fields from Maxwell near fields. The angular spectrum of plane wave representation can be connected to the wave equation and, like the Rayleigh and Kirchhoff propagation models, is theoretically correct.

3.8.3 Derivation of Two-Dimensional Kirchhoff Surface Integral. In theory, we could have employed either Rayleigh integral. However, the Kirchhoff integral is a simple average of the two Rayleigh integrals. One of the Rayleigh integrals makes use of near field magnitudes, and the other utilizes the derivatives of near fields. It is possible that numerical errors may be more pronounced in one or the other Rayleigh integral, and that may change from one problem to another. If so, an average of the two can reduce that concern. For that reason, and for reasons of coding ease, we chose to implement the primitive form of the Kirchhoff propagation integral.

The problem at hand is shown in Figure 3.16. The aperture shown in the drawing represents a cross-sectional slice of a liquid crystal layer such as one used to form a beam steering grating. Since we are dealing with beam steering in one plane, the liquid crystal grating can be assumed to vary only in the direction of the grating vector. The grating vector lies in the plane of the drawing, parallel to the x -axis. The near fields produced by FDTD propagation of light through the grating are obtained at the layer surface and are defined to exist on the plane $y=0$. Because of

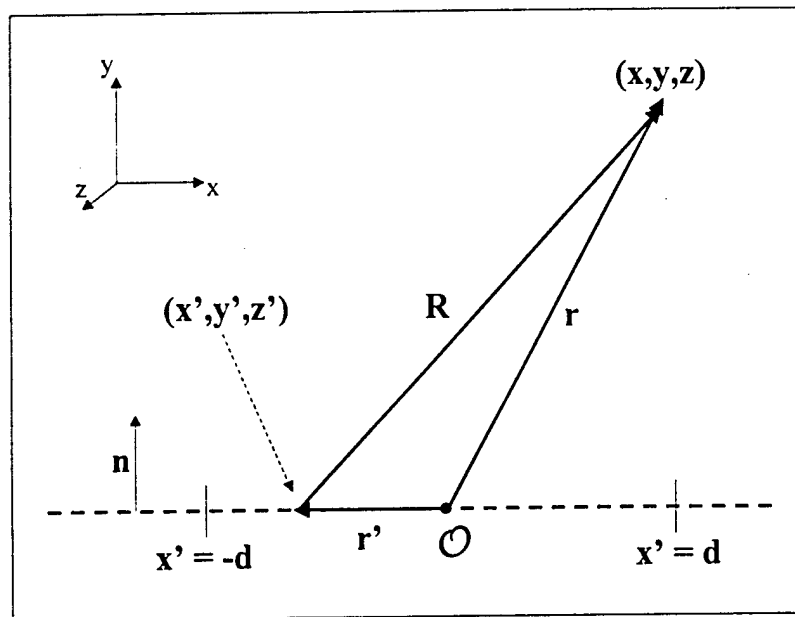


FIGURE 3.16 Geometry of diffraction problem. The diffracting object lies in the $y'=0$ plane between $x'=(-d)$ and $x'=d$. Diffracted light is observed at (x,y,z) .

the symmetry in our grating problem, those surface fields are invariant in z . The "measurable" fields emerging from the liquid crystal layer extend from $x=-d$ to $x=d$. Outside of that region, the gaussian profile of the incident beam directed at the liquid crystal grating layer dictates that transmitted fields will have negligible amplitude. The location of any point on the surface of the layer is denoted $\mathbf{r}'=(x',y',z')$, and the location of any observation point in the far zone is denoted $\mathbf{r}=(x,y,z)$. The unit vector $\mathbf{n}=\mathbf{y}$ is the normal to the grating layer surface.

This distribution of fields from $x=-d$ to $x=d$ is in essence a one-dimensional aperture. The primitive Kirchhoff integral must be recast for this problem. The primitive form of the Kirchhoff integral for a two-dimensional aperture in three-dimensional space takes the form:

$$\psi(x,y,z) = \frac{1}{4\pi} \iint_{\text{aperture}} \mathbf{n} \cdot \left[G(\mathbf{r},\mathbf{r}') \cdot \nabla_{\mathbf{r}} \psi(\mathbf{r}') - \psi(\mathbf{r}') \cdot \nabla_{\mathbf{r}} G(\mathbf{r},\mathbf{r}') \right] \cdot d\mathbf{x}' dz' \quad (3.64)$$

The Green's function $G(\mathbf{r},\mathbf{r}')$ is defined as:

$$G(\mathbf{r},\mathbf{r}') = \frac{e^{ikR}}{R} \quad (3.65)$$

The magnitude of the distance between any point on the aperture to any observation point is:

$$R = |\mathbf{r} - \mathbf{r}'| = \sqrt{(x-x')^2 + (y-y')^2 + (z-z')^2} \quad (3.66)$$

Since the surface fields of our grating problem do not vary with z' , the far field pattern will not vary with z , and then we can arbitrarily choose this problem to exist in the plane $z=0$. Since the FDTD near fields are obtained at the liquid crystal layer surface, we can also define $y'=0$. Then:

$$R = \sqrt{(x-x')^2 + (y)^2 + (z')^2} \quad (3.67)$$

The integral, over the aperture surface, is to be evaluated over the surface of the grating, for $x' \in (-d,d)$ and $z' \in (-\infty,\infty)$. Evaluating the normal component of the two gradient operations yields:

$$\psi(x,y,z) = \frac{1}{4\pi} \int_{-d}^d \partial_y \psi(\mathbf{r}') \left[\int_{-\infty}^{\infty} G(\mathbf{r},\mathbf{r}') \cdot dz' \right] \cdot dx' - \frac{1}{4\pi} \int_{-d}^d \psi(\mathbf{r}') \left[\int_{-\infty}^{\infty} \partial_y G(\mathbf{r},\mathbf{r}') \cdot dz' \right] \cdot dx' \quad (3.68)$$

We can make use of the Hankel function of the first kind to evaluate the integrals along z' :

$$\psi(x,y,z) = \frac{1}{4} \int_{-d}^d \partial_y \psi(\mathbf{r}') \cdot H_0^{(1)}(kR_{\parallel}) \cdot dx' - \frac{1}{4} \int_{-d}^d \psi(\mathbf{r}') \cdot \partial_y H_0^{(1)}(kR_{\parallel}) \cdot dx' \quad (3.69)$$

After the integration along z' , the distance R has become R_{\parallel} :

$$R_{\parallel} = \sqrt{(x-x')^2 + (y)^2} \quad (3.70)$$

Since we are only concerned with diffracted light in the far zone, we can make use of the large-argument approximation of the Hankel function and evaluate the partial derivative inside the second integral term to give:

$$\psi(x, y) = \frac{1}{4} \int_{-d}^d e^{-i\pi/4} e^{ikR_{\parallel}} \sqrt{\frac{2}{\pi k R_{\parallel}}} \partial_y \psi(x') \cdot dx' - \frac{1}{4} \int_{-d}^d \psi(x') e^{-i\pi/4} \sqrt{\frac{2}{\pi k}} \frac{iky e^{ikR_{\parallel}}}{R_{\parallel}^{3/2}} \cdot dx' \quad (3.71)$$

Note the occurrence of y in the numerator of the second integral term. If the diffraction pattern were to be evaluated only over the paraxial region, $y/R \sim 1$. The above equation may finally be simplified, assuming $kR_{\parallel} \ll 1$, to give:

$$\psi(x, y) = \frac{e^{-i\pi/4}}{\sqrt{8\pi k}} \int_{-d}^d \frac{e^{ikR_{\parallel}}}{\sqrt{R_{\parallel}}} \left\{ \partial_y \psi(x') - \frac{iky}{R_{\parallel}} \psi(x') \right\} \cdot dx' \quad (3.72)$$

This integral could to be applied to all six components of the surface fields $E(x')$ and $H(x')$. However, if the medium for $y > 0$ is linear and isotropic, there are only two independent propagating modes. Consequently, the above integral need only be evaluated for $E_z(x')$ and $H_z(x')$. That will produce two far field distributions $E_z(x, y)$ and $H_z(x, y)$. From those values the relative intensity of the diffraction pattern is calculated:

$$I(x, y) \propto E_z(x, y)^2 + Z_0^2 H_z(x, y)^2 \quad (3.73)$$

In our implementation, the (x, y) dependence was converted to an angular distribution, for which $\theta = \arctan(x/y)$. This concludes discussion of far field diffraction pattern computation.

3.9 Initial Calculations

The FDTD method has been implemented as described above. We have not yet added some software details necessary to carry out full simulations of laser illuminated liquid crystal gratings. However, we have conducted three calculations on two smaller liquid crystal structures.

Each of these liquid crystal structures is a pixel or pair of pixels from a liquid crystal display or spatial light modulator. The liquid crystal director orientation maps were computed and provided to us by Dr. Jack Kelly, also at the Liquid Crystal Institute. These mappings were imported onto the FDTD grid in the layout shown in Figure 3.17. The structures were illuminated by a linearly polarized plane wave source described earlier. A dichroic polarizing layer was placed on the transmission side of each structure tested, adjacent to it on the grid. This entire assembly was embedded in glass with a refractive index of 1.5. The near field computation was carried out until steady state oscillations were obtained on the entire grid. Transmitted electric and magnetic fields were then collected from the transmission side of the polarizer. That data provided a means of calculating the emerging transmitted intensity profile, and served as input for the far field calculation.

The first liquid crystal structure to be simulated was a twisted nematic structure, whose director map is shown in Figure 3.18. There is a grounded electrode at the top of the structure. The default twisted structure is affected by voltage applied to a smaller lower electrode. The director distribution was obtained for a voltage well in excess of

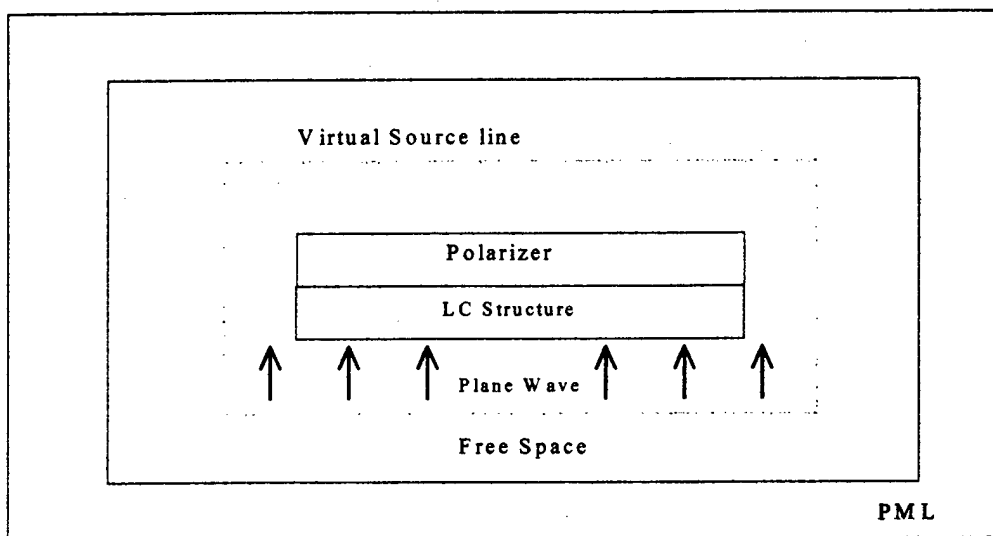


FIGURE 3.17 Layout of FDTD grid for plane wave excitation of small liquid crystal structure and dichroic polarizing layer.

the Freedericksz threshold applied to the lower electrode. One of its notable features is the reverse-tilt disclination located asymmetrically within the structure.

Because this finite structure was to be illuminated by a plane wave of infinite extent, we expected some diffractive artifacts in the transmitted fields at the edges of the structure. In order to reduce the influence of that edge diffraction on transmission by the field-reoriented portion of the liquid crystal structure, the structure on the FDTD

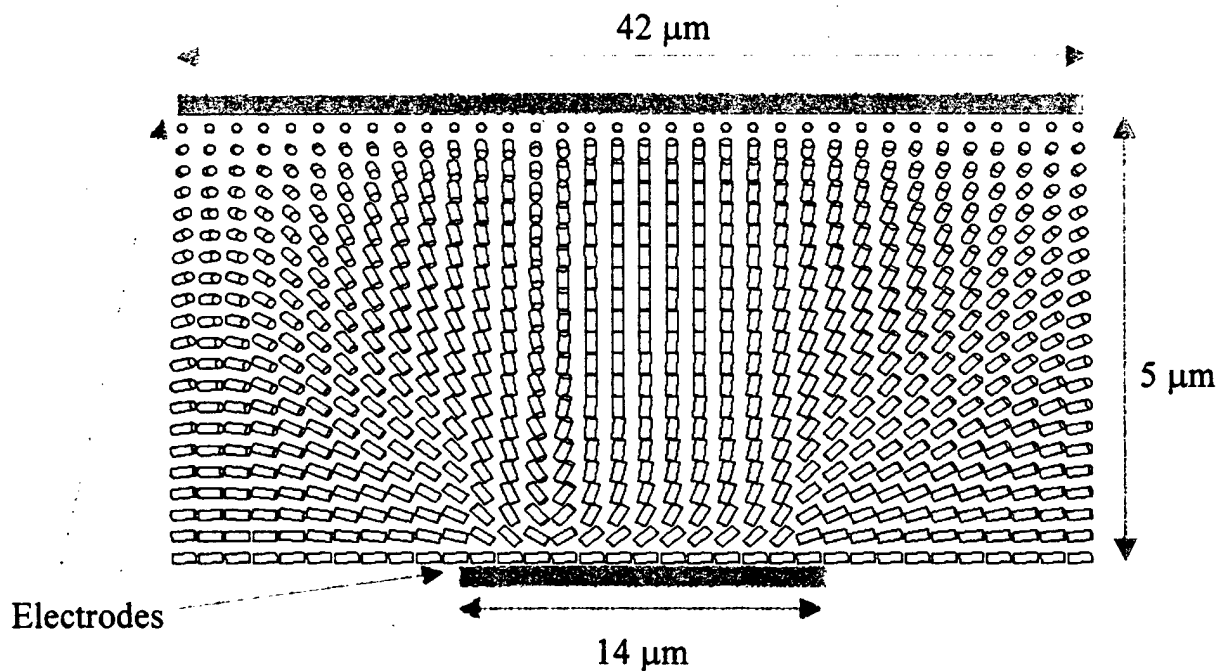


FIGURE 3.18 Twisted nematic structure with some voltage applied. Note that liquid crystal retains undisturbed twisted structure at left and right sides of structure, far from the small lower electrode to which voltage is applied. Reverse tilt disclination appears just to left of center of lower electrode and extends vertically to upper electrode.

grid was "padded". This padding consists of simple extensions of the left and right edge director orientations by $11\mu\text{m}$. The simulated structure was thus $64\mu\text{m}$ wide, not $42\mu\text{m}$ as shown in Figure 3.18.

The near field intensity patterns of this structure were obtained using our FDTD code. Two such simulations were performed. For one calculation, the structure was illuminated from below with normally incident light linearly polarized perpendicular to the liquid crystal director at the lower surface. The absorption axis of the exit-side polarizer was oriented parallel to the plane of the structure. This is "o-mode" illumination of "normally dark" operation. The resulting near field intensity pattern is shown in Figure 3.19. The sharp spike in the near field intensity curve is the product of the disclination appearing in Figure 3.18.

The far field intensity distribution is shown in Figure 3.21. This was calculated at a distance of one meter from the structure. The near field "edge diffraction" appearing in Figure 3.19 was not included in the calculation. The far field pattern appears somewhat irregular, without any well-defined diffraction orders. The lack of a well-ordered diffraction pattern is the result of lack of uniformity or periodicity in the single liquid crystal aperture.

For the second calculation of the TN structure, the normally incident light was linearly polarized parallel to the liquid crystal director at the lower surface. The absorption axis of the exit-side polarizer was oriented perpendicular to the plane of the structure. This is "e-mode" illumination of "normally dark" operation. The resulting near field

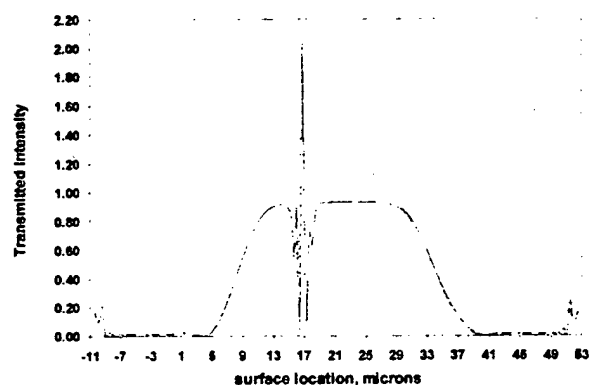


FIGURE 3.19 Surface intensity profile, partially activated twisted nematic structure, o-mode source, normally dark mode.

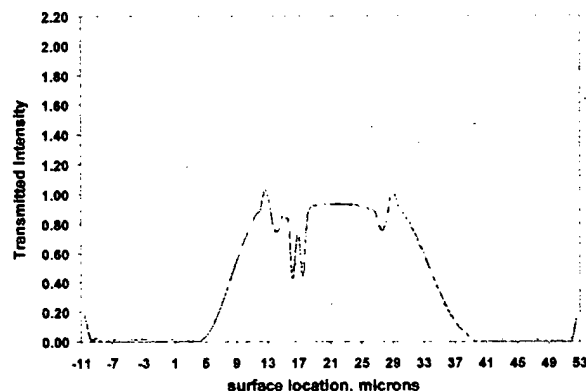


FIGURE 3.20 Surface intensity profile, partially activated twisted nematic structure, e-mode source, normally dark mode.

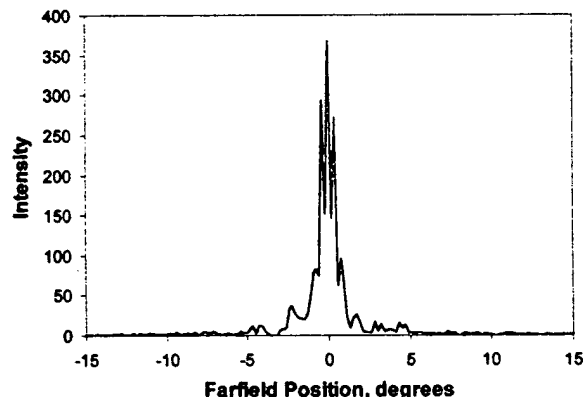


FIGURE 3.21 Surface intensity profile, partially activated twisted nematic structure, e-mode source, normally dark mode.

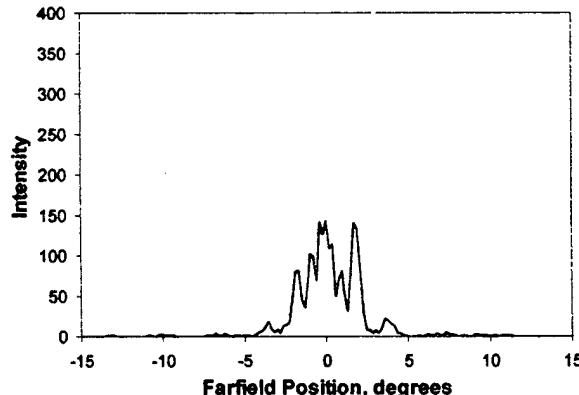


FIGURE 3.22 Surface intensity profile, partially activated twisted nematic structure, e-mode source, normally dark mode.

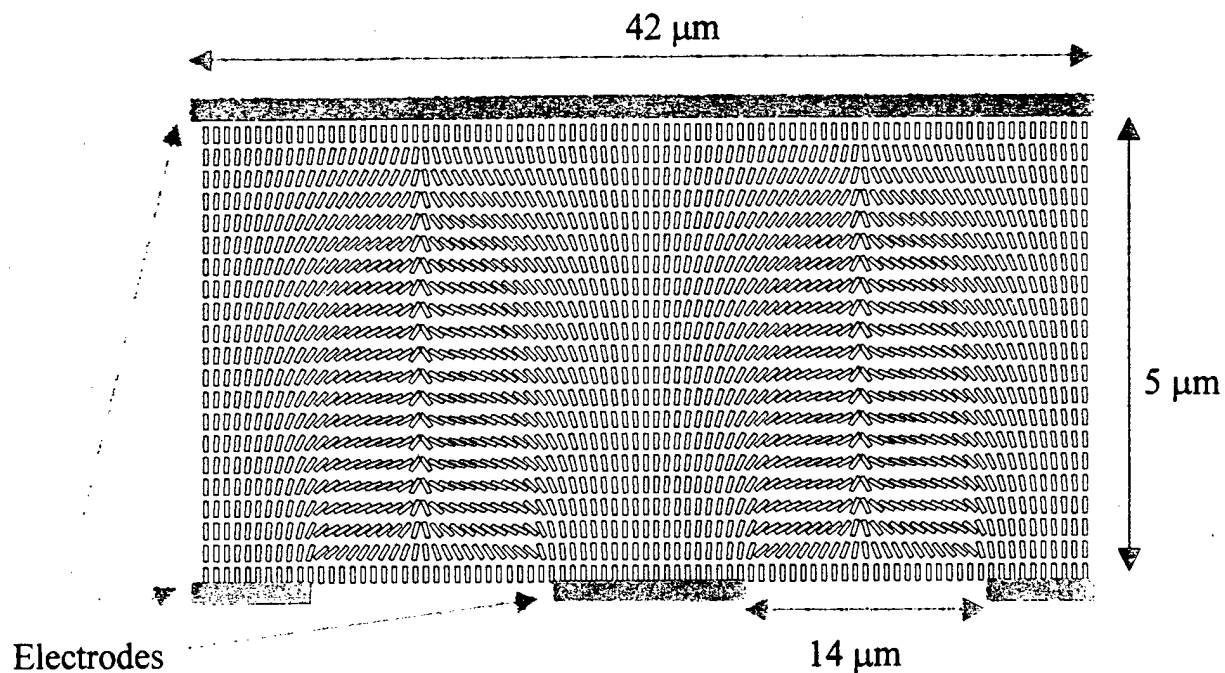


FIGURE 3.23 Vertically aligned in plane nematic structure with same voltage applied to each of three lower electrodes. Liquid crystal texture is undisturbed over the center of each electrode (only $\frac{1}{2}$ of the two outer electrodes is shown). Defects appear at the center of gaps between electrodes, extending to upper electrode.

intensity pattern is shown in Figure 3.20. There is still a near field intensity curve artifact resulting from the disclination, but it is not as pronounced.

The far field intensity distribution is shown in Figure 3.22. This was also calculated at a distance of one meter from the structure. The diffraction pattern of the e-mode simulation is not as concentrated as the o-mode run. This result is expected because of the reduced influence of the defect and the added near field artifacts corresponding to the edges of the lower electrode.

The second test structure is a double aperture in-plane liquid crystal structure, shown in Figure 3.23. Again, the common upper electrode is grounded. Equal voltages, well in excess of the Freedricksz threshold, were applied to

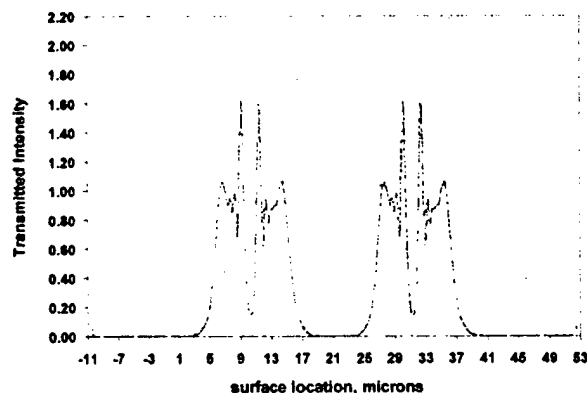


FIGURE 3.24 Surface intensity profile, partially activated vertically-aligned in plane nematic structure, normally dark mode.

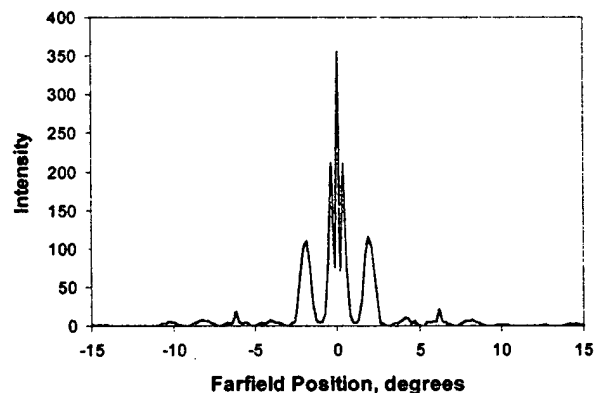


FIGURE 3.25 Surface intensity profile, partially activated twisted nematic structure, o-mode source, normally dark mode.

the three lower electrodes. Deformation is produced by fringing fields between neighboring lower electrodes. There are defects at the center of each field-influenced region.

The near field FDTD computation was performed with a normally incident source linearly polarized midway between the plane of the structure and a plane perpendicular to it. The exit polarizer absorption axis was rotated 90 degrees from the source. This is a normally dark mode of operation. The resulting intensity profile is shown in Figure 3.24. The locations of the two field-reoriented liquid crystal regions are evident. There is also evidence of the defect in each of those regions.

The far field diffraction pattern (Figure 3.25) was calculated as in the TN simulation. The far field pattern shows evidence of well-defined diffraction orders. This is the result of the inclusion of two identical and symmetrical "apertures" in the simulation. That is the type of far field behavior which will be expected from simulations of blazed-phase liquid crystal grating layers such as those employed for beam steering.

3.10 Status of Optical Simulation Software and Grating Calculations

The simulation method described up to this point still requires some modification before being capable of computing far field diffraction of a liquid crystal beam steering grating illuminated by a laser beam. The laser-illuminated grating problem is much larger than calculations performed up to this point, which have been carried out on a single microprocessor. Because we wish to illuminate the grating with a slowly diverging gaussian beam, that beam, in the visible spectrum, must possess an e^{-2} diameter on the order of 600 to 700 μm . In addition, we wish to limit diffractive artifacts resulting from lateral truncation of the gaussian beam on the FDTD grid. That would require the e^{-2} diameter be smaller than the structure it illuminates. A reasonable guess is that the grating should be the width of the e^{-4} diameter of the beam, approximately 1500 μm .

The intended computation will require more memory than available on a single desktop computer. The code must be modified for parallel execution on our multiprocessor computer, each node of which is in essence its own desktop computer. The total memory available in that system, approximately 4GB, is sufficient for the large grating calculation. In addition, the division of the task among the 16 processors in the system will permit completion of a single simulation in less than one day. Without that task division, a single processor with sufficient memory would require approximately two weeks to complete a single simulation.

This code modification is underway.

3.11 Conclusions – Optical Simulation of Liquid Crystal Beam Steering Devices

- There is existing software suitable for calculation of the director orientation distribution in two dimensional liquid crystal structures.
- We have developed FDTD software capable of simulating light transmission through liquid crystal structures possessing two-dimensional variation of director orientation, such as found in liquid crystal layers employed for blazed-phase beam steering gratings.

- We have compared FDTD near field results to analytical solutions for several liquid crystal problems with analytical solutions: the twisted nematic cell and Bragg reflection from a cholesteric layer. FDTD simulations are capable of closely duplicating the exact solutions.
- We have determined that the primitive Kirchhoff integral is a suitable means of calculating far field diffraction patterns from accurate near field distributions.
- We have developed software for carrying out that far field calculation.
- Some additional software modifications are still necessary to carry out full near and far field simulations of liquid crystal beam steering gratings. These modifications are underway.

4. CHOLESTERIC DIFFRACTION GRATINGS

4.1 Introduction

LC diffraction gratings have certain potential advantages over conventional ruled or holographic gratings. Large birefringence of LC's and a possibility to switch between 'on' and 'off' states using low-voltage electric fields make LC structures attractive for various applications in beam steering, diffractive optics, etc. The optical phased array technology, reviewed by McManamon *et al.*⁴, is the most developed concept of the liquid crystal beam steering devices^{4, 63,64,65,66,67}. The voltage applied to patterned electrodes produces an inhomogeneous periodic distortion of the director field in a nematic LC and results in the phase-modulated diffraction grating. A deflecting angle of the grating is determined by the distance between adjacent electrodes and by the number of electrodes, which produce a required phase profile.

We develop a concept of beam steering based on diffraction properties of the helical structure in cholesteric LC cells that are controlled by the electric field^{6,7,68,69}. An ideal cholesteric diffraction grating (CDG) should represent a uniform one-directional modulation in the plane of the cell. The director modulations originate in the natural tendency of the cholesteric LC to twist. The in-plane uniformity and amplitude of director distortions is achieved by balancing two additional factors: the dielectric coupling and the surface anchoring. The dielectric coupling keeps the twist axis in the plane of the cell, while the surface anchoring (e.g., due to mechanical rubbing of the boundary plates) orients the modulations along one direction in the plane of the cell. To improve the optical diffraction and dynamic properties of cholesteric gratings we performed extensive studies of the complex three-dimensional cholesteric structures that arise in the electric field and serve as the diffraction gratings. The numerical calculations based on the Frank-Oseen free energy density have been accompanied by confocal microscope studies that allow to decipher the structural features of the cross-section of liquid crystal cells.

Depending on the parameter $Q = \frac{2\pi \cdot m^2 \lambda d}{n \Lambda^2}$ (m is the diffraction order, λ is the wavelength, d is the thickness of the grating, Λ is the grating period and n is the spatially averaged refractive index of the diffractive medium) two types of diffraction can be distinguished. A 'thin' grating, $Q \ll 1$, determines the Raman-Nath diffraction when for normal incidence several diffraction orders $m = 0; \pm 1; \pm 2 \dots$ with the directions

$$\theta_m = \arcsin(m\lambda / \Lambda). \quad (4.1)$$

have noticeable intensity, Figure 4.1a. Here and below we measure all the angles from to the normal to the cell. A 'thick' grating, $Q \gg 1$, corresponds to the Bragg diffraction, Figure 4.1b, and can produce a strong diffraction maximum of the order m when the incident angle Θ satisfies the phase-matching condition

$$\Theta = \Theta_m = \arcsin(m\lambda / 2\Lambda). \quad (4.2)$$

The modulated state is capable of diffraction in both regimes, also the modulation period can be voltage controlled.

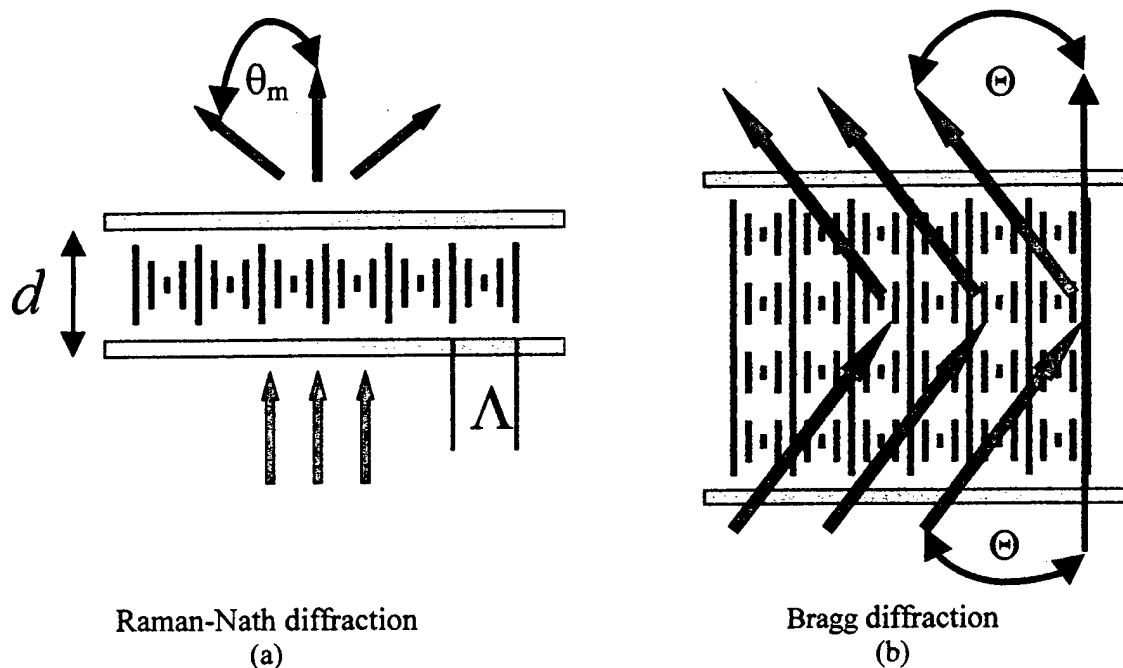


FIGURE 4.1. Two types of diffraction in a cholesteric cell.

4.2 Experimental

In the experiments we used nematic liquid crystal mixtures ZLI 5200-000 (E. Merck; $\epsilon_{\perp} = 3.6$, $\epsilon_a = 5.9$ at $f = 1$ kHz, refractive indices $n_o = 1.494$, $n_e = 1.614$ at 20°C and $\lambda = 633 \text{ nm}$) and LC E7 (E. Merck; $\epsilon_{\perp} = 5.2$, $\epsilon_a = 13.8$ at $f = 1$ kHz, refractive indices $n_o = 1.522$, $n_e = 1.746$ at 20°C). Nematic materials were doped with the chiral agent CB 15 (E. Merck; twisting power $-8 \mu\text{m}^{-1}$) to control the ratio d/p . Cells were vacuum filled. LC cells with planar anchoring were assembled from two glasses coated with ITO and polyimide aligning layers. In-plane homogeneous orientation was set by unidirectional buffing of the alignment layer. Measurements in similar nematic cells with planar anchoring show⁷⁰, that the pretilt angle is in the range $\theta_{\text{pretilt}} = 0 - 5^{\circ}$ and the polar anchoring coefficient is about $W_p \sim 10^{-4} \text{ J/m}^2$. Homeotropic anchoring was achieved by using lecithin alignment layers. Thickness of the liquid crystal slabs was set by spacers in the range $d = 2 - 20 \mu\text{m}$.

Olympus Fluoview fluorescent confocal microscope was used to study the internal structure of modulated states. A fluorescent Rhodamine 590 dye was added (0.01–0.05 wt%) to the cholesteric mixture for confocal-microscopy studies. Laser light from Ar^+ laser excites the dye molecules within the sample, the dye fluoresce revealing the sample structure. The concentration of dye was limited to avoid aggregates that might distort the LC host. Although the confocal microscopy does not provide one-to-one correspondence between the director configuration and its image as the polarizing microscopy (with an appropriate accessories such as quarter-wave plates) does, it is still of a great value. A unique advantage is that the confocal microscopy reveals the symmetry of director configurations both in the plane of the liquid-crystal slab and in the plane normal to the slab.

The diffraction experiments were performed with He-Ne laser ($\lambda = 633$ nm). The laser beam was directed through the linear polarizer whose orientation was controlled by Newport rotary stage 495. The polarized beam was incident normally to the cell. The diffracted light intensity was measured by photodiod separately for the different locations of diffraction maxima.

4.3 Homogeneous Modulated Textures

To achieve the most appropriate optical and dynamic properties of CDG we performed extensive studies of the complex three-dimensional cholesteric structures that arise in the electric field and serve as the diffraction gratings. The standard experiments (optical diffraction and polarizing microscopy) have been accompanied by (a) numerical simulations of equilibrium structures based on the Frank-Oseen free energy density minimization⁷¹ and (b) confocal microscope studies that allow to decipher the structural features of the cross-section of liquid crystal cells. We studied cells with both planar and homeotropic alignment. In cells with planar alignment director has on the substrates either parallel orientation (unidirectional cell) or perpendicular orientation (twist cell).

4.3.1. Planar unidirectional cells.

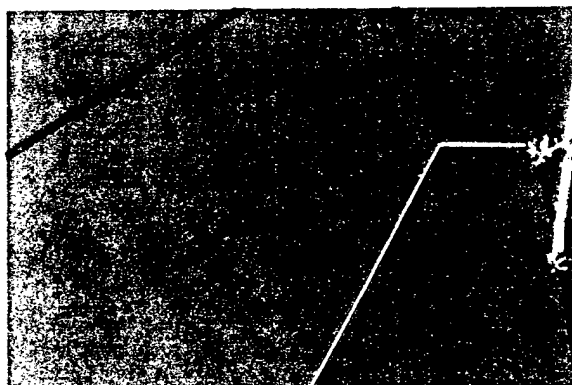
Cells with planar alignment and parallel easy axes on the substrates (unidirectional cell) are the most obvious candidates for CDG. Figure 4.2 shows typical polarizing-microscope textures in a unidirectional cell. The zero-field state is a planar state with cholesteric layers and molecules parallel to the cell substrates, Figure 4.2a. For planar alignment, we deciphered one of the important mechanisms of the planar-modulated structural transition⁷². Responsible for the planar-modulated transition are large dislocation bands (so-called oily streaks, exhibit as lines in Fig.4.2a) in cholesteric planar cells. The formation and propagation of oily streaks should be considered undesirable since at some voltage the line tension of the oily streaks becomes negative and the oily streaks tend to deviate from a direction set by the surface alignment; these deviations cause light scattering at the cholesteric cells. The oily streaks can be eliminated in a cholesteric liquid crystal with dielectric anisotropy that depends on the frequency of the applied signal. Such mixtures are called dual-frequency mixtures. When the dielectric anisotropy is negative, the applied electric field eliminates the oily streaks. At different frequency, the anisotropy is positive, and the electric field causes modulated structure without oily streaks.

For high voltage the structure also becomes in-plane homogeneous, Figure 4.2b. It looks like almost homeotropic but some optical activity caused by twist distortions remains. At intermediate voltages, we obtain a modulated state with stripes oriented parallel to the rubbing direction, Figure 4.2c.

(a) Stripes parallel to the rub direction

To study a fine structure of the textures numerical simulations of equilibrium structures based on the Frank-Oseen free energy density minimization has been developed. Mathematical basis of simulations is presented in Appendix A. Figure 4.3 shows computer-simulated cholesteric structures resulting from the balance of intrinsic twisting power, finite surface anchoring (favoring planar alignment) and dielectric coupling to the electric field. The parameters chosen are the same as of the material in our experiments. The zero-field state is a planar state with cholesteric layers and molecules parallel to the cell substrates, Figure 4.3a. For high voltage the structure in the bulk becomes

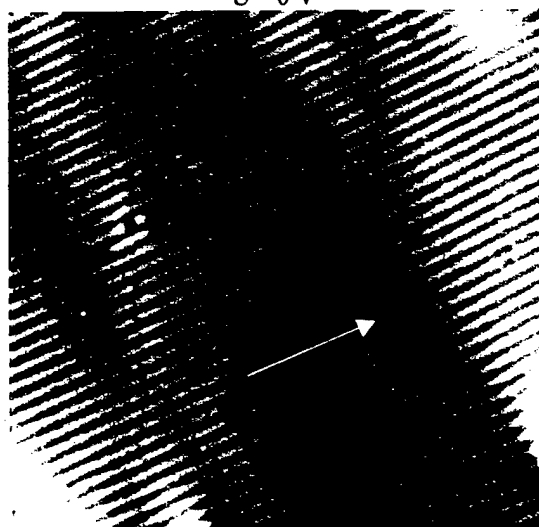
layers and molecules parallel to the cell substrates, Figure 4.3a. For high voltage the structure in the bulk becomes an almost ideal homeotropic but near the surfaces the molecules are not reoriented completely, Figure 4.3b. At intermediate voltages, we have obtained two modulated states with stripes oriented parallel to the rubbing direction: one is almost ideal cholesteric structure with surface defects (surface director is not planar), Figure 4.3c, and another is a complex double-twist structure that almost satisfies to the anchoring conditions on the substrates, Figure 4.3d.



(a) planar structure
 $U = 0 \text{ V}$

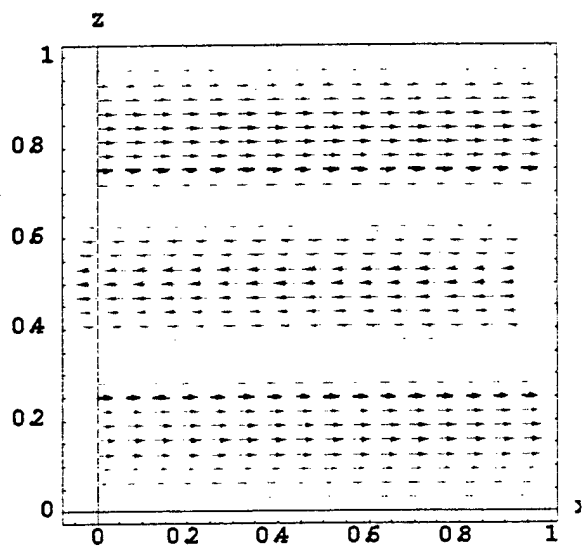


(b) conical homeotropic structure
 $U = 2.6 \text{ V}$

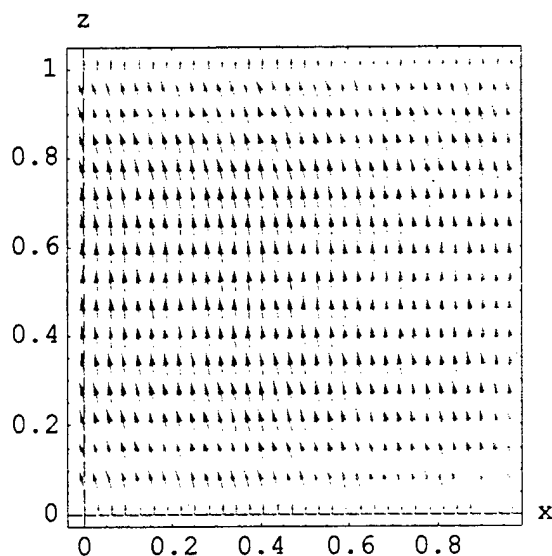


(c) parallel stripes
 $U = 1.1 \text{ V}$

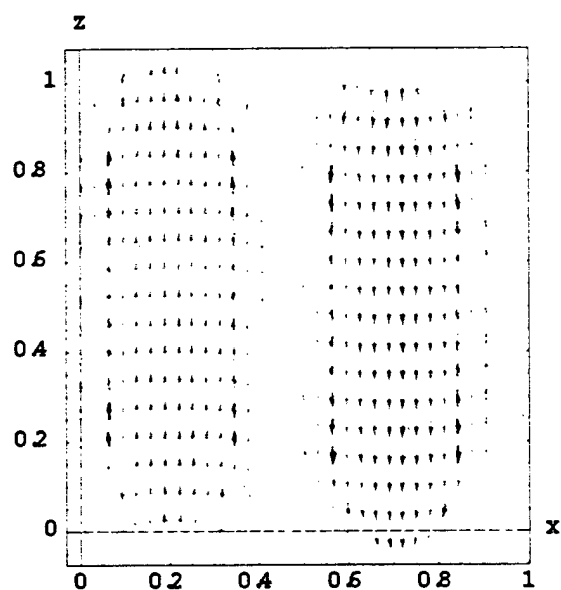
FIGURE 4.2. Polarizing-microscope textures in a cell with planar unidirectional alignment; the arrow shows the rubbing direction.



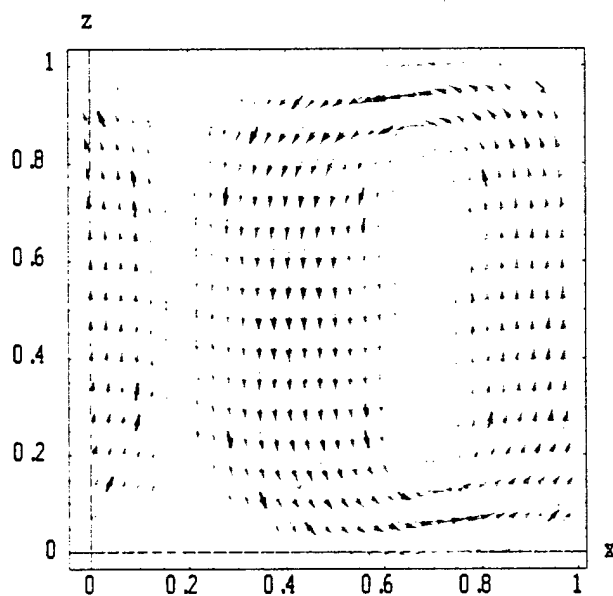
(a) planar structure
 $E_z = 0$



(b) conical homeotropic structure
 $E_z = 0.8 \text{ V}/\mu\text{m}$



(c) symmetrical stripes
 $E_z = 0.72 \text{ V}/\mu\text{m}$



(d) asymmetrical stripes
 $E_z = 0.72 \text{ V}/\mu\text{m}$

FIGURE 4.3. Computer-simulated cholesteric structures ($p = 1.67 \mu\text{m}$, elastic constants and dielectric correspond to E7) in a cell with thickness $d = 2.5 \mu\text{m}$ and planar unidirectional alignment (polar anchoring coefficient $4 \times 10^{-5} \text{ J}/\text{m}^2$, azimuthal anchoring coefficient $2 \times 10^{-5} \text{ J}/\text{m}^2$): (a) voltage $U = 0.0 \text{ V}$; (b) $U = 2.0 \text{ V}$; (c) and (d) $U = 1.8 \text{ V}$. The electric field is oriented along the axis z and rubbing is along the axis y .

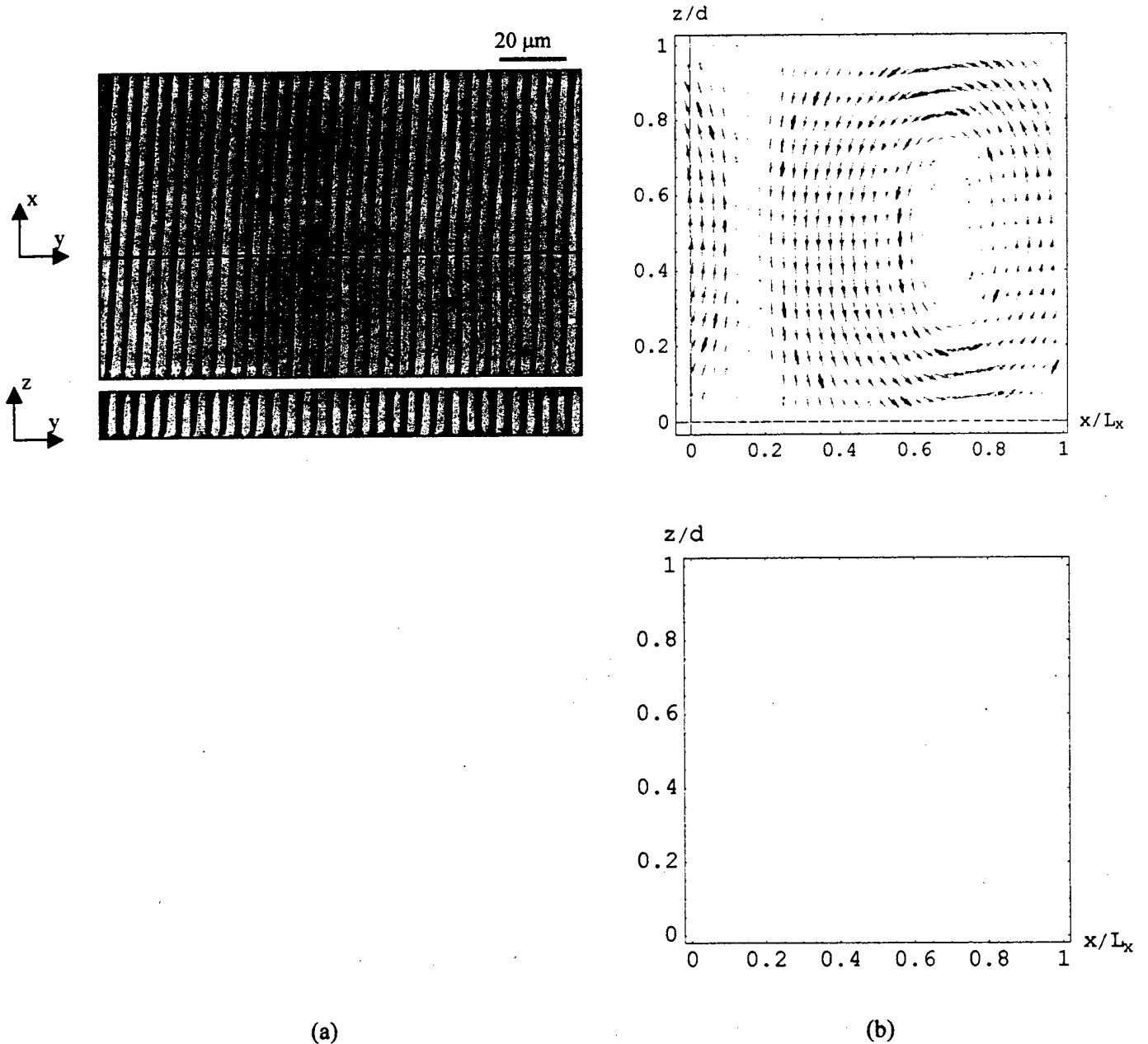


FIGURE 4.4. Confocal microscope image (a) and computer simulations (b) of growing stripes (I) in a cholesteric cell. Computer simulations (director field – top, set of equipotential lines – bottom) used the following parameters: $p = 10 \mu\text{m}$, elastic constants and dielectric correspond to E7, the cell has thickness $d = 10 \mu\text{m}$ and planar unidirectional alignment ($\theta_{\text{pretilt}} = 3^\circ$, polar anchoring coefficient $4 \times 10^{-5} \text{ J/m}^2$, azimuthal anchoring coefficient $2 \times 10^{-5} \text{ J/m}^2$), applied voltage $U = 1.7 \text{ V}$. The bounding substrates are normal to the axis z and the rub direction is along the axis y .

Both structures have approximately the same free energy, thus to clarify which one is usually realized in experiments, we performed confocal-microscope studies of the modulated state in the plane of the cell and in the

vertical cross-section, Figure 4.4a. For better resolution the images were obtained for a cell with a higher pitch ($p = 10\mu\text{m}$) and with the ratio $d/p \sim 1$. The apparent periodicity of the structure, as seen in the plane of the cell, is the distance between two consecutive bright stripes. However, the cross-section examination clearly reveals that the true periodicity is twice as large: odd and even stripes have different heights. Thus, although the periodicity in the bulk roughly corresponds to $p/2$, the surface periodicity is close to p . This surface symmetry-breaking effect is reproduced by computer simulations in Figure 4.4b and provides the weak odd-order diffraction maxima, described below, Figure 4.12.

(b) Stripes perpendicular to the rub direction

We have recently found a new type of modulated cholesteric patterns that can be created by a careful adjustment of the cell parameters⁶⁹. The results described below were obtained for a cell with $p = 5\mu\text{m}$ and $d = 5 \pm 0.2\mu\text{m}$ ($d/p \approx 1$) and anti-parallel easy axes on the bounding plates. In zero field the texture is uniformly planar with small number of defects whereas in the strong field ($V > 5V$) it changes to a homogeneous conical (almost homeotropic) texture. Two kinds of modulated patterns are observed for the intermediate voltages, Figure 4.5, that differ both in the scenario of appearance and in orientation with respect to the rub direction.

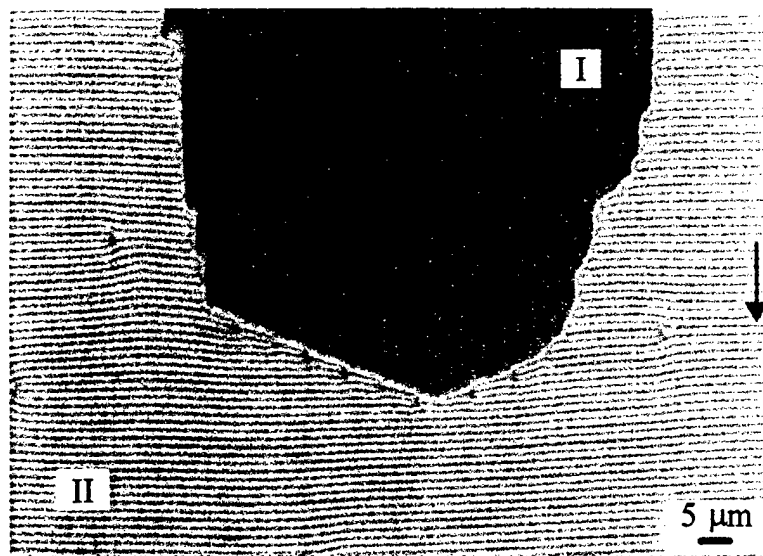


FIGURE 4.5. Polarizing microscope picture of both types of modulations: I – growing; II – developable; vertical arrow shows the rub direction.

- (I) **Stripes parallel to the rub direction.** These stripes initially *nucleate* near spacers and other defects as circular zones; their further expansion proceeds by splitting the center and forming a stripe cupped by two semicircles. The stripe elongates along the rub direction filling the available space.

- (II) *Modulations perpendicular to the rub direction.* Periodic one-dimensional modulation appears simultaneously all over the domain. There is no increase in the length of perturbations, as this length is defined by the size of the sample or by the size of the available domain at the very beginning of the instability. The modulations develop like a photographic image, i.e., by enhancing the optical contrast rather than by propagation in space. We will refer to these modulations as 'developable' modulations to distinguish them from 'growing' modulations of type (I).

Domains of developable and growing modulations co-exist, Figure 4.5. By changing the applied voltage it is possible to move the boundary between two domains either way. Note that in Figure 4.5 the stripes in co-existing domains are perpendicular to each other.

Computer simulations and confocal-microscope studies of the developable modulations (Figure 4.6) indicate that their structure differs drastically from growing stripes and that these modulations appear as result of dielectric instability that is similar to the Helfrich – Hurault instability in multi-layered ($d/p \gg 1$) systems. Computer simulations allow one to interpret the features of the confocal image. The two adjacent dark bands are different because of the non-zero pretilt angle (with a zero pretilt they would be identical). The two adjacent bright bands are different because of the lack of mirror symmetry (with respect to the middle plane of the cell) combined with the dye-induced absorbance. Note an important feature of the developable modulations clearly visible in Figure 4.6: the 'right' and 'left' halves of the period are asymmetric. This asymmetry feature is crucial for the development of blazed cholesteric gratings in which one branch of diffractive orders is cut off.

4.3.2. Planar twist cells.

Cells with planar alignment and perpendicular easy axes on the substrates (twist cells) have been also studied for creation of CDG. In a twist cell, the zero-field planar texture and the high field homeotropic texture are very similar to the same textures in a unidirectional cell. At intermediate voltages, we also obtain a modulated texture but stripes are oriented at $\pm 45^\circ$ from the rubbing directions. The sign is determined by the handedness of the cholesteric mixture. The polarizing-microscope image and the computer-simulated structure show, Figure 4.7, that the modulated text is the double-twist structure with surface symmetry-breaking (double periodicity) effect. Note that this experiment and simulations have been done for the mixture based on ZLI 5200-000, which has less dielectric anisotropy, than E7, and therefore less inhomogeneity of the electric field (Figure 4.7b).

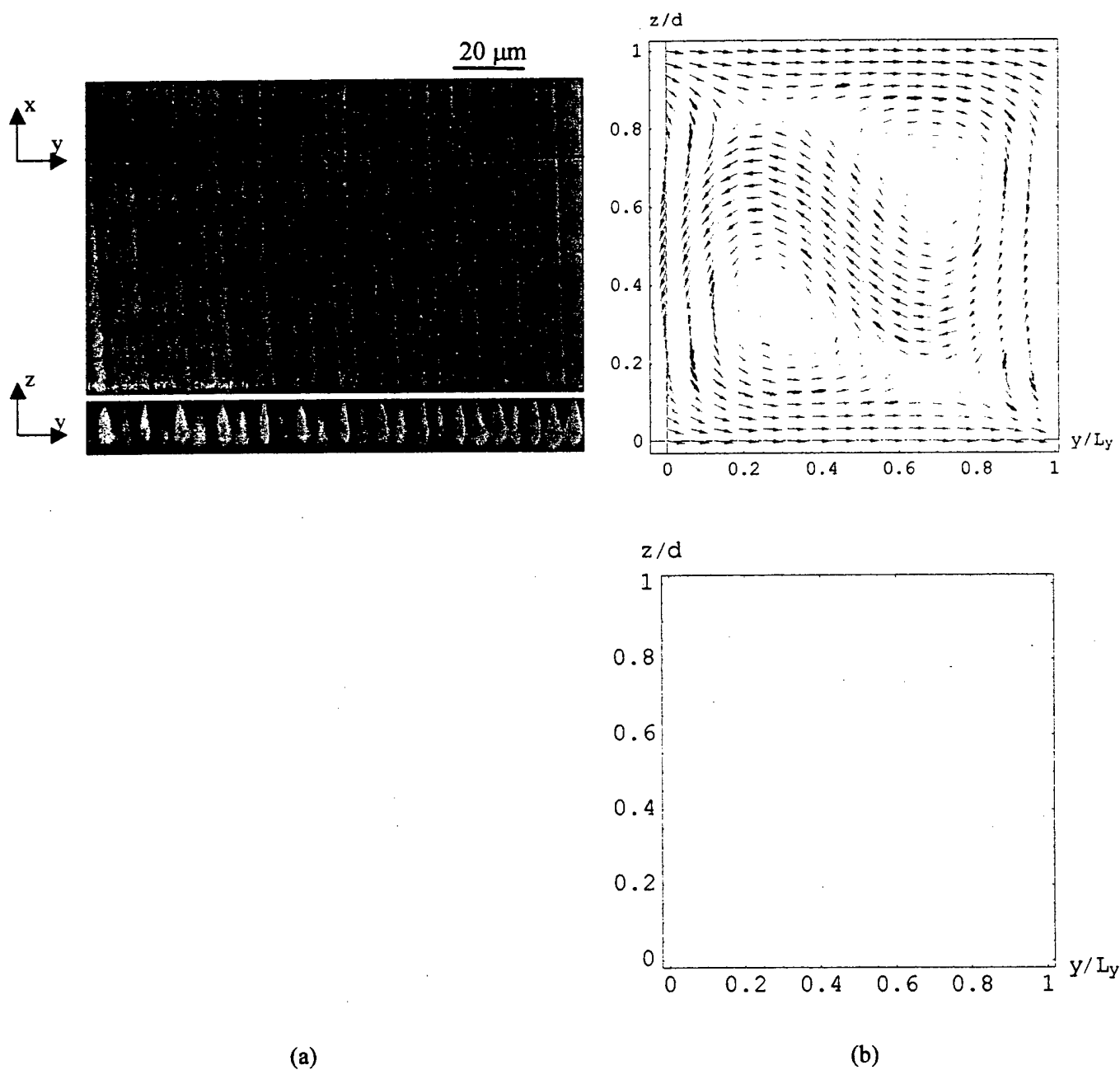


FIGURE 4.6. Confocal microscope image (a) and computer simulations (b) of developable modulations (II) in a cholesteric cell. Computer simulations (director field – top, set of equipotential lines – bottom) used the same parameters as in Figure 4.4: applied voltage $U = 1.8\ \text{V}$. The bounding substrates are normal to the axis z and the rub direction is along the axis y .

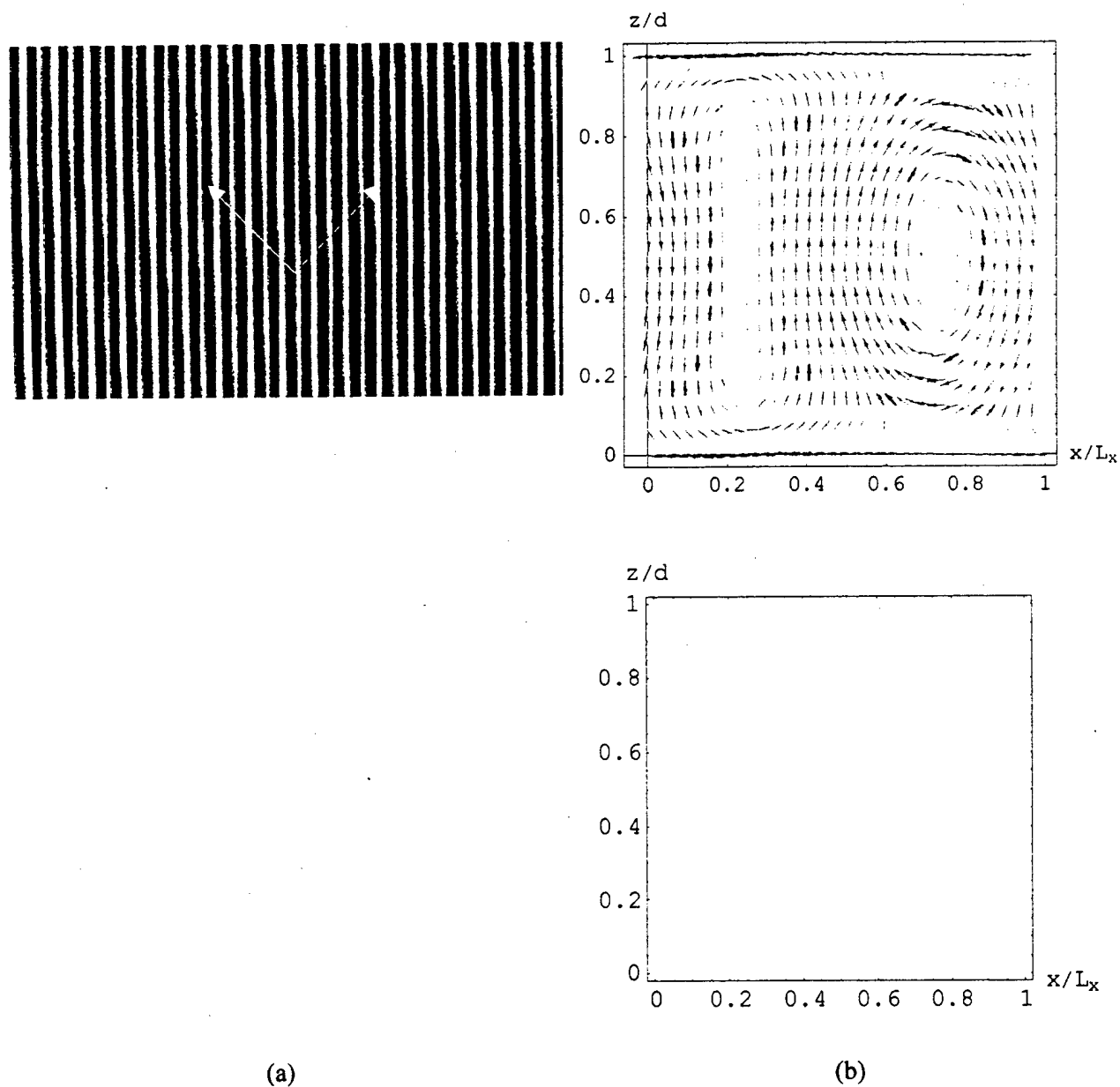


FIGURE 4.7. Polarizing microscope texture (a) and computer simulations (b) of the modulated state in the twist cell (ZLI 5200-000 + CB15). Computer simulations (director field – top, set of equipotential lines – bottom) used the parameters for ZLI 5200-000; applied voltage $U = 4.0$ V. The bounding substrates are normal to the axis z and the rub directions are oriented at $\pm 45^\circ$ the axis y (white arrows).

4.3.3. Homeotropic cells

Modulated states with beam-steering effect can also be created in cells with homeotropic anchoring. The advantage is that in this geometry the modulations are stable in zero-field. For homeotropic anchoring all in-plane directions are equivalent, so the orientations and the uniformity of modulations was set by an in-plane magnetic field Figure 4.8. The uniform structure was preserved even when the magnetic field was removed (Figure 4.9a) and when electric field was applied, Figure 4.9b, up to complete transformation to the homogeneous homeotropic state.

Figure 4.10 shows computer-simulated cholesteric structures for homeotropic anchoring. At high voltage the structure is strictly homeotropic, Figure 4.10a. Another in-plane homogeneous state is a planar in the bulk and conical near the surfaces, Figure 4.10b. This state is metastable in zero-field because two modifications of the modulated state, Figure 4.10c and Figure 4.10d, have lower free energy. Both structures are realized in experiments; thin symmetric stripes (Figure 4.10c) appear after phase transition from the isotropic phase, whereas thick asymmetric stripes (Figure 4.10d) appear during the transformation from the homeotropic state (Figure 4.9) and are applicable for the beam-steering effect.

Comparison the confocal microscope image, Figure 4.11a, and the computer-simulated structure, Figure 4.11b, of thick stripes in zero-field for homeotropic anchoring shows that the simulated structure reproduces correctly the diamond shape of stripe's vertical cross-section on the confocal image and even the diamond distortion.

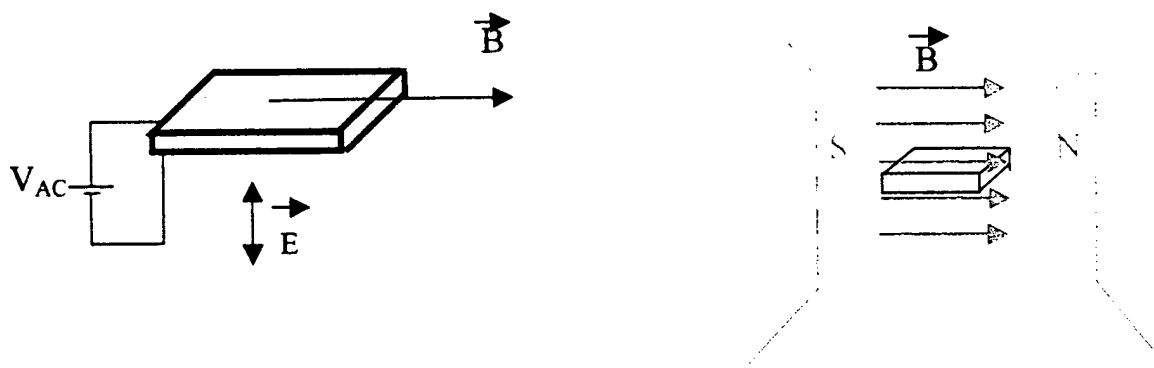
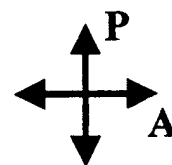
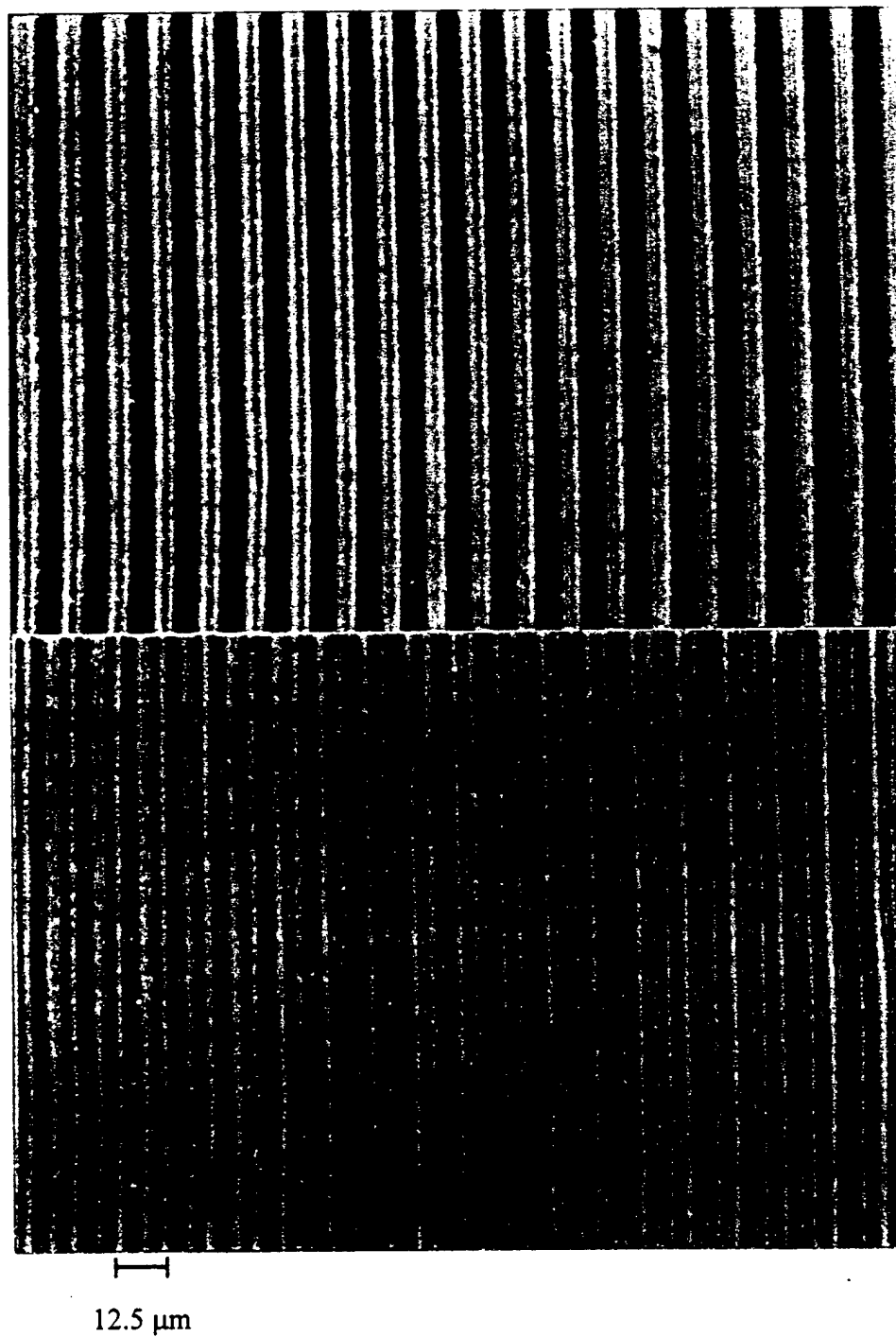


FIGURE 4.8. Geometry to grow stripes in a homeotropically aligned cholesteric cell: on the left, - magnetic and electric fields are both necessary; on the right, - orientation of the cell in the magnetic field.



(a)

$U = 3 \text{ V}$

$f = 200 \text{ kHz}$

(b)

$U = 0 \text{ V}$

FIGURE 4.9. Stripes in a homeotropically aligned cholesteric cell: $d/p \sim 1$, $p = 10 \mu\text{m}$, (a) voltage is 'on', (b) voltage is 'off'.

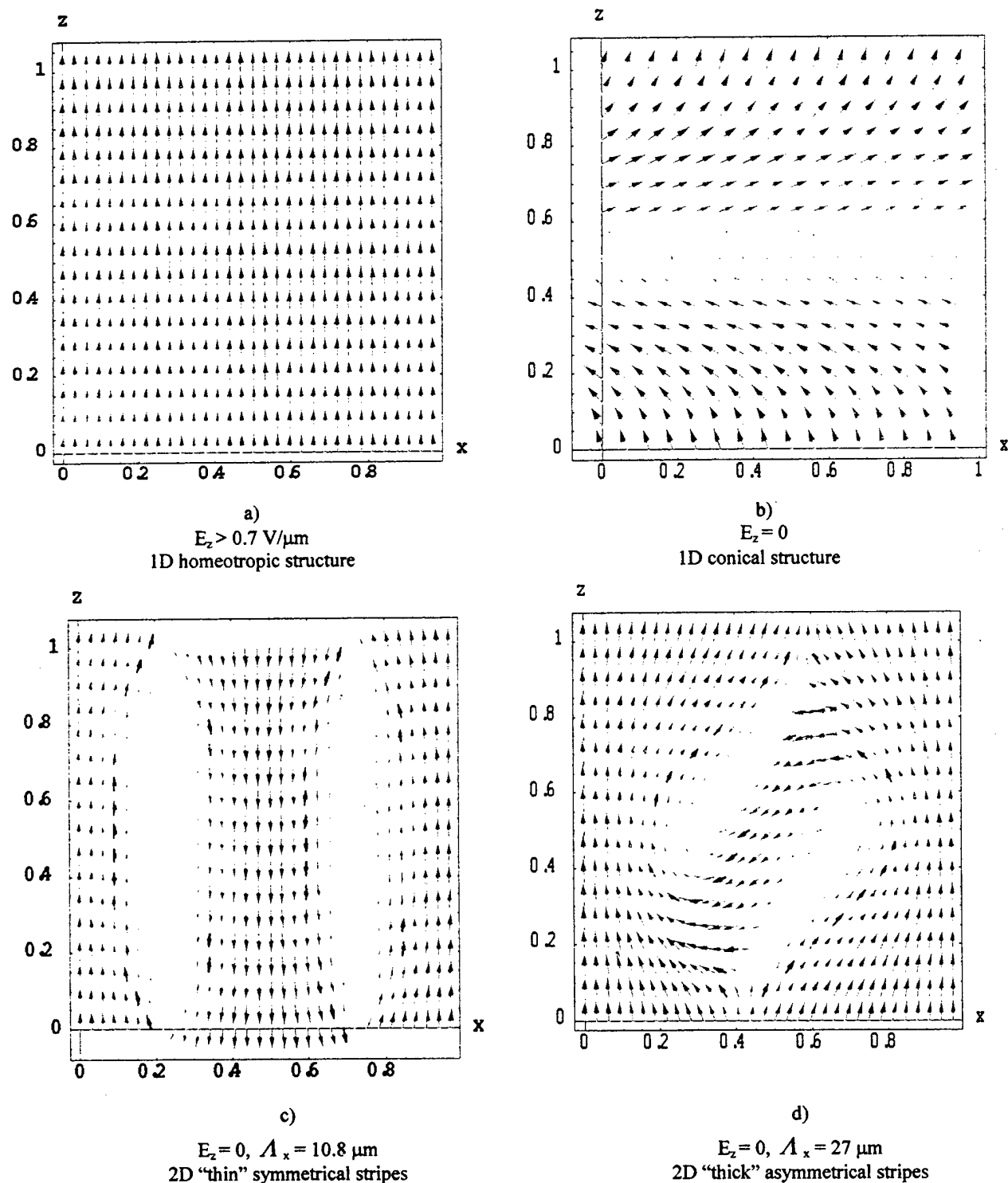


FIGURE 4.10. Computer-simulated cholesteric structures for homeotropic alignment ($p = 10 \mu\text{m}$, $d = 10 \mu\text{m}$, Polar anchoring coefficient $2 \times 10^{-5} \text{ J/m}^2$. The rest of the parameters are the same as in Fig.4.4. a) applied voltage $U > 4 \text{ V}$; b), c) and d) $U = 0 \text{ V}$.

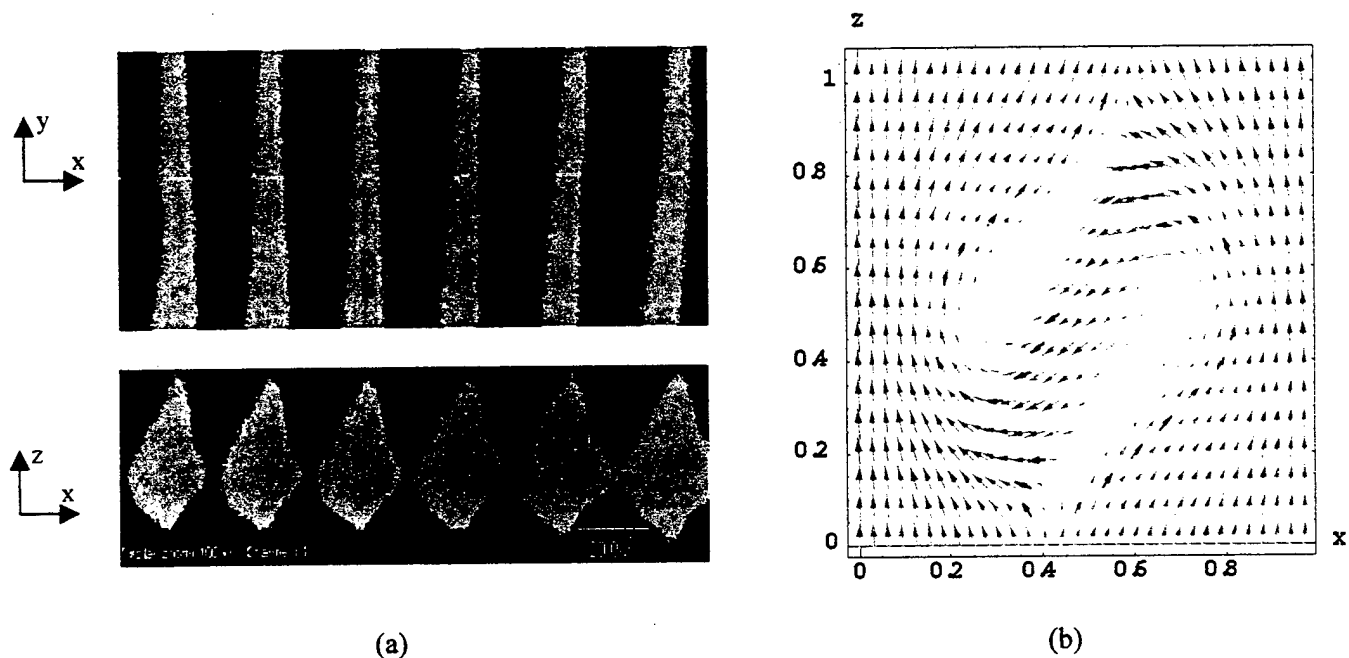


FIGURE 4.11. Confocal microscope image (a) and computer simulations (b) of the thick stripes in the homeotropic cholesteric cell. Computer simulations used the are the same as in Fig.4.10, no applied voltage. The bounding substrates are normal to the axis z .

4.4. Optical and Dynamical Properties of CDG

Depending on the cell design (thickness d , cholesteric pitch p , etc.) we obtain two modes of operation. The first is an electrically-switchable CDG (the periodicity in the modulated state does not depend on the applied field); the optical beam is deflected in a discrete mode. The second kind of CDG is both electrically-switchable and electrically-controlled: the period of the grating in the M state changes with the applied voltage. The beam is steered continuously.

4.4.1. Electrically-Switchable CDG

We designed electrically switchable CDG of the Raman-Nath type⁷. These CDGs appear in unidirectional or twist planar cells and in homeotropic cells with $d \approx p \geq 5\mu m$. Figure 4.12 shows a typical diffraction pattern of modulated state in unidirectional or twist planar cell for the light polarized along the rubbing direction of the front plate. There is no analyzer in the system. The diffraction pattern is rather unusual. First, the strongest maxima are the second-order-ones. The diffraction angle for the 2nd maxima is approximately 5° . Two first order maxima are visible, but they are much weaker, Figure 4.12a. Higher order (3,4,...) maxima are hard to detect when the voltage is small. However they appear as the field increases, Figure 4.12b.

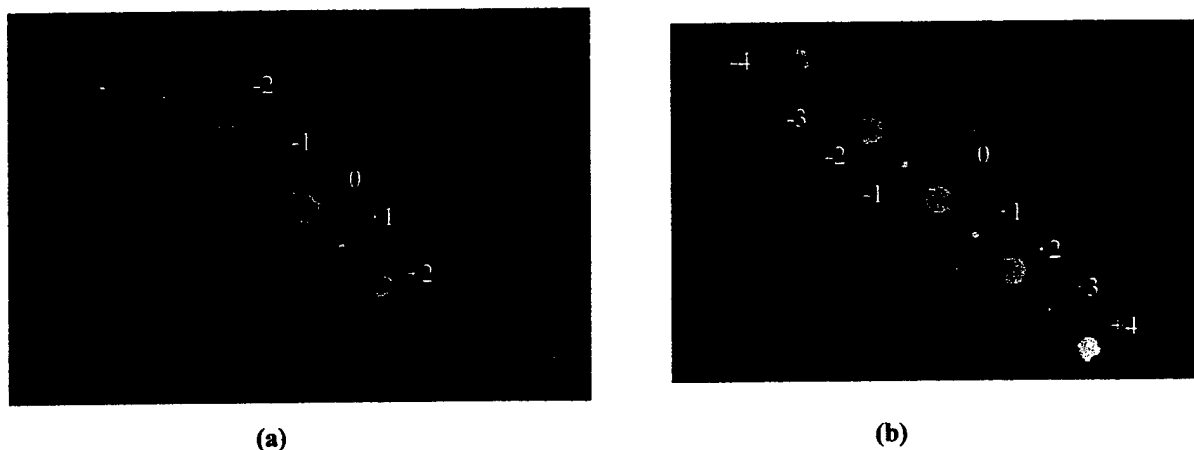


FIGURE 4.12. Typical diffraction patterns for the cell with planar alignment at: $U = 4.0 \text{ V}$ (a) and $U = 4.4 \text{ V}$ (b); diffraction angle is 5.5° for the intense 2nd order maximum.

Voltage dependencies of the diffraction intensities for the 0th and 2nd maxima are shown in Figure 4.13. Voltage scan rate was 1 mV/sec. Incident light is polarized along the rubbing direction of the front plate. Two voltage regions should be considered separately. In the region from $U_c = 3.9 \text{ V}$ to $U = 4.5 \text{ V}$ the diffraction pattern is stable, Figure 4.14. Voltages higher than $U > 4.5 \text{ V}$ give unstable patterns with moving dislocations. The diffraction pattern slowly evolves (Figure 4.14) and show significant scattering.

Another mode of CDG switching is from the homeotropic orientation at high applied voltages, $U = (9 - 15) \text{ V}$, to M-state (voltage $4 \text{ V} < U < 4.4 \text{ V}$). Again, switching to $U > 4.5 \text{ V}$ gives a non-equilibrium defect state.

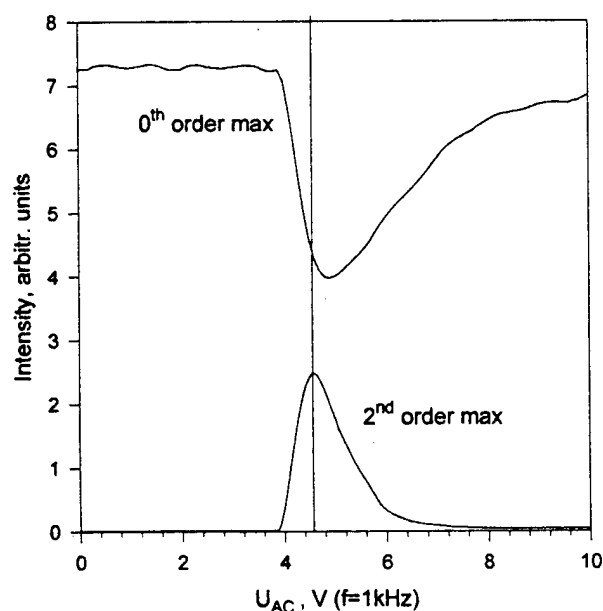


FIGURE 4.13 Voltage dependence of diffraction intensity for 0-th and two 2-nd order maxima in twist cell.

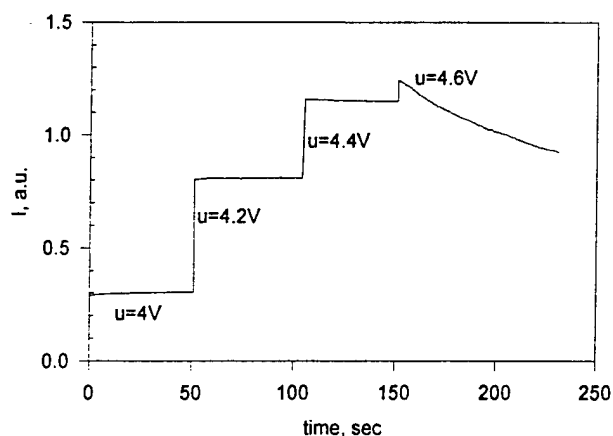


FIGURE 4.14. The 2-nd order maximum diffraction intensity vs. time at different applied voltages in twist cell.

The dependencies of the diffraction efficiency on the incident light polarization direction are different for the unidirectional and twist planar cells, Figure 4.15. In the unidirectional planar cell, the most intensive second order diffraction can be suppressed almost completely when the polarization of the incident light is perpendicular to the rubbing direction. In the twist cell, the second order diffraction also depends on the polarization of the incident light but the ratio between maximum and minimum the intensities does not exceed four.

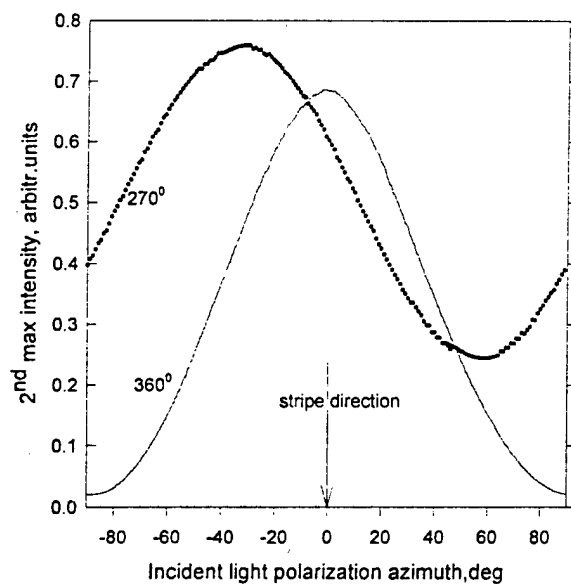


FIGURE 4.15. Diffraction intensity vs. direction of the incident light polarization for twist (270°) and unidirectional (360°) cells ($U=4.2V$). No analyzer is present. Polarizer orientation angle 0° corresponds to the stripe orientation in the cell.

To measure diffraction grating response time the switching was performed by applying voltage steps of $f = 10\text{-}20\text{ Hz}$ from 0 V to 4.4 V and measuring optical response of the 2nd order max using the oscilloscope. The growth and decay time (intensity change to 90% from the initial value) is of the order of $20\text{-}30\text{ msec}$, Figure 4.16. The measured response times ($\sim 20\text{ msec}$) are in good agreement with the well-known estimate of the relaxation time of the helical structure $\tau \sim \gamma_1 D^2 / 4\pi^2 K$, where D is the characteristic length of the system (in our case $D \approx d \approx p$), γ_1 is the viscosity coefficient, K is an effective elastic constant⁷³. With typical $\gamma_1 \approx 200\text{ mPa}\cdot\text{s}$, $K \approx 10^{-11}\text{ N}$ and $D \approx 5\text{ }\mu\text{m}$ one gets $\tau \approx 20\text{ ms}$.

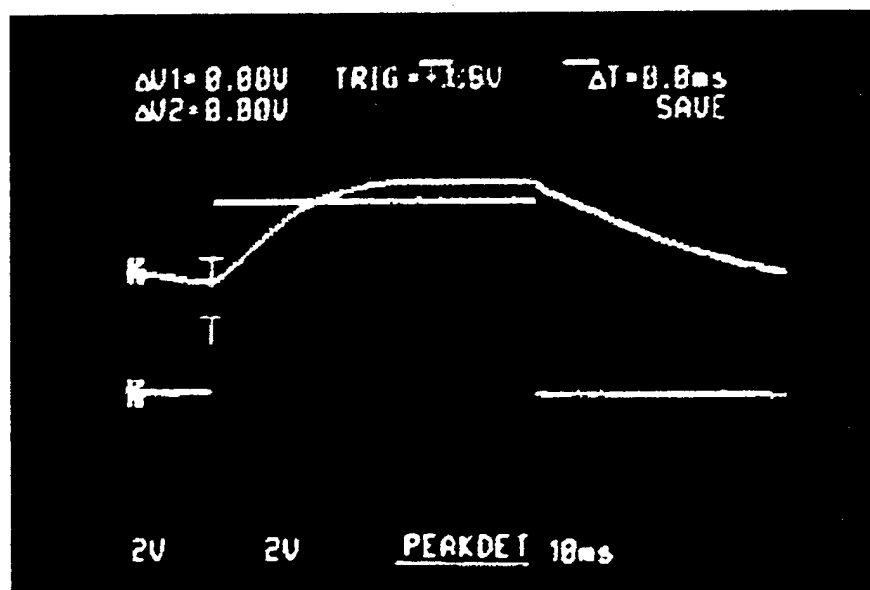


FIGURE 4.16. Oscilloscope picture of the optical response of the 2-nd order diffraction maximum.

The Raman-Nath diffraction is also observed in cells with homeotropic anchoring. The switching time from modulated (zero-field) to the homeotropic state depends on applied voltage and the cell thickness, Figure 4.17, and varies from 5 msec (for $V = 5\text{ V}$) to 40 msec (for $V = 1.2\text{ V}$, which is near the threshold voltage). The reverse transition from homeotropic to modulated state is about 0.1 s .

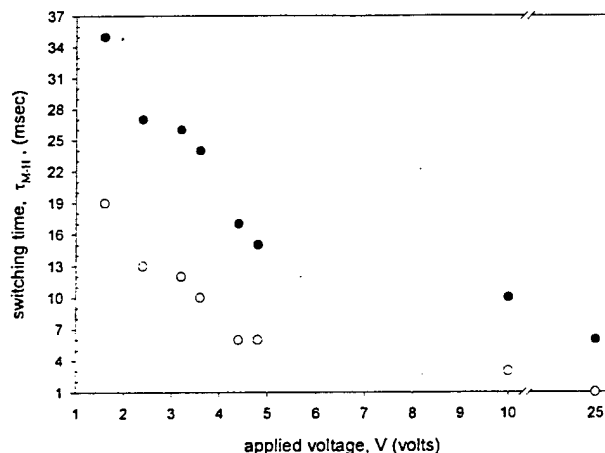


FIGURE 4.17. Switching time of M-H transition vs. applied voltage for cells with different thickness (closed circles – 5.0 μm , open circles – 1.9 μm). Both cells have the same structures (homeotropic anchoring, $d/p \sim 1$).

Polymer stabilization of electrically-switchable CDG

The distribution of the electric field is not uniform inside the cholesteric cell, as clearly seen in Figure 4.3b and Figure 4.4b. As recent studies by J. West's group at the LCI demonstrate^{74,75}, phase separation of a polymer and a liquid crystal in the presence of a non-uniform electric field results in spatial redistribution: the polymer concentrates in regions with a lower field. In the original West's approach, one uses patterned electrodes to create the field gradients. We decided to use the intrinsic modulation of the electric field in the cholesteric cells. This modulation occurs because of the dielectric anisotropy of the liquid crystal and does not require patterned electrodes. Our previous results demonstrated that a photoinduced separation in cholesteric gratings is indeed possible when the photosensitive material is a low-molecular-weight dye⁷⁶. Besides, the approach was also indirectly supported by the studies of photo segregation effects in another layered liquid crystals, namely smectic A phases. Our group at Kent performed experiments and N.A. Clark's group at Boulder performed computer simulations that led to the conclusion of nano-scale segregation induced by light irradiation of layered structures⁷⁷.

To verify the idea for polymer materials formed in cholesteric gratings, we used a cholesteric mixture E7 and CB15 and added 10 wt % of a photo polymerizable material Norland 65. The cholesteric pitch of the mixture was $p \sim 6 \mu\text{m}$. The thickness of cells with planar alignment layer was fixed at $d \sim 7 \mu\text{m}$. The electric voltage $V = 2.6 \text{ V}$ ($f = 1 \text{ kHz}$) was applied to the ITO layers at the bounding plates to cause the fingerprint texture. The sample was then illuminated with a UV light with a wavelength 366 nm. Light-induced polymerization was accompanied by spatial separation of the polymer and the liquid crystal and formation of walls along the cholesteric fingers. Note that the walls are located in the regions of planar director orientation, where the electric field is low.

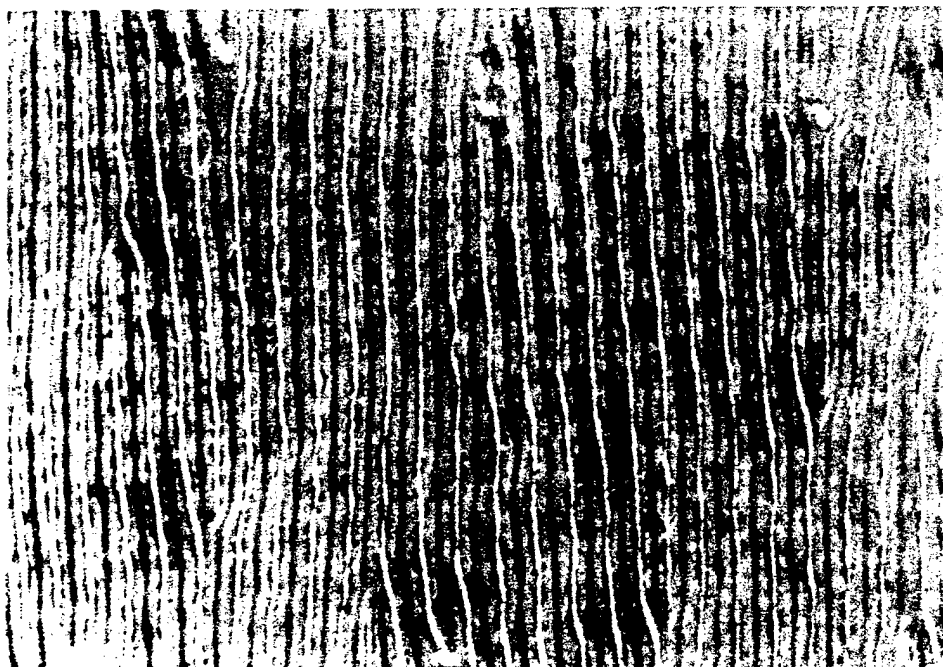


FIGURE 4.18. Polymer walls along the cholesteric fingers

Our preliminary data indicate an even more exciting scenario: if the light-induced polymerization takes place in a cell where the director modulations are stabilized by means other than the electric field, it still might result in a non-homogeneous polymer architecture.

4.4.2. Electrically-Controlled CDG

Grating with a field-controlled period in the M-state was obtained by decreasing d and p . Our studies show that for small d and p (about 1-2 μm) the period of modulated structure strongly depends on applied voltage. Typical changes of polarizing textures are in Figure 4.19. Both the Bragg and Raman-Nath diffraction regimes can be achieved⁶.

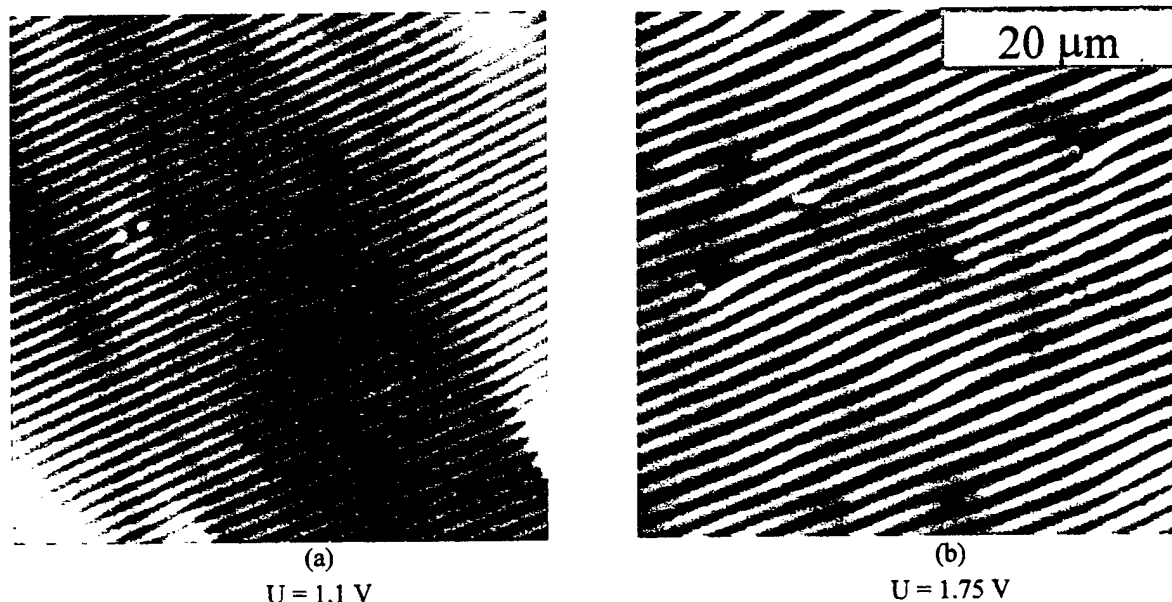


FIGURE 4.19. Polarizing-microscope textures in a cell with thickness $d = 2.5 \mu m$ and planar alignment.

Raman-Nath diffraction

The Raman-Nath diffraction with visible $0, \pm 1, \pm 2, \pm 3$ diffraction orders for a beam incident normally to the cell is observed in cells with $d/p < 2$. Decreasing d and p in comparison with the electrically-switchable CDG (with constant period) does not change the diffraction pattern, Figure 4.12. The only difference is the increase of the diffraction angle according to Eqn.(4.1). Figure 4.20 shows how the diffraction angle of the main maximum (2nd order) depends on the applied voltage. The grating period Λ is presented as the function of U in the insert. This period corresponds to the distance between the stripes in Figure 4.19. The field dependence of Λ produces a beam steering effect. For the fixed incident beam, a variation of U results in a continuous deflection of the diffracted beam (within an angular sector about 20°).

Figure 4.21 illustrates how the applied voltage changes the diffracted intensity for the 0th, 1st and 2nd order maxima. Near the transition to the homeotropic state the intensity of the 1st order maxima increases and becomes comparable with the intensity of the 2nd order maxima.

The time response of the transition to the homeotropic state is of the order of 10 msec. The complete reverse transition from the homeotropic state takes seconds. The transitions between the modulated state and the planar state are somehow slower: the transition to the planar state takes about 0.2 sec and transitions from the planar state takes about 2 sec.

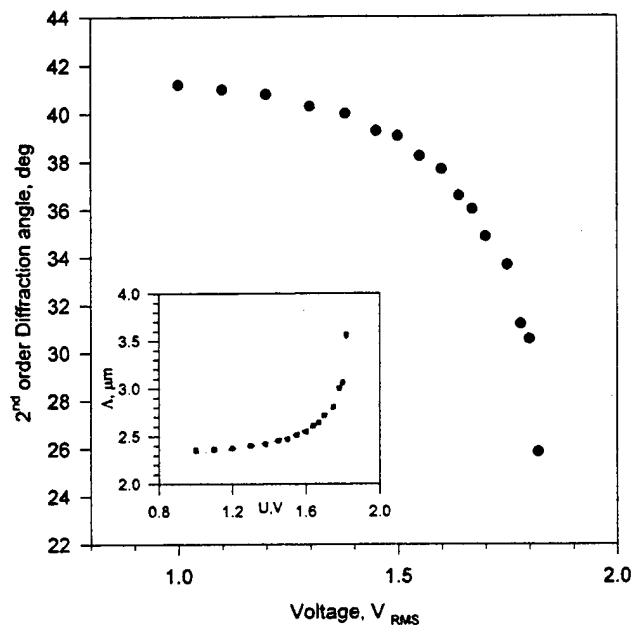


FIGURE 4.20. Direction of the 2nd diffraction maximum and the grating period Λ (calculated from Eqn.(4.1)) as the function of the applied voltage.

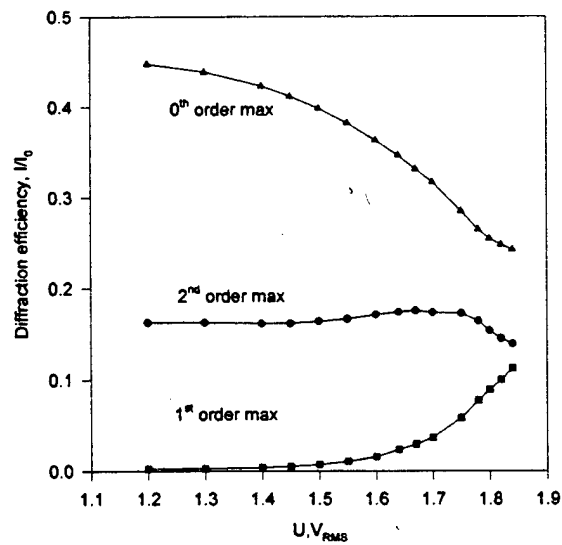


FIGURE 4.21. Intensities of the 0th, 1st and 2nd order diffraction maxima as the functions of the applied voltage.

It should be noted that change of the grating period, causing the continuous beam steering effect, appears as a generation and motion of dislocations in the stripe structure. The dislocations are clearly seen in Figure 4.19b. Therefore, we studied the dislocation effect on optical properties of CDG.

Dislocation effect on optical properties of CDG

Studies of light scattering on dislocations in cholesteric stripe textures are important due to two reasons. The first one is that dislocations are generated during structural transformations and remain rather long time (their life times is much longer than characteristic response times; see, for example, Figure 4.19b). The second reason is that scattering properties of such dislocations are not obvious a priori. On the one hand, the core of dislocation is smooth as a light scatterer. Figure 4.22 shows the structure of possible dislocations in ideal cholesteric structure. Such structure is realized in the middle of cholesteric cell with planar anchoring for stripes that are parallel to the rub direction (Figure 4.3c). On the other hand, the dislocations produce phase mismatch between stripes at the left and right sides (Figure 4.22), and this mismatch can be a source of additional scattering.

Diffraction on dislocations was simulated with a computer-generated hologram⁷⁸. This hologram is an amplitude grating containing a dislocation of Burger's vector b ($b = sa$, where the integer s is the dislocation strength, a is the grating periodicity). The dislocation effect show up as spots of zero light intensity in the diffraction maxima of light passed through the hologram. The number of spots in each diffraction maximum is given by: $n = ms$, m is the diffraction order ($m = 0, \pm 1, \pm 2, \dots$). For $s = 1$, there is one spot in each $+1$ and -1 diffraction maximum and two spots in each diffraction maximum $+2$ and -2 (Figure 4.23). Our system is similar to anisotropic phase hologram, so diffraction pattern could differ.

The geometry of the experiment is shown in Figure 4.23. A Gaussian beam from He-Ne laser 1 ($\lambda = 632$ nm, beam diameter 1.2 mm, linearly polarized along the stripes, radiation power < 1 mW) was incident on the LC cell 2 with the stripe pattern. The cell was put into the waist of the beam. To maintain stripes A.C. voltage from a wavefront generator was applied to the cell. We put a removable microscope (not shown) focused on the stripes from the opposite side of the cell to control what part of the pattern is being illuminated. By scanning the stripe pattern in the XY plane we could find either a dislocation-free, homogeneous stripes or stripes containing an isolated dislocation.

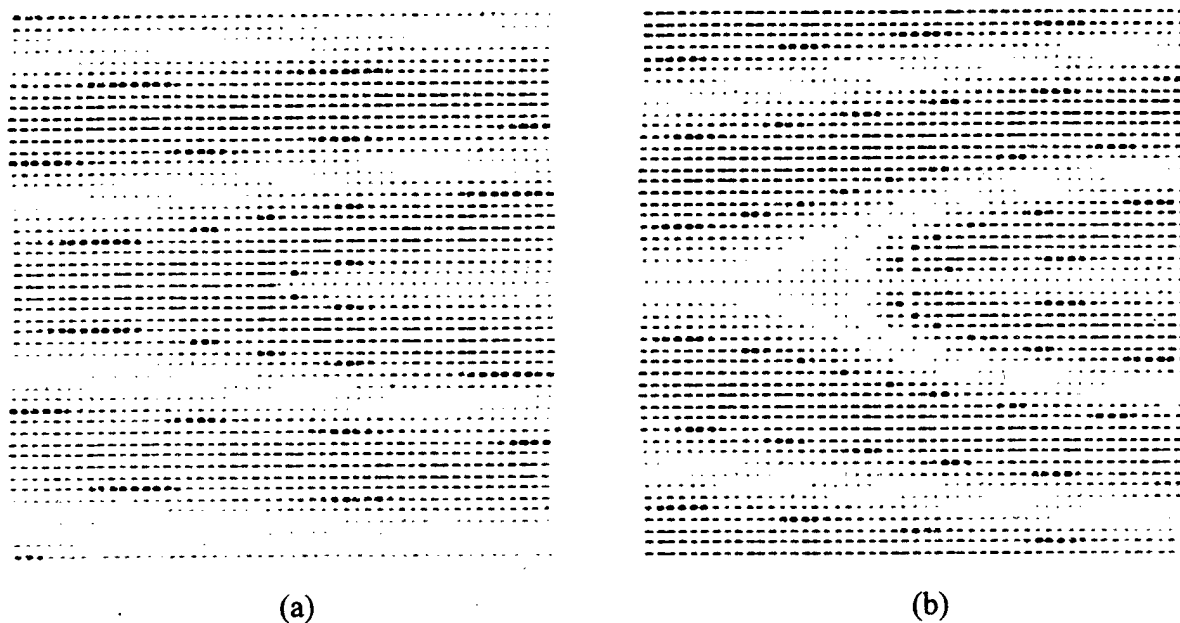


FIGURE 4.22. A cut of the edge dislocations with different strengths made parallel to the XY-plane. (a) $s=1$, (b) $s=2$.

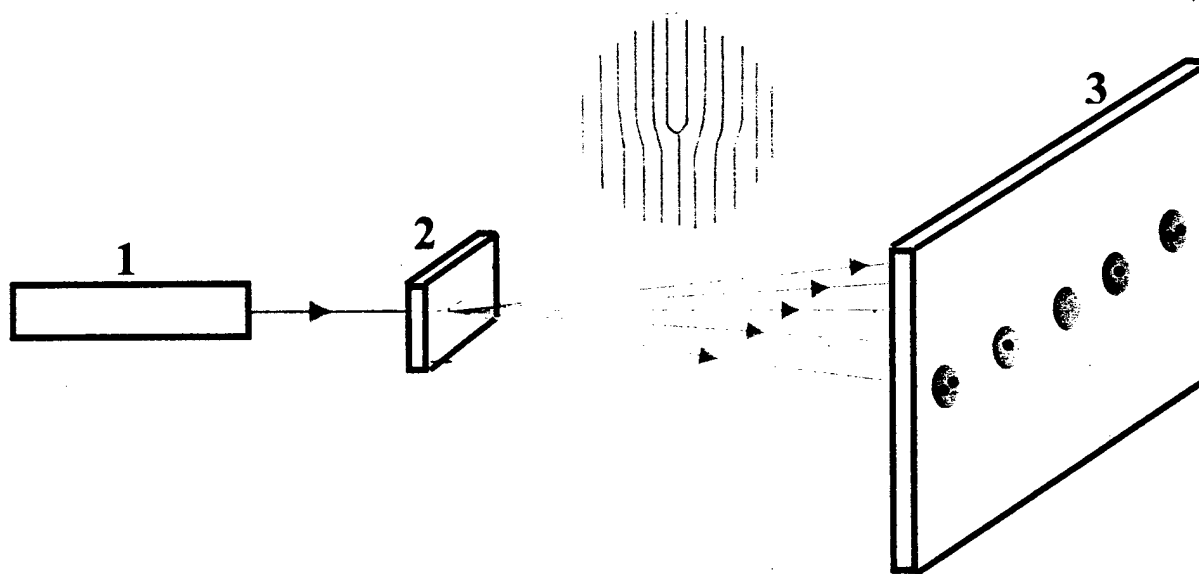


FIGURE 4.23. Geometry of the experiment for diffraction on a dislocation.

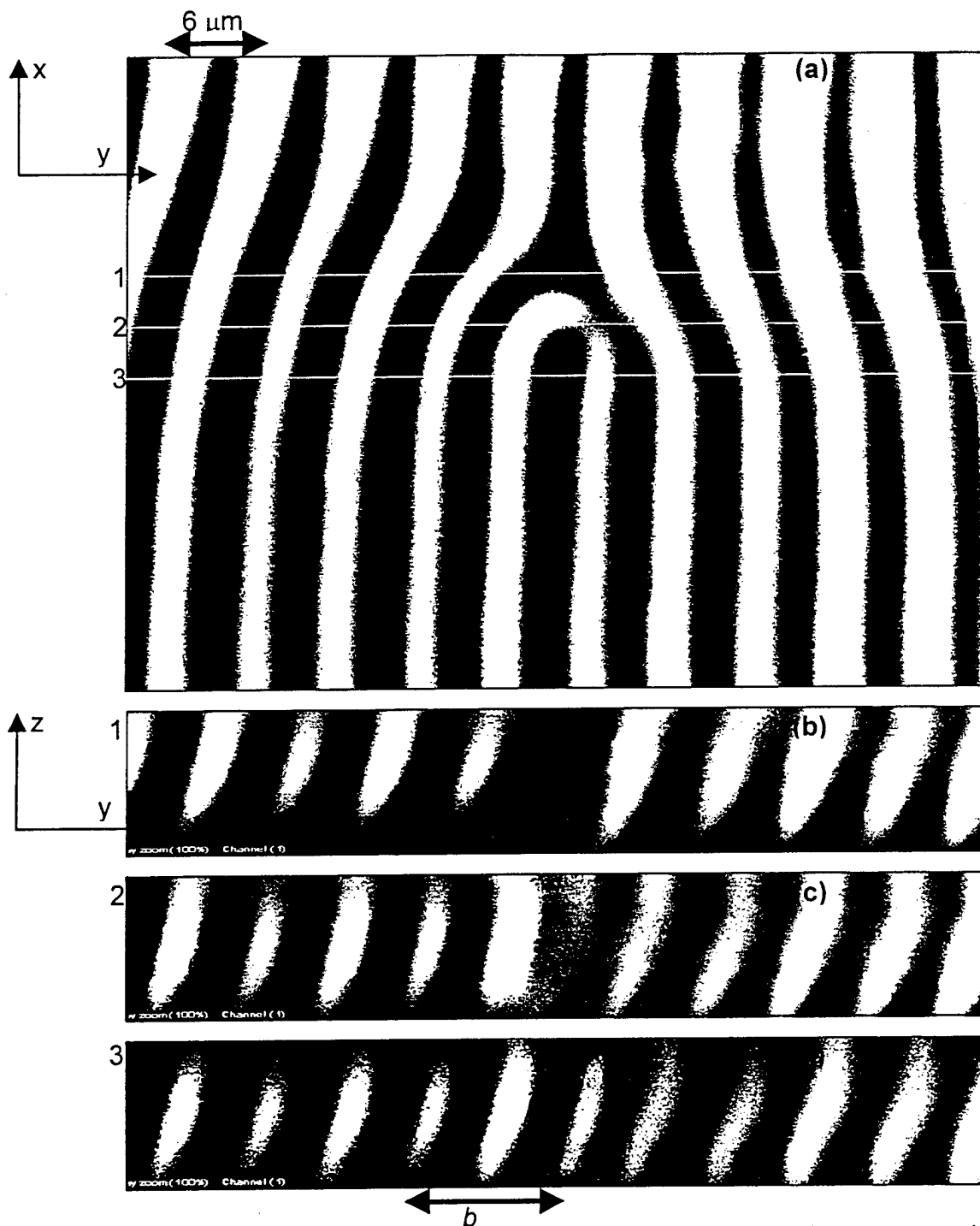


FIGURE 4.24. Fluorescent confocal scanning microscope images of the cholesteric stripe texture containing an isolated edge dislocation. (a) in the plane of the cell; (b)-(d) perpendicular to the plane of the cell; the cuts along the lines 1, 2, 3 are made parallel to z -axis. The apparent periodicity in (a) is two times smaller than the true periodicity b .

Confocal fluorescent scanning microscopy was used to study the details of the dislocation structure (Figure 4.24). Figure 4.24, b-d are cross-sections of the cell made along the lines 1, 2, 3 perpendicular to the cell plane. The cross-section examination reveals that odd and even stripes have different heights. Therefore, the periodicity is a two-stripe

section examination reveals that odd and even stripes have different heights. Therefore, the periodicity is a two-stripe distance (b on Figure 4.24.d) which corresponds to a 2π -turn of the director along the y -axis. This is also confirmed both by computer simulations of 3-D molecular distributions in cholesteric stripes and by diffraction studies. The Burger's vector of the dislocation is p and the strength is $s = 1$ ($b = p \cdot 1$).

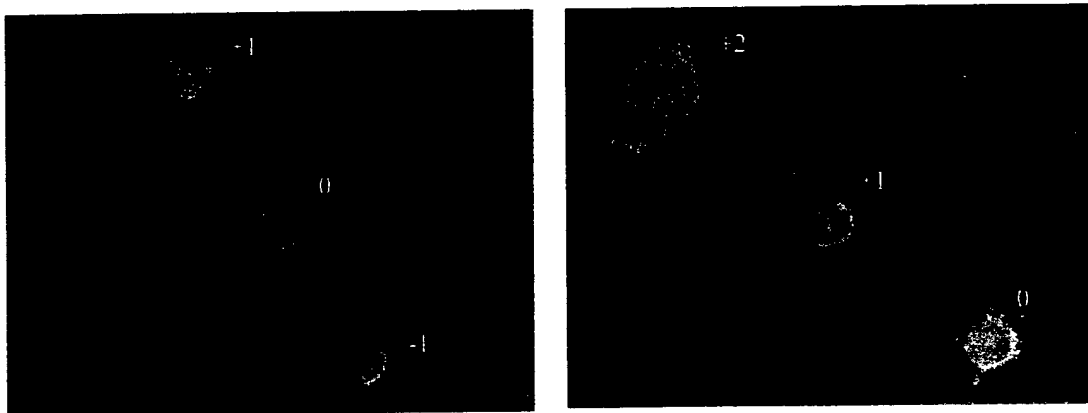


FIGURE 4.25. Diffraction pattern in the far-field zone. (a) $-1, 0, +1$ diffraction orders; (b) $0, +1, +2$ diffraction orders.

Diffraction pattern from the dislocation is shown in Figure 4.25. The number of spots in each diffraction maximum is the same as for amplitude holograms. The dislocation strength $s = 1$, and there is one spot in each $+1$ and -1 diffraction maximum and two spots in each diffraction maximum $+2$ and -2 (Figure 4.25). The number of spots in diffraction maxima is caused by topological character of singularity in the wavefront and does not depend on the structure of dislocation and its optical properties, which affect on the size and position of spots. It should be noted that dark spots are the only effect caused by an isolated dislocation produces on diffraction maxima, but the large number of dislocations should be avoided in CDG as they bring in a substantial distortion to the diffraction pattern.

Diffraction gratings in ferroelectric SmC* cells

Ferroelectric chiral smectic C (SmC*) liquid crystals are promising materials for applications in fast electrooptic devices. Extensive studies during the last two decades advanced the understanding of rather complex structures formed in the so-called surface-stabilized SmC* cells. The idea of surface stabilization is to unwind the helicoidal SmC* structure. It can be achieved when the cell thickness d is smaller than the helicoidal pitch p ⁷⁹. Normally, the preparation of an aligned SmC* slab starts with a homogeneously aligned smectic A (SmA) texture at elevated temperatures. The SmA layers are oriented normally to the glass plates that bound the cell. Upon cooling down to the SmC* phase, this 'bookshelf' structure gets distorted: the smectic layers tilt in the vertical plane and most often form a wall defect - 'chevron'²². At the tip of the chevron, the layers reverse their tilt. Chevrons are explained as the result of layer contraction compensated by the layer's tilt.

We explored the possibility of creating diffracting gratings in ferroelectric SmC* cells⁸⁰. We have found a new type of a fine modulated (stripe) structure that occurs at temperatures well below the SmA-SmC* transition point without any applied or pre-applied electric field, Figure 4.26. The periodicity of modulations is much smaller than d . Low applied voltage changes both the periodicity and orientation of stripes, which allows for electric-field control of optical diffraction at the stripes.

We used the SmC* mixture Felix-015/100 (Hoechst, Germany) with the phase sequence: X-12°C-SmC*-72°C-SmA-83°C-N*-86°C-I and the following parameters at 25°C (reported by the manufacturer): spontaneous polarization $P_s = 33 \text{ nC/cm}^2$, molecular cone angle $2\theta = 51^\circ$ (as measured by applying a strong DC electric field to a planar cell), effective cone angle $2\theta_{eff} = 26.5^\circ$ (as measured optically by using two memory states in a 2- μm cell with no electric field applied). The helical pitch in the cholesteric N* phase at 83°C is larger than 100 μm .

Cooling to the deep SmC* phase ($\approx 35^\circ\text{C}$, which is about 40°C below the SmA-SmC* transition) results in a modulated stripe structure, Figure 4.26. The stripes appear if $d \geq 10 \mu\text{m}$; no external electric field is involved. Their period Λ increases with d , remaining noticeably smaller than d , Figure 4.27.

The most striking feature of stripes is that their periodicity and orientation strongly depend on the applied voltage, Figure 4.28. Since optical properties of the stripe textures are modulated, we used optical diffraction to study the field effects, as described below for the uniform state.

Polarized He-Ne laser beam is normal to the cell. The plane of diffraction is normal to the stripes, Figure 4.28. Diffraction pattern reveals a clear pair of ± 1 st order diffraction maxima and a weak ± 2 nd order diffraction maxima. To measure the time response and diffractive efficiency of the grating, we set the photodetector at the position of the (-1)st maximum. The time of switching of stripe orientation depends on the applied voltage; the upper limit is about 0.2 sec. The measurements were performed at a larger time scale to test the equilibrium states. Diffraction efficiency is weak, 1%-2%.

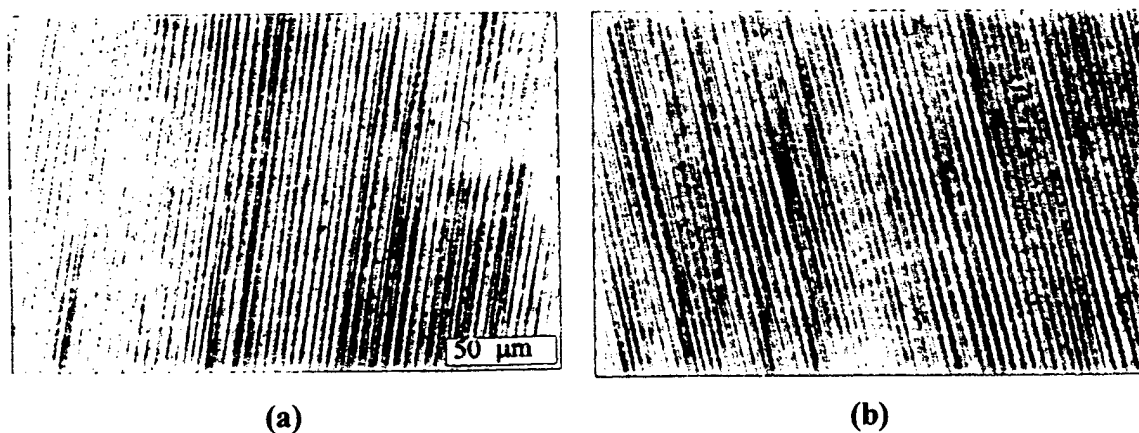


Figure 4.26. Modulated structure in a SmC* cell of thickness $21 \mu\text{m}$ at 22°C . DuPont 2555 coating, antiparallel rubbing. The stripes have different periodicity and orientation for different voltages applied to the cell: $U = 0V$ (a) and $U = 0.6V$ (b).

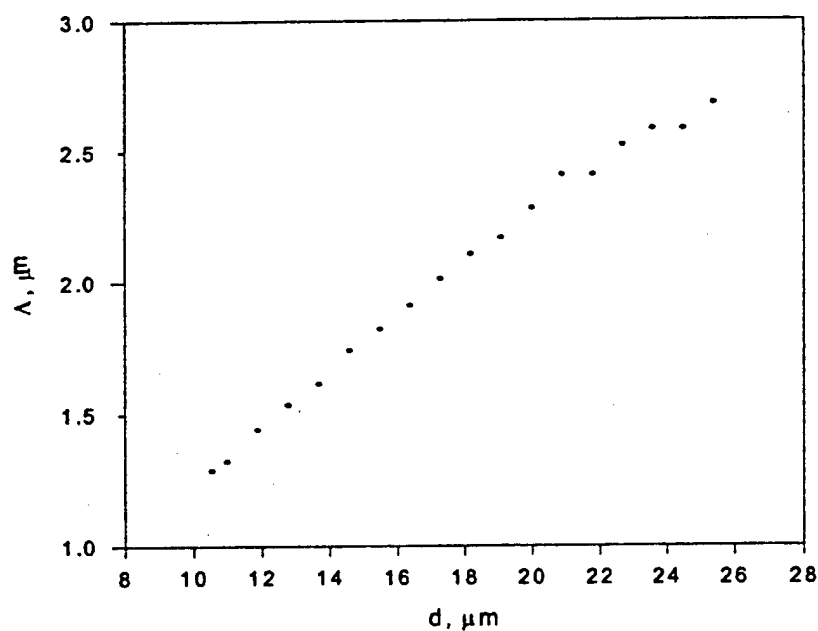


Figure 4.27. Modulation wavelength Λ as the function of the cell thickness d (PVA coating) at 22°C .

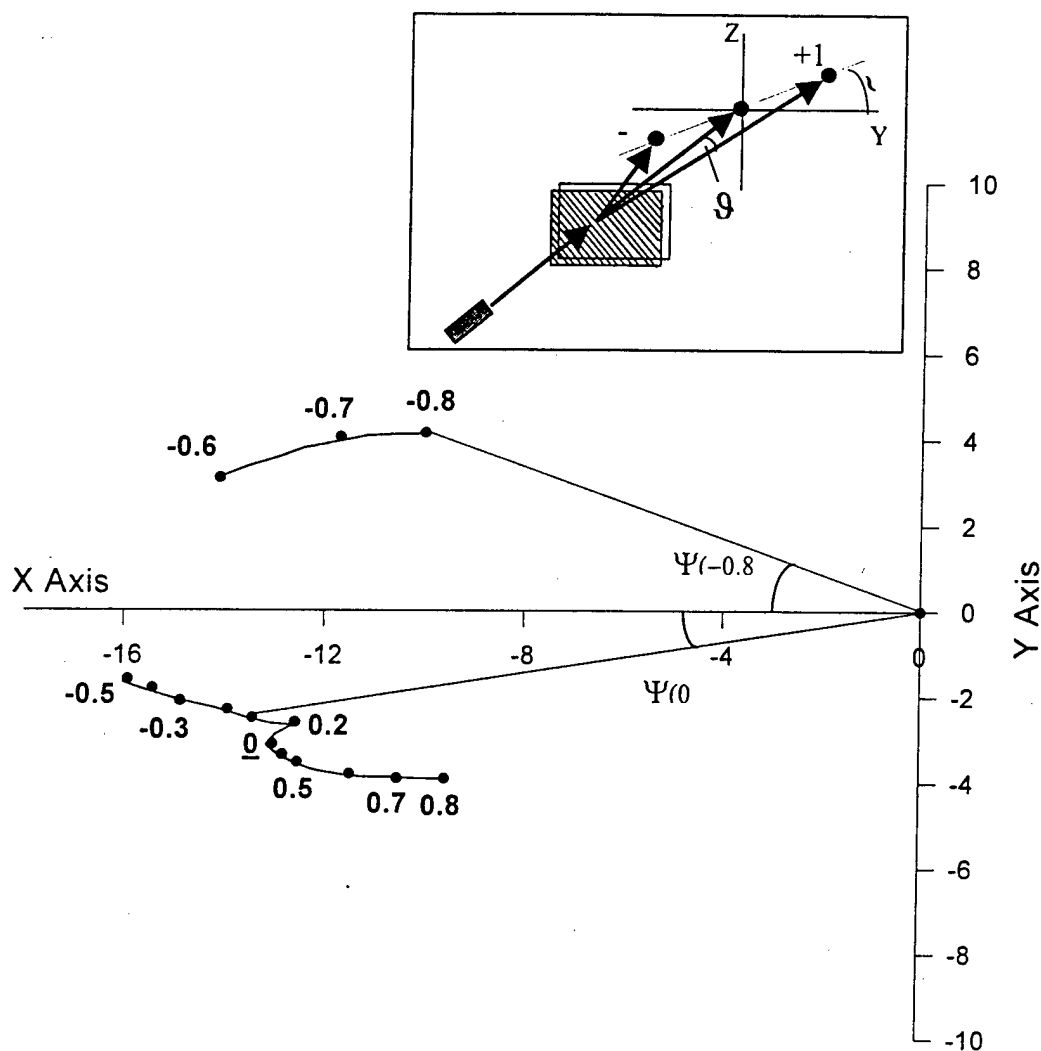


Figure 28. Position of the (-1) -st diffraction maximum as the function of the applied voltage (0.2 Hz square wave signal); $d = 21\mu\text{m}$, PVA coating. The inset shows the optical setup. Z axis is parallel and Y -axis is normal to the rub direction; both axes are in the plane of the cell.

Bragg diffraction

Bragg diffraction is observed in cells with $d/p > 2$ and $p < 1\mu\text{m}$. With fixed $\lambda = 633\text{nm}$, the intensity of the diffracted beam depends on the angle of incidence and reaches a maximum when the incident angle is equal to the Bragg angle, Eq.(2). The strongest second order diffraction maximum corresponds to the bulk periodicity related to the half-pitch of the cholesteric helix. The corresponding diffraction angle Θ_2 changes with U . For example, $\Theta_2 = 35.5^\circ$ at $U = 3.15V_{RMS}$, $\Theta_2 = 41^\circ$ at $U = 2.67V_{RMS}$, and $\Theta_2 = 48.8^\circ$ at $U = 1.9V_{RMS}$. In other words, for each value of U , the incident angle should be adjusted to satisfy the Bragg condition. The maximum efficiency of diffraction (calculated with respect to the incident light intensity) is ≈ 0.3 and does not change significantly with U .

Certainly, the necessity to adjust the beam incident angle does not suit for applications, but discrepancy from the Bragg condition is not so crucial the diffraction efficiency. Thus, the oblique beam with constant incident angle can be used for the cells with electrically-controlled periodicity. On the other hand, the oblique beam allows to suppress other diffraction orders, Figure 4.29.

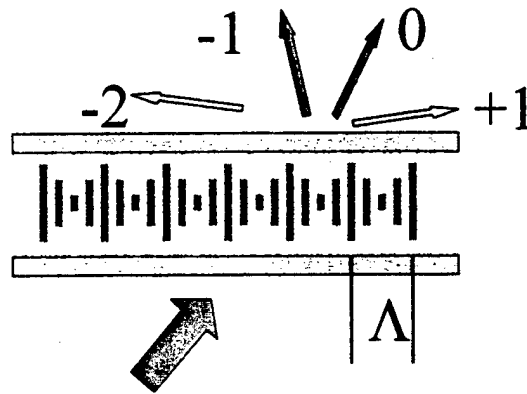


FIGURE 4.29. Suppression of other diffraction orders for the oblique beam.

4.5 Conclusion - Cholesteric Diffraction Gratings

- We have developed the electrically-controlled cholesteric diffraction gratings (CDG), based on the in-plane periodic structures in liquid-crystalline cells with non-patterned transparent electrodes. These periodic structures appear under certain conditions as a result of simultaneous action of dielectric reorientation and surface anchoring.
- CDG is a phase grating capable of both Bragg and Raman-Nath diffraction and two modes of operation:
 - (1) simple electric switching between non-diffractive and diffractive regimes with corresponding digital deflection of the laser beam;
 - (2) continuous electric-field-controlled periodicity of the grating allows one to steer the beam continuously; the device has no mechanically moving elements.

The regime of diffraction and the operational mode of the cholesteric diffractive device can be selected by adjusting the cell thickness and the cholesteric pitch.

- We have found two different scenarios to form a one-dimensionally modulated director configuration in the plane of a cholesteric cell. The first scenario is a first-order nucleation process with subsequent elongation of 'stripes'. The second process is a continuous (second-order) undulation-like instability in which the whole area of the cholesteric cell becomes modulated when the voltage is high enough to tilt the quasi-nematic layers away from their original horizontal orientation. The second process is faster than the first one since there is no energy barrier.

- The following characteristics have been achieved for CDGs:

(1) Steering angle:

electrical switching:

up to 90 degrees for Bragg diffraction;

up to 40 degrees for Raman-Nath diffraction;

continuous beam steering ~ 20 degrees.

(2) Diffraction efficiency:

~10 % for Raman-Nath diffraction, as measured for one out of two symmetric diffraction maxima;

~30 % for Bragg diffraction;

(3) Response time:

electrical switching: 'on' ~ 20-40 ms, 'off' ~ 5-40 ms;

continuous beam steering ~100 ms for 1 cycle of steering by 10 degrees.

- We found that the real-space dislocations that control the spacing changes in the cholesteric gratings cause optical vortices, i.e., singularities of the wavefront. The effect is of fundamental interest and, as far as we know, is the first example of the optical vortices created by liquid crystal phase gratings. The optical vortices mark the diffraction maxima with small spots of zero intensity. The effect does not seriously influence the diffraction efficiency since the area of the spot is small.
- We have found a new modulated structure in ferroelectric chiral smectic C liquid crystals that can serve as diffraction gratings in which the periodicity and direction of modulations can be controlled by a small applied voltage. The drawback of these devices (as compared to the CDGs) is small diffraction efficiency (1-2%) and slow response (up to 200 msec).
- We have found that the photopolymerization in the fingerprint structures of cholesteric diffraction gratings can lead to spatial separation with modulated polymer density. The effect will be further explored since it promises to increase the ruggedness of the gratings, to allow light-weight plastic devices and to reduce the response times.

Appendix A. Mathematical Basis for Computer Simulations

The equilibrium director field is found by minimizing free energy functional, which is a sum of the Frank-Oseen bulk energy and the surface anchoring energy. Usually LC's with large dielectric anisotropy are used in experiments and the inhomogeneity of electric field may be significant even in the case with homogeneous plane electrodes. Therefore, we find electric potential $V(\mathbf{r})$ self-consistently. The Frank-Oseen functional of director distortion in the external field is calculated taking into account the divergence K_{24} elastic constant⁷:

$$F_{FO} = \int \left[\frac{K_{11}}{2} (\text{div } \mathbf{n})^2 + \frac{K_{22}}{2} (\mathbf{n} \text{curl } \mathbf{n} - q)^2 + \frac{K_{33}}{2} [\mathbf{n} \times \text{curl } \mathbf{n}]^2 - \right. \\ \left. - K_{24} \text{div}(\mathbf{n} \text{div } \mathbf{n} + \mathbf{n} \times \text{curl } \mathbf{n}) - \frac{\epsilon_0}{2} (\nabla V \cdot \hat{\epsilon} \cdot \nabla V) \right] d^3 \mathbf{r}, \quad (\text{A.1})$$

where K_{11} (K_{22} , K_{33}) is the splay (twist, bend) elastic constant, $\hat{\epsilon}$ is the relative dielectric tensor with components dependent on the director orientation:

$$\epsilon_{ij} = \epsilon_{\perp} \delta_{ij} + \epsilon_a n_i n_j. \quad (\text{A.2})$$

Variation of F_{FO} with respect to the potential V inside a cell gives the Maxwell equation:

$$\frac{\delta F_{FO}}{\delta V} = \text{div}(\epsilon_0 \hat{\epsilon} \nabla V) = 0. \quad (\text{A.3})$$

The surface anchoring energy is calculated in the generalized Rapini-Papoular approximation

$$F_s = -\frac{1}{2} \int W_{ij} n_i n_j dS, \quad (\text{A.4})$$

where W_{ij} is the symmetrical anchoring tensor, that describes the pretilt angle as well as polar and azimuthal anchoring coefficients.

We study periodic in-plane structures. Therefore, we simulate one unit cell in x and y directions, that are parallel to the cell, with periodic boundary conditions²⁷:

$$\mathbf{n}(\mathbf{r}) = \mathbf{n}(\mathbf{r} + \Lambda_x \mathbf{i}) = \mathbf{n}(\mathbf{r} + \Lambda_y \mathbf{j}). \quad (\text{A.5})$$

The discretized free energy $f = \frac{F_{FO} + F_s}{\Lambda_x \Lambda_y}$ per unit area (derivatives in each rectangular unit are substituted by

corresponding differences between opposite faces of this unit) should have minimum with respect to \mathbf{n} and maximum with respect to V . Therefore the relaxation to the equilibrium state is provided by the following 'motion' equations:

$$\gamma \frac{d\mathbf{n}_{\{m\}}}{dt} = - \frac{\delta f}{\delta \mathbf{n}_{\{m\}}}, \quad (\text{A.6a})$$

$$\eta \frac{dV_{\{m\}}}{dt} = \frac{\delta f}{\delta V_{\{m\}}}, \quad (\text{A.6b})$$

where the phenomenological viscosities γ and η are being adjusted during the calculation for the fastest convergence.

The free energy f per unit area of the cell reads as the quadratic form

$$f = f_0 + \sum_{\alpha=x,y} f_{\alpha} q_{\alpha} + \sum_{\alpha=x,y} f_{\alpha\beta} q_{\alpha} q_{\beta}, \quad (\text{A.7})$$

where $q_{x,y} = 1/\Lambda_{x,y}$, f_{α} and $f_{\alpha\beta}$ are coefficients independent on q_{α} , so the minimum of f with respect to q_x and q_y is easily calculated after each step. This convergent process allows us to find both the free energy minimum and the periodicity of equilibrium state (Λ_x and Λ_y) simultaneously.

REFERENCES

1. J. A. Thomas, Y. Fainman; Optical Cascade Operation of Optical Phased-Array Beam Deflectors; *Applied Optics*; 37; pp. 6196-6212; 1998.
2. O. Solgaard, F. Sandejas, D. Bloom; Deformable Grating Optical Modulator; *Optics Letters*; 17; pp. 688-690; 1992.
3. R. Fuchs, et. al; Novel Beam Steering Micromirror Device; *Proc. SPIE*; 3513; pp. 40-49; 1998.
4. P. F. McManamon, T. A. Dorschner, D. L. Corkum, L. J. Friedman, D. S. Hobbs, M. Holz, S. Lieberman, H. Q. Nguyen, D. P. Resler, R. C. Sharp, and E. A. Watson; Optical Phased Array Technology; *Proc. of the IEEE*; 84; pp.268-297; 1996.
5. R. M. Matic; Blazed phase liquid crystal beam steering; *Proc. of SPIE*; 2120; pp.194-205; 1994.
6. D. Subacius, S. Shiyankovskii, O. D. Lavrentovich, P. Bos, Cholesteric Gratings with Field-Controlled Period; *Appl. Phys. Lett.*; 71; pp. 3323-3325; 1997.
7. D. Subacius, P. Bos, O. D. Lavrentovich; Switchable Diffractive Cholesteric Gratings; *Appl. Phys. Lett.*; 71; pp. 1350-1352; 1997.
8. W. Kulcke, T. J. Harris, K. Kosanke, E. Max; A Fast, Digital-Indexed Deflector; *IBM J. Res. Dev.*; 8; pp. 64-67; 1964.
9. T. J. Nelson; Digital Light Deflection; *Bell Syst. Tech. J.*; 43; 3, pp. 821-845; 1964.
10. U. J. Schmidt; A High Speed Digital Light Beam Deflector; *Phys. Lett.*; 12; 3; pp. 205-206; 1964.
11. W. Kulcke, K. Kosanke, E. Max; H. Fleisher, T. J. Harris; Convergent Beam Digital-Indexed Deflector; *Optical and Electro-optical Information Processing*; ch. 23; -MIT Press; Cambridge, MA; 1965.
12. W. J. Tabor; The Use of Wollaston Prisms for a High-Capacity Digital Light Deflector; *Bell System Technical Journal*; pp. 43; 1153-1154; 1964.
13. R. A. Soref, D. H. McMahon; Optical Design of Wollaston Prism Digital Light Deflectors; *Applied Optics*; 3; pp. 425-434; 1966.
14. W. J. Tabor; A High-Capacity Digital Light Deflector Using Wollaston Prisms; *Bell System Technical Journal*; 46; pp. 957-990; 1967.
15. U. J. Schmidt; A High Speed Digital Light Beam Deflector; *Physics Letters*; 12; 3; pp. 205-206; 1964.
16. G. Hepner; Digital Light Deflector with Prisms and Polarization Switch Based on the Pockels Effect with Transverse Field; *IEEE J. Quant. Elec.*; 8; pp. 169-173; 1972.
17. H. Meyer, D. Riekman, K. P. Schmidt, U. J. Schmidt, M. Rahlff, E. Schroder, W. Thust; Design and Performance of a 20-Stage Digital Light Beam Deflector; *Applied Optics*; 11; pp. 1732-1736; 1972.

18. U. J. Schmidt, E. Schroder, W. Thust; Optimization Procedures for Digital Light Beam Deflectors; *Applied Optics*; 12; pp. 460-465; 1973.
19. R. McRuer, L. R. McAdams, J. W. Goodman; Ferroelectric liquid-crystal digital scanner; *Optics Letters*; 15,23, pp. 1415-1417, 1990.
20. L. R. McAdams; *Photonic Switching with Liquid Crystal*; PhD dissertation; Stanford Univ.; 1991.
21. R. N. McRuer; *Ferroelectric liquid crystal optical switching networks*; PhD dissertation; Stanford Univ.; 1991.
22. P. G. de Gennes, J. Prost; *The Physics of Liquid Crystals*; 2nd ed; p. 142; Oxford Univ. Press; New York; 1993.
23. D. J. Broer, G. N. Mol; "In-situ photopolymerization of oriented liquid-crystalline acrylates"; *Makromol. Chem.*; 192; pp. 59-74; 1991.
24. B. Malraison, Y. Poggi, E. Guyon; Nematic liquid crystals in high magnetic field: Quenching of the transverse fluctuations; *Phys Rev A*; 21, 3; pp. 1012-1024; 1980.
25. D. A. Dunmur, T. F. Waterworth, P. Palffy-Muhoray; Electric Field Induced Birefringence in Nematic Liquid Crystal Films: Evidence for Wall Quenching of Director Fluctuations; *Mol Cryst Liq Cryst*; 124; pp. 73-88; 1985.
26. S. Chandrasekhar; *Liquid Crystals*, 2nd ed., p. 227; Cambridge Univ. Press; New York; 1992.
27. Y. Ouichi, Y. Takanishi, H. Takezoe, and A. Fukuda; Chevron Layer Structure in Smectic A Phase of 8CB; *Jpn J Appl Phys.*; 28; pp.L487-489; 1989.
28. Y. Ouichi, Y. Takanishi, H. Takezoe, and A. Fukuda; Chevron Layer Structure and Parabolic Focal Conics in Smectic A Liquid Crystals; *Jpn. J. Appl. Phys. Part I*; 28; pp.2547-51; 1989.
29. R. Crandall, *Topics in Advanced Scientific Computation*, Springer-Verlag, New York, 1996.
30. W. H. Press, et. al.; *Numerical Recipes in C*; 2nd Edition; Cambridge Univ. Press; New York; 1995.
31. V. Dominic, A. Carney, E. Watson; Measurement and Modeling of the Angular Dispersion in Liquid Crystal Broadband Beam Steering Devices; *Opt. Eng.*; 35; pp. 3371-3379; 1996.
32. L. J. Friedman, et. al.; Spatially Resolved Phase Imaging of a Programmable Liquid-Crystal Grating; *Appl. Opt.*; 35; pp. 6236-6240; 1996.
33. S. Dickmann, J. Eschler, O. Cossalter, D. Mlynski; Simulation of LCDs Including Elastic Anisotropy and Inhomogeneous Fields; *SID 93 Digest*; pp. 638-641; 1993.
34. A. Lien; Extended Jones Matrix Representation for the Twisted Nematic Liquid-Crystal Display at Oblique Incidence; *Appl. Phys. Lett.*; 57, p.2767; 1990.
35. D. W. Berreman; Optics in Stratified and Anisotropic Media: 4 X 4 Matrix Formulation; *J. Opt. Soc. Am.*; 62; p.502; 1972.

36. K. S. Yee; Numerical Solution of Initial Boundary Value Problems Involving Maxwell's Equations in Isotropic Media; IEEE Trans Ant. Prop.; 14; 3; pp.302-307; 1966.
37. B. Witzigmann, P. Regli, W. Fichtner; Rigorous Electromagnetic Simulation of Liquid Crystal Displays; J. Opt. Soc. Am. A; 15; p.753; 1998.
38. A. Taflove; *Computational Electrodynamics, The Finite-Difference Time-Domain Method*; Artech House; Boston; 1995.
39. J. Schneider, S. Hudson: The Finite-Difference Time-Domain Method Applied to Anisotropic Material; IEEE Trans. Ant. & Prop.; 14; pp. 994-999; 1993.
40. R. Guenther; *Modern Optics*; John Wiley & Sons; New York; 1990.
41. G. Mur; Absorbing Boundary Conditions for the Finite-Difference Approximation of the Time-Domain Electromagnetic-Field Equations; IEEE Trans. Elec. Comp.; 23; pp. 377-382; 1981.
42. J-P. Berenger; A Perfectly Matched Layer for the Absorption of Electromagnetic Waves; J. Comp. Phys.; 114; p.185; 1994.
43. C. M. Titus, P. J. Bos, J. R. Kelly, E. C. Gartland; Comparison of Analytical Calculations to Finite-Difference Time-Domain Simulations of One-Dimensional Spatially Varying Anisotropic Liquid Crystal Structures; Jap. J. Appl. Phys.; Part 1; 38; p.1488; 1999.
44. I. Kim, W. Hoefer; Effect of the Stability Factor on the Accuracy of Two-Dimensional TD-FD Simulation; 1989 IEEE AP-S Symp. Digest; pp. 1108-1111; 1989.
45. I. Kim, W. Hoefer; Numerical Dispersion Characteristics and Stability Factor for the TD-FD Method; Elect. Lett.; 26; pp. 485-486; 1990.
46. A. Taflove; *Advances in Computational Electrodynamics*; Artech House; Boston; 1998.
47. C. H. Gooch, H. A. Tarry; The optical properties of twisted nematic liquid crystal structures with twist angles $\leq 90^\circ$; J. Phys. D; 8; pp. 1575-1584; 1975.
48. H. Wohler and M. Becker; The Optics of Liquid Crystals; Seminar Lecture Notes; The 13th International Display Research Conference; Strasbourg, France; August 31, 1993.
49. B. Baker, E. Copson; *The Mathematical Theory of Huygens' Principle*; 2nd ed.; Oxford Univ. Press; London; 1950.
50. C. Bouwkamp; Diffraction Theory; Rep. Prog. Phys.; 17; pp. 35-100; 1954.
51. M. Born, E. Wolf; *Principles of Optics*; 6th Edition; Cambridge University Press; Cambridge; 1997.
52. J. W. Goodman; *Introduction to Fourier Optics*; McGraw-Hill; New York; 1968.
53. P. Clemmow; The Plane Wave Spectrum Representation of Electromagnetic Fields; Pergamon Press; London; 1966.

54. J. A. Stratton; *Electromagnetic Theory*; 1st Edition; McGraw-Hill; New York; 1941.
55. S. Schelkunoff; Some Equivalence Theorems of Electromagnetics and Their Application to Radiation Problems; *Bell Sys. Tech. J.*; 15; pp. 92-112; 1936.
56. J. D. Jackson; *Classical Electrodynamics*; Wiley; New York; 1962.
57. M. Kowarz; Diffraction Effects in the Near Field; PhD Thesis; University of Rochester; 1995.
58. M. Totzeck; Validity of the Scalar Kirchhoff and Rayleigh-Sommerfeld Diffraction Theories in the Near Field of Small Phase Objects; *J. Opt. Soc. Am. A*; 8; pp. 27-32; 1991.
59. M. Totzeck; Test of Various Diffraction Theories in the Near Field of Phase Objects; *Ultramicroscopy*; 57; pp. 160-164; 1995.
60. P. M. Morse, P. J. Rubenstein; The Diffraction of Waves by Ribbons and Slits; *Phys. Rev.*; 54; pp. 895-898; 1938.
61. A. Sommerfeld, *Lectures on Theoretical Physics*; Volume VI; Academic Press; New York; 1954.
62. C. M. Titus, P. J. Bos, J. R. Kelly; Two-Dimensional Optical Simulation Tool for Use in Microdisplay Analysis; *SID 99 Digest*; pp.624-627; 1999.
63. K.M. Johnson, D.J. McKnight, and I. Underwood, *IEEE J. Quant. Electron.* **29**, 699 (1993).
64. J. Chen, P. J. Bos, H. Vithana, and D. L. Johnson, "An electro-optically controlled liquid crystal diffraction grating", *Appl. Phys. Lett.* **67**(18), 2588-2590 (1995).
65. D.P. Resler, D.S. Hobbs, R.C. Sharp, L.J. Friedman, and T.A. Dorschner, *Opt. Lett.* **21**, 689 (1996).
66. Zh. He, T. Nose, S. Sato, "Polarization properties of an amplitude nematic liquid crystal grating", *Opt. Eng.* **37**(11), 2885-2898 (1998).
67. J. E. Stockley, D. Subacius, S. A. Serati, "The influence of the inter-pixel region in liquid crystal diffraction gratings", *Proceedings of SPIE* 3635, 127-136 (1999).
68. S. V. Shiyankovskii, D. Subacius, D. Voloschenko, Ph. Bos, and O. D. Lavrentovich, "Cholesteric diffraction devices with a field-controlled grating vector", *Proceedings of SPIE* 3475, 56-64 (1998).
69. O.D. Lavrentovich, S.V. Shiyankovskii, and D. Voloschenko, "Fast Beam Steering Cholesteric Diffractive Devices", *Proceedings of SPIE*, vol. 3787 Optical Scanning: Design and Application, 21-22 July 1999, p. 149-155 (1999)
70. Yu.A.Nastyshyn, R.D.Polak, S.V.Shiyanovskii, and O.D.Lavrentovich. "Determination of the nematic polar anchoring from retardation vs. voltage measurements", *Appl. Phys. Lett.* **75**(2), pp.202-204 (1999).
71. S.V. Shiyankovskii and O.D. Lavrentovich; 3D Computer Simulations of Nematic and Cholesteric Cells, *SID International Symposium, Digest of Technical Papers*, May, 1998, p.826-829.
72. O.D. Lavrentovich and D.-K. Yang, Cholesteric Cellular Patterns with Electric-Field-Controlled Line Tension, *Phys. Rev. E (Rapid Communication)*, **57**, R6269 (1998).

73. S.A. Pikin, *Structural Transformations in Liquid Crystals*, Gordon & Breach, NY, 1991, pp.175-193.
74. Yoan Kim and Jim Franci and Bahman Taheri and John L. West "A Method for the Formation of Polymer Walls in Liquid Crystal/Polymer Mixtures" *Appl. Phys. Lett.* **72** (18) pp. 2253-2255 (1998).
75. Volodymyr H. Bodnar and Yoan Kim and Bahman Taheri and John L. West "Formation of Polymer Walls by Phase Separation of LC-Polymer Binary Mixtures in a Nonuniform Electric Field" *Mol. Cryst. Liq. Cryst. Sci. Tech. A* **329** pp. 405-412 (1999).
76. D. Voloschenko and O.D. Lavrentovich, Light-induced director-controlled micro-assembly of dye molecules from a liquid crystal matrix, *J. Appl. Phys.*, **86**, 4843 (1999).
77. Y. Lansac, M. A. Glaser, N. A. Clark and O. D. Lavrentovich Photocontrolled nanophase segregation in a liquid-crystal solvent, *Nature* **398**, No.6722 (1999).
78. V.Yu.Bazhenov, M.S.Soskin, and M.V.Vasnetsov, *J. Modern Optics*, **39**(5), 985-990. (1990).
79. N.A. Clark and S.T. Lagerwall, S.T., *Appl. Phys. Lett.*, **36**, 899, 1980.
80. D. Subacius, D. Voloschenko, Ph. Bos and O.D. Lavrentovich, Modulated Structures with Field-Controlled Direction and Periodicity in SmC* Liquid Crystals, *Liquid Crystals*, **26**, 295-298 (1999).

Personnel Supported

PI's: Dr. O.D. Lavrentovich(1.5 mo.) and Dr. P.J. Bos (1.5 mo.).

Research Associates: Dr. S.V. Shiyanovskii (30 mo.), D. Subacius(15 mo.) Dr. M. Sabeva (9 mo.)

Graduate Students: C. Titus (25 mo.), D. Voloschenko (6 mo.), R.D. Polak (3 mo.)

Publications

1. D. Subacius, Ph. Bos, and O.D. Lavrentovich; Switchable Diffractive Cholesteric Gratings, *Appl. Phys. Lett.* **71**, 1350 (1997).
2. D. Subacius, S.V. Shiyanovskii, Ph. Bos, and O.D. Lavrentovich; Cholesteric Gratings with Field-Controlled Period, *Appl. Phys. Lett.* **71**, 3323 (1997).
3. O.D. Lavrentovich and D.-K. Yang, Cholesteric Cellular Patterns with Electric-Field-Controlled Line Tension, *Phys. Rev. E (Rapid Communication)* **57**, R6269 (1998).
4. D. Subacius, D. Voloschenko, Ph. Bos and O.D. Lavrentovich, Modulated Structures with Field-Controlled Direction and Periodicity in SmC* Liquid Crystals, *Liquid Crystals*, **26**, 295-298 (1999)
5. Y. Lansac, Matthew A. Glaser, N. A. Clark and O. D. Lavrentovich, Photocontrolled nanophase segregation in a liquid-crystal solvent, *Nature* **398**, No.6722 (1999).
6. D. Voloschenko and O.D. Lavrentovich, Light-induced director-controlled micro-assembly of dye molecules from a liquid crystal matrix, *J. Appl. Phys.*, **86**, 4843 (1999)

7. C. M. Titus, P. J. Bos, J. R. Kelly, E. C. Gartland; "Comparison of Analytical Calculations to Finite-Difference Time-Domain Simulations of One-Dimensional Spatially Varying Anisotropic Liquid Crystal Structures"; Japanese Journal of Applied Physics, Part 1, **38**, p.1488, 1999.

Presentations

1. *Diffractive cholesteric gratings*, D. Subacius, P. Bos, O.D. Lavrentovich, **APS March Meeting**, March 1997, Abstracts, p. 598, code N7-10.
2. *Visualized Instabilities in Cholesteric Stripe Structures*, T. Ishikawa and O.D. Lavrentovich, **APS March Meeting**, March 1997, Abstracts, p. 383, code I16-9
3. *Electric Field Effects and Defects in Layered Liquid Crystals*, O.D. Lavrentovich, D. Subacius, P.J. Bos, and S.V. Shiyankovskii, **The Fourth International Display Workshops**, November 19-21, 1997, Nagoya Congress Center, Nagoya, Japan, Proceedings, LCT1-1 **Invited**, pp. 29-32 (1997)
4. *Oil Streaks in Cholesteric Planar-Focal Conic Transition* O.D. Lavrentovich and D.K. Yang, ALCOM Symposium "Reflective Displays," Cuyahoga Falls, Ohio, December 11-12, 1997, **ALCOM (Advanced Liquid Crystal Optical Materials) Technical Papers**, v. IX, p. 11-21 (1997) (**Invited**).
5. *Computer Simulations of 3D Nematic and Cholesteric Structures* S. V. Shiyankovskii and O.D. Lavrentovich, ALCOM Symposium "Reflective Displays," Cuyahoga Falls, Ohio, December 11-12, 1997, **ALCOM Technical Papers**, v. IX, p. 139-144 (1997)
6. *Cholesteric Diffractive Devices with a Field-Controlled Grating Vector* D. Subacius, S. Li, S. V Shiyankovskii, P. Bos, and O.D. Lavrentovich, ALCOM Symposium "Reflective Displays," Cuyahoga Falls, Ohio, December 11-12, 1997, **ALCOM Technical Papers**, v. IX, p. 183-188 (1997).
7. *Cholesteric Cellular Patterns with Electric-Field Controlled Line Tension*, O.D. Lavrentovich and D.-K. Yang, **The Fifth International Symposium on Ferroic Domains and Mesoscopic Structures**, The Penn State Conference Center, State College, Pennsylvania, April 6-10, 1998, Abstracts (1998) (**Invited**).
8. *3D Computer Simulations of Nematic and Cholesteric Cells*, S.V. Shiyankovskii and O.D. Lavrentovich, SID International Symposium, Digest of Technical Papers, May, 1998, p.826-829.
9. *Optical Wavefront Singularities Generated by Real-Space Singularities in a Cholesteric Liquid Crystal*, D. Voloschenko, O. Lavrentovich, 17th International Liquid Crystal Conference, Strasbourg, France, **Abstract book**, p. P-30, July 19-24, 1998.
10. *Electrically Controlled Liquid Crystalline Diffraction Gratings*, D. Subacius, D. Voloschenko, P.J. Bos, and O.D. Lavrentovich, 17th International Liquid Crystal Conference, Strasbourg, France, **Abstract book**, p. P-127, July 19-24, 1998.
11. *Cholesteric Diffraction Devices with a Field-Controlled Grating Vector*, S.V. Shiyankovskii, D. Subacius, D. Voloschenko, P.J. Bos and O.D. Lavrentovich, International Symposium on Optical Science, Engineering, and Instrumentation, SPIE 43rd Annual Meeting, 19-24 July 1998, San Diego, CA, Conference 3475 Liquid Crystals II, **Proceedings of SPIE**, Vol. 3475, paper 3475-10, 1998. (**Invited**)

12. *Efficient, Accurate Liquid Crystal Digital Light Deflector*, C. M. Titus, P. J. Bos, and O. D. Lavrentovich, Photonics West - Conference on Diffractive/Holographic Technologies, Systems and Spatial Light Modulators VI, January 23-29, 1999, San Jose, CA., **Proceedings of SPIE**, Vol. 3633, Paper 3633-32, 1999.
13. *Two-Dimensional Optical Simulation Tool for Microdisplay Analysis*, C. M. Titus, P. J. Bos, J. R. Kelly, ALCOM Symposium "Reflective Displays," Cuyahoga Falls, Ohio, February 18-19, 1999, **ALCOM Technical Papers**, v. X, p. 127-132, 1999.
14. *Beam Steering Liquid Crystal Devices*, P. Bos, C. Titus, S. Shiyanovskii, D. Voloschenko, and O.D. Lavrentovich, MURI meeting, April 1999, Pasadena, Ca.
15. *Two-Dimensional Optical Simulation Tool for use in Microdisplay Analysis*, C. M. Titus, P. J. Bos, J. R. Kelly, Society for Information Display International Symposium, May 18-20, 1999, San Jose, CA. **SID Digest**, V. XXX, p.624-627, 1999.
16. *Diffractive cholesteric gratings*, O.D. Lavrentovich, seminar at the Institute of Physics, National Academy of Sciences, Kyiv, Ukraine, July 2, 1999
17. *Cholesteric fingerprint structures and beam steering devices*, O.D. Lavrentovich, Seminar at Istituto Nazionale di Fisica Nucleare, Bologna, Italy, July 12, 1999
18. *Fast Beam Steering Cholesteric Diffractive Devices*, O.D. Lavrentovich, S.V. Shiyanovskii, and D. Voloschenko, **Proceedings of SPIE**, vol. 3787 Optical Scanning: Design and Application, 21-22 July 1999, p. 149-155 (1999)
19. *Cholesteric Fingers: Oily streaks and Dislocations*, T. Ishikawa, D. Voloschenko, S.V. Shiyanovskii, D.-K. Yang and O.D. Lavrentovich, International Seminar on "Properties and Dynamics of Defects in Liquid Crystals", Aug. 17- Aug.27, 1999, Program on "Topological Defects in Non-equilibrium Systems and Condensed Matter", Max Planck Institute for the Physics of Complex Systems, Dresden, Germany.
20. *Cholesteric Fingerprints: Diffraction Optics and Photoeffects*, S.V. Shiyanovskii, D. Voloschenko, T. Ishikawa, and O.D. Lavrentovich, 8th International Topical Meeting on Optics of Liquid Crystals", Sep. 26- Oct.1, 1999, Humacao, Puerto Rico.
21. *Light-Induced Micro-Assembly of Dye Molecules from a Distorted Liquid Crystal Matrix*, D. Voloschenko and O.D. Lavrentovich, 8th International Topical Meeting on Optics of Liquid Crystals", Sep. 26- Oct.1, 1999, Humacao, Puerto Rico.

New discoveries, inventions, or patent disclosures

Patent application "Diffractive Grating with Electrically-Controlled Periodicity" filed on September 18, 1997 (patent disclosure No. KSU-181), by O.D. Lavrentovich and D. Subacius, Kent State University, is pending.

Patent disclosure No. KSU-202 "Non-lithographic patterning of polymers from liquid crystal solvents with spatially modulated director field" filed on May 22, 1999, by O.D. Lavrentovich, D. Voloschenko, and S.V. Shiyanovskii, Kent State University, is pending.